Master's thesis

NTNU
Norwegian University of Science and Technology
Faculty of Natural Sciences
Department of Physics

Jonas Bueie

Shear Viscosity of the Lennard-Jones Fluid

Master's thesis in Applied Physics and Mathematics
Supervisor: Raffaela Cabriolu
Co-supervisor: Astrid de Wijn, Christopher Devik Fjeldstad
July 2022

NTNU
Norwegian University of
Science and Technology

Jonas Bueie

Shear Viscosity of the Lennard-Jones Fluid

Master's thesis in Applied Physics and Mathematics
Supervisor: Raffaela Cabriolu
Co-supervisor: Astrid de Wijn, Christopher Devik Fjeldstad
July 2022

Norwegian University of Science and Technology
Faculty of Natural Sciences
Department of Physics

NTNU
Norwegian University of
Science and Technology

Preface

This work concludes my Master in Science degree in physics and mathematics at NTNU. The Master thesis in physics is written for the Department of Mechanical Engineering, as a part of a larger project on viscosity and friction.

Thanks to Astrid, for introducing me to an interesting scientific field, and for including me in a welcoming and helpful research group. You brought insightful comments to the discussions when I was confused, which has saved me many times during the last year. It has been enriching to be a part of the research group, and I am happy to have gotten the opportunity to partake in discussions and group meetings, and to "do science" with you.

Thanks to Christopher, for giving me all the help I could have hoped for, and more, throughout the work with this project. You have been available at any time, and have gone to great lengths in assisting me with theoretical knowledge, teaching me molecular simulation, helping me search for issues in my scripts, and with writing. You have taught me invaluable habits I bring with me when I step out into the world of science. On top of that, you have driven many interesting discussions, both scientific and otherwise.

Thanks to Raffaela, my internal supervisor at the Department of Physics, for helping me with practicalities.

Lastly, I wish to thank my great group of friends for keeping me company through these five years, both on and off campus. You have made my studies delightfully memorable! Thanks to you, *Fysikkland* will always feel a bit like home.

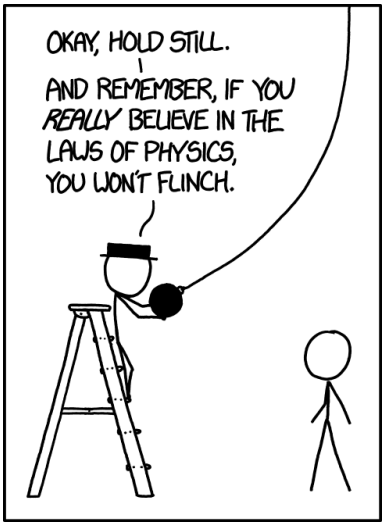

Image: `https://xkcd.com/1670/`

Sammendrag

Lennard-Jones-fluidet er en nøye utforsket enkel, men samtidig nyttig klassisk modell for fluider. I denne masteroppgaven finner vi skjærviskositeten til Lennard-Jones-fluidet, ved å ta utgangspunkt i Enskogs visositetsuttrykk fra kinetisk teori, sammen med eksisterende uttrykk for fluidets Helmholtz frie energi. Vi finner viskositeten i tre steg. Først avleder vi kompressibilitetsfaktoren (tilstandslikningen) og den indre energien til Lennard-Jones-fluidet fra dets Helmholtz frie energi. Deretter finner vi den radielle tetthetsfunksjonen ved kontakt fra tilstandslikningen og indre energien. Til slutt benytter vi den radielle tetthetsfunksjonen i Enskogs viskositetsuttrykk for å finne viskositeten.

Vi finner dermed et uttrykk for viskositeten – en ikke-likevektsegenskap – som kun er avhengig av likevektsegenskapene til fluidet. Til sammen utforsker vi fem Helmholtz frie energier for Lennard-Jones-fluidet som vi kombinerer med Enskogs viskositetslikning. Dette gir fem ulike viskositetsuttrykk. Disse uttrykkene blir så testet opp mot 336 molekylærdynamikksimuleringer. Simuleringene utforsker ulike superkritiske tilstander for Lennard-Jones-fluidet, som varierer i temperatur og tetthet.

Våre viskositetsuttrykk avviker fra simuleringsdata med oppimot 20 %, men ved å introdusere *én* empirisk tilpasningsparameter, har denne feilen blitt redusert til mindre enn 5 % for nær alle utforskede tetthets- og temperaturkonfigurasjoner. Tilpasningsparameteren korresponderer med kollisjonsintegralet til Lennard-Jones-partikler, og kan dermed rettferdiggjøres i henhold til kinetisk teori.

Dette arbeidet bidrar med ny innsikt til hvordan den innflytelsesrike Enskogs viskisotetslikning fungerer for myke og komplekse interaksjonspotensialer. Vi diskuterer videre rollen til den radielle tetthetsfunksjonen ved kontakt, som opptrer i Enskogs uttrykk for viskositet, og demonstrerer at den er tvetydig definert for myke interaksjonspotensialer.

Vi forventer at denne metoden kan utvides til å benyttes på andre liknende potensialer. Dermed kan den danne en allsidig tilnærming til å beregne viskositet med utgangspunkt i likevektstilstander.

Summary

The Lennard-Jones fluid is widely studied as a simple yet useful classical model for fluids. In this thesis, we find an expression for the shear viscosity of the Lennard-Jones fluid. This is done by using Enskog's expression for viscosity from kinetic theory, along with the Helmholtz free energy of the fluid. We find the viscosity in three steps. First, we obtain the compressibility factor (equation of state) and the internal energy of the Lennard-Jones fluid, from the Helmholtz free energy. Second, we find the radial distribution function at contact from the equation of state and internal energy. Lastly, we use the radial distribution function in Enskog's viscosity expression, to get the viscosity.

We then arrive at an approximate expression for the viscosity – which is a non-equilibrium property – dependent only on equilibrium properties. In total, five Helmholtz free energies for the Lennard-Jones fluid have been explored and combined with Enskog's expression for viscosity to give five different viscosity predictions. These expressions were then tested against 336 molecular dynamics simulations. The simulations explore different states of a supercritical Lennard-Jones fluid, varying in temperature and density.

Our viscosity expression deviates from the simulation data by up to approximately 20 %, but introducing *one* empirical fitting parameter reduces this error to less than 5 %, for almost all explored density-temperature configurations. The fitting parameter corresponds to the collision integral of Lennard-Jones particles, and thus has theoretical justifications from kinetic theory.

This work contributes with new insight into how Enskog's influential viscosity expression performs for soft, complex interaction potentials. We also discuss the role of the radial distribution function within Enskog's equation for the viscosity, and demonstrate that its numerical definition is ambiguous for soft interaction potentials.

We expect that this method can be extended to other similar potentials, yielding a versatile approach to computing viscosity only from equilibrium properties.

Contents

List of Figures

Acronyms

CS Carnahan-Starling. 23

EOS Equation of state. 9

HS Hard sphere. 8

LJ Lennard-Jones. 3

MC Monte Carlo. 31

MD Molecular dynamics. 31

RDF Radial distribution function. 13

WCA Weeks, Chandler, Anderson. 27

1. Introduction

Friction is associated with loss of kinetic energy when there is relative motion between different objects in a system. This phenomenon appears everywhere. Friction will both slow down a car, and simultaneously give it traction so that it does not slide off of the road.

Friction causes wear and tear in many everyday situations, as well as in engineering applications. At the same time, it is necessary to keep most applications functional. Without friction, we would not be able to walk around. Too much friction however, will make many tasks highly energy-consuming, as many a cross-country skier has experienced in poor weather.

Viscosity is most easily summarized as friction in a fluid – that is, friction in a gas or a liquid. The resistance we feel when swimming in water, or walking upwind, is due to friction. Certain fluids are more viscous than others. Honey flows slowly, while water runs much more rapidly. We say that honey has a higher viscosity than water.

Several aspects can change a fluid's viscosity as well. If honey is stored in the refrigerator, it will hardly flow at all. Drag resistance in air is much less noticeable than in water, because air is much less dense. This means that viscosity often decreases with the fluid's temperature, and increases with its density.

We often wish to change the friction of some system. For example, we use wheels, ball bearings and lubricants (and often so in combination) to reduce frictional resistance; and we use rubber, groove patterns (as in car tires) and even glue to increase it.

There are many systems we associate with regular sliding friction (kinetic friction), where viscosity is actually the "star of the show". In engineering applications where we wish to reduce friction, lubricants are typically used. These lubricants are often – though not always – liquid, meaning that their frictional properties are in fact viscous. This is commonly the case in rotating shafts, where regular sliding friction would not only wear out the shaft, but also cause huge amounts of resistance and noise. Perhaps more unexpectedly, even skis do not glide atop of solid snow, but on a thin film of water, melted by the frictional heat [1]. Note that this is a vastly complicated process.

Understanding viscosity is therefore an important part of understanding the friction that surrounds us, and how it impacts our technology. This Master thesis attempts to study viscosity as a transport phenomenon, as explained below.

1.1. An introduction to viscosity

If different parts of a fluid move with different velocities, momentum will be transferred between the regions of the fluid – as described by Maxwell in 1867 [2]. This phenomenon

is called viscosity. Unless external forces maintain the velocity profile of the fluid, the viscosity will eventually cause every region of the fluid to move with a uniform velocity – or to stop moving entirely. Since this process is a *transport* of momentum within a system, we call it a transport phenomenon.

Transport phenomena refer to transport of properties such as momentum, temperature and mass. The description of transport phenomena is a branch of statistical mechanics, known as transport theory.

In this thesis, we will consider one particular branch of transport theory, known as *the kinetic theory of fluids* – or simply kinetic theory. Kinetic theory allows us to mathematically describe fluids as large groups of individual particles (of certain types), and the fluid properties that arise from their behaviour.

We should discuss kinetic theory a bit further. How exactly can we describe viscosity from a large collection of particles? The mathematics behind this – summarized in section 3 – is severely complex, but the physics is somewhat intuitive.

Imagine a large amount of marbles, collected in a very spacious container. Now, imagine that all the marbles have a velocity, and start to fly about in random directions. This is (essentially) what we call temperature. The marbles now move around the container, crashing into each other and the walls of the container. Whenever they crash, they exchange a bit of energy and change directions, as marbles do. Now, let us take a look at the bigger picture: Thousands of marbles flying around the container. The *group* of marbles now exhibit some interesting behaviour – much of the same behaviour as real-world gases and liquids do. This is no huge surprise. After all, ignoring some details, gases and liquids *do* consist of vast collections of particles that "fly" around and bounce off of each other. Viewing gases and liquids (fluids) as such, allows us to derive mathematical models to describe them.

How then, does viscosity arise from said collection of marbles? Imagine now that the container is a box, and that the particles in the top half move with one velocity, and the particles in the bottom half move with another. In the border between the top and bottom half of the box, particles that move with different velocities will start to collide. Through the collisions, they exchange momenta. After a number of collisions, the velocity of the particles around the middle of the box will no longer have a clear border. After a long time has passed, both halves of the gas will be moving with the same velocity, at least if we ignore the random differences on the individual particle level. The collisions have erased the large-scale velocity difference! This is how viscosity works on a small scale.

In this project, we will not work with *marbles*. There are particle models that closer resemble real atoms which we will use instead. Let ut briefly discuss how to find more faithful representations of real atoms and molecules. First of all, atoms are not perfectly hard. When they collide, they usually "overlap" slightly[1]. We say that the particles are *soft*. We can account for this softness by altering how the particle interact.

[1] Unambiguously defining the size (and thusly, the concept of overlapping) of a real atom is not trivial. However, since this thesis is concerned entirely with classical physics, we can safely ignore this. The difference between classical and quantum physics is part of the reason why the Lennard-Jones potential exists in the first place.

There are more complicating factors as well. A water molecule has a small charge difference between its two sides, making it a weak electrical dipole. Oils and organic molecules are often large collections of different atoms, which can hardly be modelled as spheres. Several works on such complex fluids has been done, but in this thesis, we will only consider one type of soft spheres. These spheres represent a more realistic approach to fluids than simpler hard spheres, even though it is still a "simple" model.

1.2. The Lennard-Jones fluid

In 1924, John Lennard-Jones [3] introduced what is now one of the most widely studied particle interaction potentials [4]. His motivation was to create a description of the forces that particles exert on each other. The description was supposed to capture the recent development in quantum mechanics. Yet, it should not require doing the complicated mathematics typically associated with quantum mechanics. He then proceeded to use this force in relation to the kinetic theory of Maxwell, Chapman and Enskog (see section 2.1 and 3.1), to compute certain transport properties [3]. He saw this as a more efficient path to precise descriptions of fluid properties than to wait for the quantum theory to evolve. This motivation and use of the Lennard-Jones (LJ) potential remains relevant a century later.

Originally, Lennard-Jones tried several exponents in the potential before eventually settling on the form which is known as *the* Lennard-Jones potential today. This form is motivated in part by physical theory, and in part by computational simplicity, as we explain in section 3.2.2.

1.3. Description of the problem

We attempt to obtain an expression for the viscosity of the Lennard-Jones fluid, from its pressure[2] and potential energy, in combination with the Enskog equation for the viscosity of fluids. Both pressure and potential energy are equilibrium properties, while the viscosity is a non-equilibrium property. Both the pressure and the potential energy will be obtained from the Helmholtz free energy of the LJ fluid.

The resulting viscosity expression is compared to computer simulations of the LJ fluid. The simulations are molecular dynamics simulations, performed in LAMMPS [5], using the Müller-Plathe algorithm [6]. In other words, we wish to investigate the following research question.

Research question

Can we predict the viscosity of the Lennard-Jones fluid by combining Enskog theory for hard spheres with equilibrium expressions for the radial distribution function, derived from the Helmholtz free energy?

[2] More precisely, the compressibility factor Z, see section 3.3.

1.4. Motivation

Viscosity is interesting from an engineering point of view because of how it determines the efficiency of lubricants. In lubrication models, "regular" gliding friction between two lubricated surfaces in relative motion is dependent on three factors: The viscosity – denoted with an η – of the lubricant, the sliding speed v, and the pressure or load p that presses the surfaces together [7]. This relation is known as the Stribeck number

$$S = \eta \frac{v}{p} \tag{1.1}$$

It turns out that the gliding friction is mostly proportional to this number, except that it grows when S becomes very small. A model developed by Stribeck and Gumbel in the early 1900s, describes how friction changes depending on the Stribeck number. The gliding friction turns out to have a minimum at some optimal value of the Stribeck number. Accordingly, one would often wish to keep the Stribeck number at this optimal value to minimize the friction. One useful way to do this, is by changing the lubricant to get a different viscosity.

The motivation for this work is to further our understanding of viscosity for complex fluids. In particular, this work investigates Enskog's important viscosity expression (see section 3.1.3), which is commonly used as a foundation for more sophisticated viscosity models. Although the Lennard-Jones potential is mainly theoretical, understanding it is a key step towards understanding more realistic fluid models, and in turn, real fluids.

1.5. Structure of the thesis

The thesis is structured as follows. Chapter 3 introduces the main theoretical concepts, including kinetic theory and the Lennard-Jones fluid. We also explain how we obtain the appropriate viscosity equations for the Lennard-Jones fluid. Chapter 4 explains molecular dynamics, and how we will compute the numerical viscosity of the Lennard-Jones fluid. In chapter 5, we describe the methods used, and give details about the particular implementation of the molecular dynamics simulation used in this work. Then, we present the results of the computations in chapter 6, and compare them to the theory. The results are then discussed in chapter 7, where we will focus on assessing how well the theoretical descriptions of viscosity can predict the outcome of the simulations. Chapter 8 summarizes the findings.

1.6. To the examiner

This Master thesis builds upon a previous project by the same main author. Therefore, some theory sections in the thesis consist mainly of information from the project report [8], and are recounted here due to the high relevance. These sections should not contribute to the amount of credits this thesis is worth. This is the case for the following chapters and sections:

- Section 3.1
- Section 3.2.1
- Section 3.2.5
- Section 3.3.3
- Section 3.4 (but section 3.4.1 is original)
- Chapter 4

Note that every section has been reformulated and improved to suit the present problem better than the hard sphere case which was the topic of [8]. In particular, chapter 4 contains more details than the corresponding sections in [8]. The remaining chapters are original to this work.

All source code used, including LAMMPS scripts and analysis code, are available on the main author's GitHub account[3].

[3] `https://github.com/jonasbue/MD_viscosity.git`

2. Literature review

2.1. Transport theory

Physical models of fluids date back to the Euler equation of *non-viscous* flow, published in 1757 [9]. The Navier-Stokes equations generalise the Euler equations, for example by including viscosity. However, the Navier-Stokes equations do not treat the origin of viscosity theoretically, but rather let viscosity be a phenomenological constant. This constant must be measured experimentally, and inserted into the equations. Theoretical descriptions of viscosity, as well as other transport properties, are possible in kinetic theory. The foundation of kinetic theory is the Boltzmann equation, derived by Ludwig Boltzmann in 1872. From the interactions of the individual particles that comprise a fluid, the Boltzmann equation allows us to quantitatively describe transport properties such as heat conduction, diffusion and viscosity. This gives us theoretical descriptions of viscous flow that do not depend on experimental measurements, at least for certain model fluids. In 1916–17, Chapman and Enskog developed a framework for doing this, now known as Chapman-Enskog theory, or just Enskog theory [10]. We will explain the most central elements of both Boltzmann and Enskog theory in section 3.1.

2.2. Viscosity

Viscosity is a complex phenomenon, and a variety of empirical, numerical and theoretical approaches have been used to study it [11, 12, 13, 14]. From Enskog theory, Enskog's expression for shear viscosity is an important example. Enskog's expression for viscosity theoretically predicts the viscosity of a single-component fluid. The Enskog expression has also been applied to *complex fluids*. These are fluids with for example long range interaction potentials, non-isometric particle shapes, and multiple particle components. We here mention a few examples.

The Enskog theory has been generalized to fluid mixtures [12]. The Enskog equation for two components [10] is known as the Thorne equation. Tham and Gubbins have further generalized the Thorne equation to an arbitrary number of components [15].

Boltzmann originally assumed that the fluid is very dilute – that its density approaches zero – and that particles interact only at short range. Enskog then extended Boltzmann theory to intermediate densities. These assumptions work very well with hard spheres [12, 14], but grow less precise at high densities, as well as with more complex particle interactions.

Some extensions of Enskog's viscosity expression have been published. Umla and Vesovic [13, 16] have published such an extension Enskog's equation for the viscosity to

soft potentials, by introducing *two* effective particle diameters. These diameters account for two different parts of the particle dynamics, making the model more able to describe softer potentials.

Pousaneh and de Wijn [17] have studied the shear viscosity of dipolar hard spheres. Electric dipoles within the particles introduce new long-range Coulomb interactions. Working from Enskog theory, they were able to describe the viscosity of such fluids. De Wijn has furthermore studied the viscosity of fluids that consist of chain molecules [18]. This model aims to describe polymer fluids, which many lubricants are.

2.3. Viscosity, kinetic theory and molecular dynamics

Computer simulations form a link between theory and experiment, which is particularly useful in the context of kinetic theory. Molecular dynamics allows us to represent artificial model systems that cannot be created in the real world. With this, approximate theories can be tested individually, rather than to be compared to complex real-world systems in which we need several approximations at once. Furthermore, MD allows studies down to the level of individual particles, giving powerful analysis tools. This is so useful in the field of molecular physics, that this field was one of the earliest to adopt computer simulations at all [19].

A variety of published works exist on MD studies of viscosity, for several types of fluids [17, 18, 20, 21]. For instance, Müller-Plathe [6] has studied how to obtain viscosity estimates from an MD simulation, and Pousaneh and de Wijn [14], have studied how hard spheres (HS) can be efficiently modelled in molecular dynamics.

2.4. The Lennard-Jones fluid

The Lennard-Jones (LJ) potential is named after John Lennard-Jones, who introduced the potential in the 1920s [3]. The potential was developed in the early days of quantum mechanics, following novel insight on the nature of the atomic structure. The notion that the atom consists of a positively charged nucleus and a negatively charged electron cloud implied the need for a new model of atomic interaction. Such a model had to represent both the attractive and repulsive nature of the atom, and at the same time be simple enough to allow extension to larger systems. A quantum mechanical approach grows unmanageable with larger systems, so Lennard-Jones proposed a *classical* force to approximate the quantum effects. The resulting Lennard-Jones interaction potential is now a textbook example of simple atomic interactions that yields predictions of real-world fluid behaviour.

2.4.1. Equilibrium properties of the Lennard-Jones fluid

Many studies of the equilibrium properties of the Lennard-Jones fluid have been published. One of the central quantities used to describe these properties is the equation of state (EOS). The EOS and particularly the Helmholtz free energy (which is often

used to express EOSs), are powerful tools when describing the equilibrium properties of physical systems. This is explained further in section 3.3.

A vast number of equations of state expressions for the LJ fluid exits. These differ by for example derivation method, assumptions made, and the number of parameters in the equation. Stephan et al. [4] has conducted a review of 20 different EOSs for the LJ fluid. The EOSs were published between 1969 and 2019, and differ by derivation method, validity range, precision order, and number of parameters.

The most widely used LJ EOS is that of Kolafa and Nezbeda [4, 22], which was published in 1994. Shortly after, Mecke [23] (1996) published a similar EOS. In recent years, Thol et al. [24] (2016) and Gottschalk [25] (2019) have published EOSs of much higher orders. These four equations are all derived in an empirical manner. From an initial function, they were fitted to numerical data, generated with Monte Carlo and molecular dynamics simulations. One EOS that separates itself from these empirical ones, is that of Hess [26]. This EOS was derived as an extension of the theoretical van der Waals equation of state, with an empirical correction factor. All these EOSs are described in section 3.3.4.

2.4.2. Transport properties of the Lennard-Jones fluid

There are not too many available studies on the transport coefficients of the LJ fluid that systematically cover a wide range of states [21]. Considering the popularity of the LJ potential, this can be somewhat surprising. Nevertheless, we here give a few examples of studies of some LJ transport properties.

Heyes [27] compared simulation data of the LJ fluid's shear viscosity, self-diffusion, and thermal conductivity to the predictions of Enskog theory. For the shear viscosity, "excellent agreement" was found. Meier et al. have published a study on the self-diffusion [28] and the viscosity [29] of the LJ fluid. In both cases, the transport coefficients were fitted to simulation data, giving empirical descriptions of the coefficients.

Dyer er al. [30] has studied the transport coefficients of the LJ fluid in several different theoretical frameworks, not limited to kinetic theory.

Lautenschlaeger and Hasse [21] have performed correlations of the truncated and shifted version (see section 4.2.3, as well as [21, 31]), but not the regular infinite-ranged LJ potential.

Furthermore, Hellmann et al. [20] have computed several transport properties – namely the shear viscosity, diffusion coefficient and the thermal conductivity – of a gas consisting of Lennard-Jones *chains*. The chains were of lengths up to 16 particles, and all gases were dilute. Their expressions agreed well with molecular dynamics simulation.

2.4.3. Applying the LJ potential to real fluids

Thol et al. [32] have studied how the LJ fluid performs as a model for the noble gases, neon, argon, krypton and xenon. The results showed that the LJ potential is able to represent all these noble gases well, with an error of 1–10 %, depending on equilibrium property. There were also little difference between the different noble gases. Due to

quantum effects from the low mass of neon, the LJ fluid was expected to perform worse for neon than the other gases. This was not observed, although for neon, the LJ fluid representation was more sensitive to the choice of the potential parameters σ and ϵ. These parameters will be defined in section 3.2.2. Imprecisions due to the classical nature of the LJ potential were also pointed out by Tchouar et al. [33]. They studied the performance of the LJ liquid as a model for Helium, methane, neon and nitrogen. The results showed overall good performance of the LJ potential, but that quantum corrections are necessary close to the triple point

Wang et al. [34] has even applied the LJ potential to a collection of hydrocarbons. They performed a fitting of experimental data to obtain values for the parameters in the LJ potential. This allowed them to model the diffusion of hydrocarbons in an acetylene flame.

2.5. Contribution of this work to the scientific field

As the above examples demonstrate, the LJ potential is able to reproduce certain properties of real-world fluids. This motivates the current study of the viscosity of the LJ fluid, in an endeavour to further our understanding of the viscosity of real world complex fluids. The goal of this study is to understand how Enskog's viscosity expression performs for the Lennard-Jones fluid, when combined with more recent and precise descriptions of its equilibrium properties. This can contribute to understanding how models for more complex fluids can be developed and improved.

3. Theory

This chapter introduces the main theoretical concepts on which the current work builds. Most importantly, transport theory is introduced, and a brief description of viscosity in transport theory.

3.1. Transport theory

Transport theory is a theoretical description of how thermodynamical quantities are transported through many-particle systems. These quantities are known as transport properties. Some transport properties are viscosity, diffusion and thermal conductivity.

This work builds on the branch of transport theory which is known as the kinetic theory of fluids, sometimes just known as kinetic theory. In kinetic theory, a fluid system is described on a macroscopic level through the properties of its microscopic particle components. The foundation of kinetic theory is the Boltzmann equation. It describes the time development of a probability density distribution $f(\vec{r}, \vec{p}, t)$ for a many particle system. Three terms define this probability distribution: The external forces on the system, the free-flight motion of particles in the system, and how the particles interact (collide) with each other. The Boltzmann equation can be written [35]

$$\frac{\mathrm{d}f}{\mathrm{d}t} = \left(\frac{\partial f}{\partial t}\right)_{\text{force}} + \left(\frac{\partial f}{\partial t}\right)_{\text{free}} + \left(\frac{\partial f}{\partial t}\right)_{\text{collision}}, \tag{3.1}$$

where $f = f(\vec{r}, \vec{p}, t)$, and

$$f \ \mathrm{d}^3\vec{r} \ \mathrm{d}^3\vec{p} \ \mathrm{d}t \ \equiv P(\vec{r}, \vec{p}, t) \tag{3.2}$$

is the probability of finding a particle at a point $(\vec{r}, \vec{p})$ in phase space at a time t. The three terms on the right hand side of the Boltzmann equation are the contribution from external forces, diffusion and particle collisions.

The third term, the collision term, makes the equation particularly challenging to solve. This calls for simplifying assumptions. One common way to simplify the collision term is to assume that the particles collide elastically. Enskog theory is an important analytical kinetic theory which uses this assumption. Notably, Enskog theory describes the transport properties of hard sphere fluids accurately.

3.1.1. Assumptions of Boltzmann theory

The Boltzmann equation was derived from three fundamental assumptions/approximations, that are partially interdependent. Understanding these assumptions is necessary in or-

der to understand kinetic theory, and hence, the results of this work. The Boltzmann equation applies to a fluid consisting of particles, provided that [35]

- the fluid is dilute;
- collisions last for an infinitesimally short time; and that
- the particles that collide are uncorrelated.

These assumptions require some extra attention. The first implies that the mean distance between particles is much larger than the particle diameters. We note for later that, for practical simulation purposes, this condition can be taken as valid when the combined volume of the particles make up less than approximately 30% of the fluid volume [12, 14].

The second assumption means that the average time a particle spends travelling between two collisions, $\langle t_{\text{free}} \rangle$, is much larger than the average duration of a collision, $\langle t_{\text{coll}} \rangle$. This is true if collisions are instantaneous, as for hard spheres, or if the fluid is dilute. For soft interaction potentials and/or dense fluids however, this assumption is not valid.

The third assumption is known as the assumption of molecular chaos, or Boltzmann's *stosszahlansatz* [35]. It requires that colliding particles have no "memory" of each other when a collision occurs – any collision is independent of the previous one. This is not true for dense fluids, where particles can be "trapped" within groups of neighbouring particles for extended periods of time.

The three assumptions of Boltzmann mechanics are interdependent, and if one is invalid, the two others are likely to be as well, and vice versa.

3.1.2. Enskog theory

An important contribution to kinetic theory is the Enskog theory. This is an extension of Boltzmann equation to intermediate densities. In this framework, transport coefficients can be derived from the Boltzmann equation above the zero-density limit. Since Enskog theory is built on Boltzmann theory, the three assumptions of section 3.1.1 must be valid for Enskog theory to be applicable to a system, but the "dilute system" requirement is more relaxed. In addition, Enskog theory assumes that particles collide elastically. This assumption simplifies the collision term of the Boltzmann equation.

Smooth, spherically symmetrical particles (such as atoms) undergo elastic collisions, at least assuming deformation of the particles is impossible. This is because no energy can be transferred into internal degrees of freedom. Such internal degrees of freedom are however present in more complex molecules.

3.1.3. Viscosity

Shear viscosity, commonly denoted by η, is a transport property which can be understood as friction in a fluid system. Viscosity is associated with a transport of momentum through a system, due to a velocity gradient in the system [35]. That means, if different

regions of a viscous fluid move at different velocities, some momentum will be transported between these regions until the fluid moves with a homogeneous velocity. On a microscopic level, this momentum transport arises from collisions and momentum exchanges between particles [2]. This mechanic is described by the collision term of the Boltzmann equation. In the following, we will use the word "viscosity" about shear viscosity. The bulk viscosity, which is related to compression or expansion of a fluid (as opposed to shearing), will not be considered in this work.

Enskog's expression for the viscosity

Enskog theory is one important framework which theoretically describes viscosity. Enskog theory extends the Boltzmann equation to higher densities. From this work, Enskog derived an analytical (yet approximate) expression for the viscosity of fluids. Enskog's expression for the viscosity of a fluid consisting of particles with diameter σ, and density ρ is

$$\eta(\rho, T) = \eta_0 \left[g^{-1}(\sigma) + 0.8\, V_{\text{excl}}\, \rho + 0.776\, V_{\text{excl}}^2\, \rho^2 g(\sigma) \right]. \tag{3.3}$$

Here, V_{excl} is the excluded volume per particle. This is the volume which is inaccessible to a particle, due to other particles in the system, see figure 3.1. The excluded volume

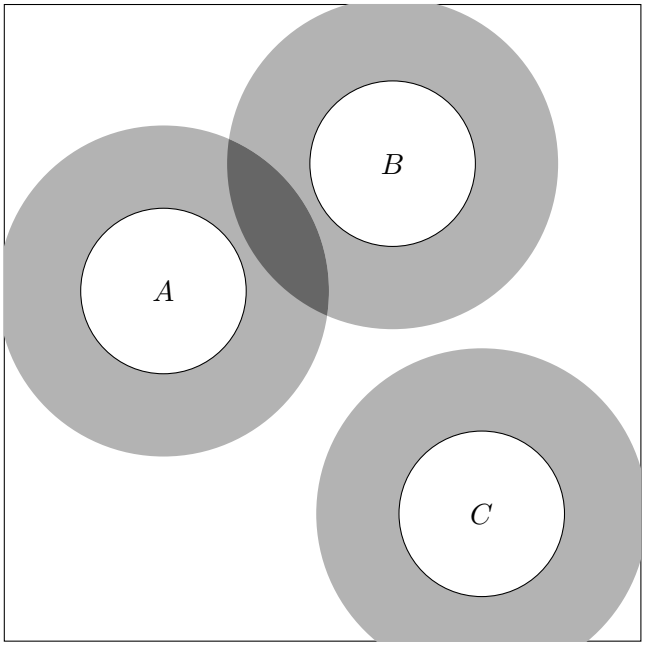

Figure 3.1.: The figure illustrates the excluded volume, V_{excl}, introduced in equation 3.3. The excluded volume is the total volume in which no particle can be located, because it would result in an overlap with other nearby particles. Three particles, A, B, and C are drawn, along with their corresponding excluded volumes, the grey shaded areas. The dark grey area is within the excluded volume of both particle A and B. Such "shared" excluded volumes are normally neglected. The figure is taken from [8].

per particle equals half the volume of a particle of *radius* σ [14]

$$V_{\text{excl}} = \frac{1}{2}\frac{4\pi\sigma^3}{3}, \tag{3.4}$$

where the prefactor 1/2 is conventional. Next, $g(\sigma)$ is the radial distribution function (RDF) at contact. We will define it in section 3.4. The prefactor $\eta_0 = \eta_0(T)$ is the viscosity in the zero-density limit

$$\eta_0 = \eta(0,T) = \frac{5}{16\sigma^2\Omega}\sqrt{\frac{m\mathrm{k_B}T}{\pi}} \tag{3.5}$$

The Enskog expression for the viscosity applies to a one-component gaseous or liquid system, provided that the assumptions of Boltzmann theory are valid.

Enskog's viscosity expression has been demonstrated to work well with for example hard sphere systems, as long as the density is low to intermediate [14, 36]. As long as the particles of a fluid does not have rotational degrees of freedom, and interact only at short ranges, we can expect the equation to provide reasonable approximations. Moreover, the expression has also been demonstrated to be a sound starting point for modelling the viscosity of more complex fluids. This can be the case, even when the assumptions of Enskog are not fully satisfied [14]. We will discuss this further in section 3.5.

As stated in chapter 1, the goal of this project is to apply the Enskog expression for viscosity to the Lennard-Jones fluid. The following sections will explain the required theory. First, we introduce the LJ fluid in section 3.2.2. Once our system is defined, we will work towards applying Enskog's viscosity expression to it. What we need to do this, is an expression for the RDF at contact, $g(\sigma)$. To get this, we will make use of the equation of state, and the internal energy. Both of these are derived from Helmholtz free energy. We therefore introduce the EOS as well as the Helmholtz free energy in section 3.3, and the RDF (and internal energy) in section 3.4.

3.2. Interaction potentials

In many-particle physics, we study large systems of particles. To get non-trivial systems, we need to define particle interactions. This section will describe two important interaction potentials – the simpler hard sphere (HS) potential, and the more complex Lennard-Jones potential.

3.2.1. The hard sphere potential

A hard-sphere gas consists of finite-sized particles that interact through the interaction potential

$$u(r) = \begin{cases} \infty, & r < \sigma \\ 0, & r > \sigma. \end{cases} \tag{3.6}$$

This interaction gives instantaneous, perfectly elastic collisions. The HS potential has been widely studied in kinetic theory and in MD and MC simulations. Accurate (though

not exact) expressions for the transport coefficients of HS fluids exist [10, 12, 15, 21, 27, 28, 29, 33].

3.2.2. The Lennard-Jones potential

The Lennard-Jones potential has historical significance in the field of physical chemistry, and is considered a textbook example of a particle-to-particle interaction potential in statistical physics and chemistry [4, 19, 37]. The Lennard-Jones potential is

$$u_{\mathrm{LJ}}(r) = 4\epsilon \left[\left(\frac{\sigma}{r}\right)^{12} - \left(\frac{\sigma}{r}\right)^{6} \right], \tag{3.7}$$

where ϵ denotes the depth of the potential at its minimum. The rest of the notation is as in equation 3.6, although the size of the particles, represented by σ, is no longer unambiguous. The particles are now soft, and can overlap slightly. The diameter σ determines the size of the particles, but it also affects the softness of the potential. The Lennard-Jones potential is illustrated in figure 3.2.

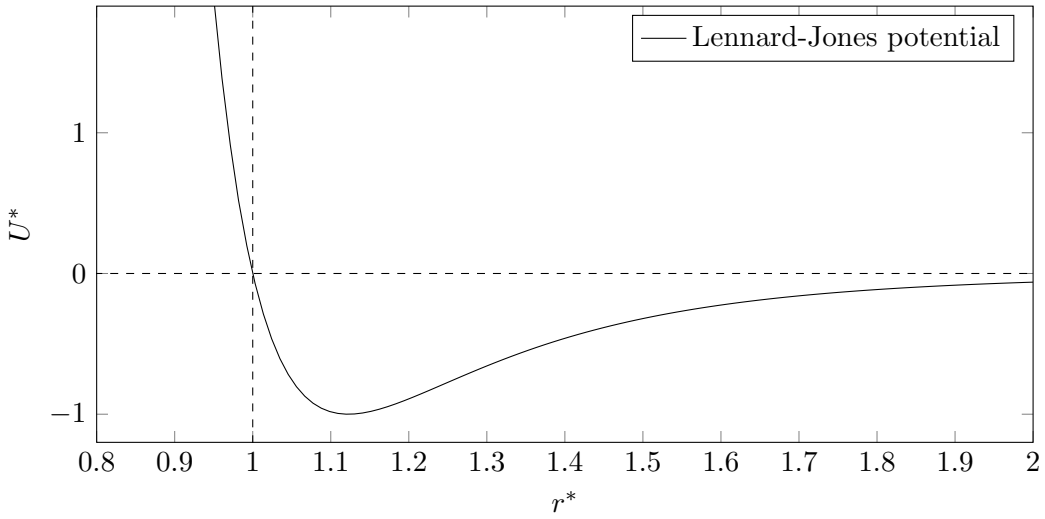

Figure 3.2.: The Lennard-Jones potential. The dashed lines represent $r = 1$ and $U = 0$. At short ranges, the LJ potential is strongly repulsive. At intermediate ranges, it is weakly attractive. Lastly, at long ranges, it approaches zero. The axis values are given in Lennard-Jones reduced units (see section 3.2.5), so the particle diameter σ is where $r^* = 1$.

The Lennard-Jones potential contains an attractive and a repulsive part. These are, respectively, the positive r^{-12}-term and the negative r^{-6}-term. The strong repulsive part is dominating at short ranges, and causes particle overlap to be unlikely. This represents the Pauli exclusion that prevents atomic nuclei from overlapping. The weaker attractive part represents the attractive force caused by quantum mechanical fluctuations in the electron charge distribution around the atom. This force is known as the London force, and was demonstrated by London to be proportional to r^{-6} [38].

The repulsive term in the LJ potential, however, does not have such a physical justification. In fact, Lennard-Jones studied a number of other exponents in his original paper on the subject [3]. While it does approximate the Pauli force, the precise number 12 was selected for computational convenience. It is faster to compute one exponential (the $(\sigma/r)^6$ term), and square it, rather than computing two exponentials separately. When the LJ potential was established in the field, this difference in computational cost was vast. The computational gain is less critical now, but efficiency is nevertheless useful. The Lennard-Jones potential remains a very commonly studied potential in molecular theory. It has been demonstrated to reproduce observations of real substances, particularly the noble gases [32, 33].

3.2.3. Qualitative behaviour of the Lennard-Jones fluid

In order to understand the relevance of the mainly theoretical Lennard-Jones potential, it is useful to describe its qualitative behaviour under different conditions. At very long distances, the interaction between two particles will approach zero. At very close ranges, they will strongly repulse each other, so that two particles will overlap only by tiny amounts – relative to the average kinetic energy $\mathrm{k_B}T$. At intermediate ranges, approximately $1 < \sigma < 2$, particles are considerably attracted to each other. This attraction can cause bonds between particles, which can be stable if the temperature is low.

The Lennard-Jones substance can have several phases, as illustrated in the phase diagram in figure 3.3. At low temperatures and/or high densities, it becomes a solid. In this state, the particles are bound together by the attractive force, and do not have the kinetic energy or the space to propagate individually. As the temperature increases, particles gain more energy, so the bonds between them are weaker. This can correspond to gas and liquid – fluid – states, which are the focus of this thesis. However, for certain temperature-density ranges, gas and liquid states can coexist within a system. In these cases, clusters or droplets of particles can form, giving local variations in the substance's properties.

Above its critical temperature $T_c \approx 1.31$ [25], the fluid phases of the LJ substance are identical. Here, the fluid behaves as a homogeneous substance. This region, as well as the regions corresponding to purely liquid and purely gaseous phases, of the phase diagram are better suited for viscosity estimates, see section 4.3 and 5. The critical density is $\rho_c \approx 0.316$ [4].

3.2.4. The effective diameter

Since the Lennard-Jones potential is soft, we have use for a way to define this softness. We can do this with the effective diameter σ_{eff}. This is the diameter which we can use in a hard-sphere fluid so that is closest resembles the soft-sphere fluid. If we assume that two particles at a temperature T collide from initial positions infinitely far apart, then the effective diameter can be estimated as the radius r where

$$u_{\mathrm{LJ}}(r) = \frac{d}{2}\mathrm{k_B}T \tag{3.8}$$

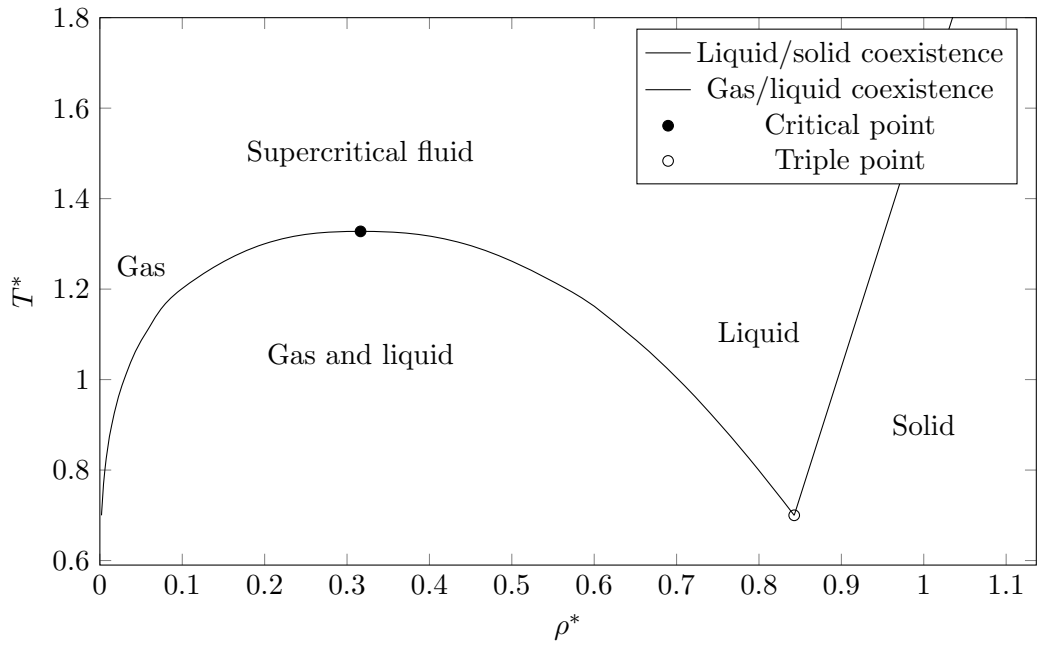

Figure 3.3.: A simplified phase diagram of the Lennard-Jones substance. Different phases are marked with text, and the solid lines mark the coexistence lines – the borders between the different phases. The critical point and the triple point are marked with a dot and a circle respectively. For low temperatures and/or high densities, the fluid is a solid. Below the gas/liquid coexistence line, above the critical point, both gas and liquid can coexist. Above the same curve, there are three homogeneous fluid regions: Pure gas, pure liquid and supercritical fluid. These are the regions in which the viscosity can be unambiguously computed with the methods presented in section 4.3. The coexistence lines are drawn with data from [25], which were computed from the Gottschalk EOS, see section 3.3.4. Reduced units are used, see section 3.2.5.

Here, d is the number of dimensions, or the translational degrees of freedom in one collision. The right side of this equation is the mean kinetic energy of a d-dimensional gas [39]. We can solve this equation to obtain an expression for σ_{eff}. Starting with equation 3.8, we have

$$\frac{d}{2}\mathrm{k_B}T = 4\epsilon\left[\left(\frac{\sigma}{r}\right)^{12} - \left(\frac{\sigma}{r}\right)^{6}\right] = 4\epsilon\left(x^2 - x\right), \tag{3.9}$$

where $x = \sigma/r$. This is a standard quadratic equation,

$$x^2 - x - \frac{d\,\mathrm{k_B}T}{8\epsilon} = 0, \tag{3.10}$$

and solving for x yields

$$x = \frac{1 + \sqrt{1 + \frac{d\mathrm{k_B}T}{2\epsilon}}}{2} \tag{3.11}$$

Inserting $r = \sigma_{\text{eff}}$, we get that the effective diameter is

$$\sigma_{\text{eff}} = \sigma \left[\frac{1}{2} \left(1 + \sqrt{1 + \frac{d\mathrm{k_B}T}{2\epsilon}} \right) \right]^{-1/6}. \tag{3.12}$$

At $T = 0$, the effective diameter is $r = \sigma$.

In a physical system, particles will not necessarily collide from infinitely far apart. Therefore, we can estimate the effective diameter in a diffeent way, assuming that particles have initial positions close to each other. The particles are still at a temperature T. If we assume that they collide from initial positions at the minimum of u_{LJ}, $2^{1/6}\sigma$, the particles will have less energy than in the previous case. Their effective diameter is where

$$u_{\text{LJ}}(r) = \frac{d}{2}\mathrm{k_B}T + \epsilon, \tag{3.13}$$

with ϵ being the well depth of the potential. Solving the equation for σ_{eff} again yields

$$\sigma_{\text{eff}} = \sigma \left[\frac{1}{2} \left(1 + \sqrt{\frac{d\mathrm{k_B}T}{2\epsilon}} \right) \right]^{-1/6}, \tag{3.14}$$

which is a larger diameter. The difference may be relevant, particularly at low temperatures. This effective diameter serves as a lower bound of the effective diameter in a finite system, while the previous definition is an upper bound. Assuming $d = 1$, its value for $T = 0$ is $2^{1/6}\sigma \approx 1.122\sigma$, and this definition of the effective diameter is σ at $T = 2$.

3.2.5. Lennard-Jones reduced units

From the quantities in the Lennard-Jones potential, it is possible to define a set of dimensionless units. These are known as the Lennard-Jones reduced units, or simply Lennard-Jones units [19]. The basis units of this unit system are length σ, energy ϵ, and mass m, all of which appear in the LJ potential, equation 3.7. Also, the Boltzmann constant $\mathrm{k_B}$ is 1 by definition in these units.

We denote quantities given in LJ units with an asterisk. For example, distance is denoted r^*, and is the distance given in multiples of σ. Following is the definition of some quantities in LJ units:

$$\begin{aligned}
\text{Distance} \quad & r^* = \frac{r}{\sigma}, \\
\text{Time} \quad & t^* = t\sqrt{\frac{\epsilon}{m\sigma^2}}, \\
\text{Energy} \quad & \epsilon^* = \frac{E}{\epsilon}, \\
\text{Temperature} \quad & T^* = \frac{k_B T}{\epsilon}, \\
\text{Density} \quad & \rho^* = \frac{\rho\sigma^3}{m}, \\
\text{Viscosity} \quad & \eta^* = \eta\frac{\sigma^3}{\epsilon t}.
\end{aligned} \tag{3.15}$$

There are several reasons to use the Lennard-Jones units. One is that most physical quantities are close to unity in this system. This makes computer calculations less prone to rounding errors. Another reason is that one physical state in LJ units can correspond to multiple states in SI units. For example, both argon at $T = 60\,\mathrm{K}$ with a density of $\rho = 840\,\mathrm{kg\,m^{-3}}$ and xenon at $T = 112\,\mathrm{K}$ and $\rho = 1617\,\mathrm{kg\,m^{-3}}$ correspond to the same state in reduced units, $T^* = 0.5, \rho = 0.5$ [19].

3.3. The equation of state

The *equation of state* relates the state of a thermodynamic system to quantities such as pressure, volume and temperature. In this work, we will use the equation of state, along with the internal energy to obtain viscosity predictions for the Lennard-Jones fluid. In this section, we introduce the EOS, as well as the Helmholtz free energy. The latter is a somewhat more versatile quantity, which is often used to express the EOS in literature.

To concretely explain the EOS, is is useful to start with the simple ideal gas model. An ideal gas is a gas consisting of non-interacting particles. An ideal gas consisting of N particles at volume V, pressure p and temperature T, obeys the ideal gas law

$$pV = N\mathrm{k_B}T, \tag{3.16}$$

where $\mathrm{k_B}$ is the Boltzmann constant. Rearranging, we can define the compressibility factor

$$Z(\rho) \coloneqq \frac{pV}{N\mathrm{k_B}T} = \frac{p}{\rho\mathrm{k_B}T}, \tag{3.17}$$

where $\rho = N/V$ is the number density, or simply the density of the system. The compressibility factor is also known as the *reduced pressure* [24], as it is a dimensionless pressure expression.

For an ideal gas, the compressibility factor is equal to one, by definition. The *equation of state* for the ideal gas is therefore

$$Z = \frac{pV}{N\mathrm{k_B}T} = 1. \tag{3.18}$$

Often, we will simply call the quantity Z for the equation of state.

For more advanced gas models, the compressibility factor is typically one only in the zero-density limit, when particle-particle interactions are so rare they are negligible. This is the case for the HS and LJ models, discussed in section 3.2.

For most practically relevant interaction potentials, no exact equation of state is known for the corresponding many-particle systems. For example, the HS potential is not particularly complex, but all existing EOSs for systems of HS fluids are approximate. A common approach to approximating the EOS involves using the *virial expansion* – a Taylor expansion in Z as a function of number density. The virial expansion generally has the form

$$Z(\rho) \approx c_0 + c_1\rho + c_2\rho^2 + c_3\rho^3 + \ldots = \sum_{i=0}^{n} c_i\rho^i, \tag{3.19}$$

where the coefficients c_i can be obtained using theoretical and numerical methods, or a combination thereof.

It is often useful to express the EOS as a function of packing fraction ξ, also known as volume density, instead of number density ρ. The packing fraction is the total volume occupied by particles of the system, divided by the volume of the system itself. Assuming σ is the diameter of the particles, the packing fraction is

$$\xi = \frac{V_{\text{particles}}}{V} = \frac{\pi N \sigma^3}{6V} = \frac{\pi \sigma^3}{6}\rho. \tag{3.20}$$

3.3.1. Expressing the EOS in terms of Helmholtz free energy

A more versatile approach to the equation of state concept, is the Helmholtz free energy F. Generally, F contains more information about a system than Z. Knowing the Helmholtz free energy, any thermodynamical property can be derived from it. In general, the compressibility factor Z can be expressed in terms of the Helmholtz free energy. Therefore, we can express the equation of state in terms of F rather than Z. The strength of this, is that all thermodynamic quantities are then given as derivatives in temperature and density of F.

Later, in section 3.4, we will find expressions for the RDF at contact from F. In this section, we will derive the relation between F and Z. We outline the derivation here, but details can be found in standard textbooks on thermodynamics [39, 40].

The Helmholtz free energy is defined as

$$F = U - TS, \tag{3.21}$$

where U is the internal energy (the potential energy) of the system, T is the temperature, and S is the entropy. Inserting a standard definition for the internal energy [39], this leads to an expression for the free energy, written in differential form as

$$\mathrm{d}F = -S\mathrm{d}T - p\mathrm{d}V + \sum_{j=1}^{M} \mu_j \mathrm{d}N_j. \tag{3.22}$$

Here, p and V are pressure and volume, and μ_j is the chemical potential of particle j. There is a total of M particles. $\mathrm{d}N_j$ is a differential in the particle number – corresponding to if we were to insert new particles to our system.

Rearranging, and assuming constant temperature and particle number ($\mathrm{d}T = \mathrm{d}N_j = 0$), gives that the pressure is

$$p = -\left(\frac{\partial F}{\partial V}\right)_{T,N} = \frac{\rho}{V}\left(\frac{\partial F}{\partial \rho}\right)_{T,N}. \tag{3.23}$$

Now, we will express the pressure in terms of the *reduced* Helmholtz free energy, per particle [24].

$$f \coloneqq \frac{F}{N \mathrm{k_B} T} \tag{3.24}$$

This reduced free energy is the quantity we will primarily use in the remaining text. It is simply a redefinition, and using f instead of F does not change the physics in any way. This gives the compressibility factor

$$\frac{pV}{Nk_BT} \equiv Z = \rho \left(\frac{\partial f}{\partial \rho} \right)_{T,N}, \tag{3.25}$$

as a function of free energy, as required.

General Helmholtz free energy derivatives

More generally, we can express thermodynamical quantities as derivatives of F, which take the form [4, 24, 25]

$$\tilde{F}_{nm} = \frac{\rho^m}{T^n} \frac{\partial^{n+m} f}{\partial \left(1/T\right)^n \partial \rho^m}. \tag{3.26}$$

In this notation, the compressibility factor is

$$Z = \tilde{F}_{01} = \frac{p}{\rho k_B T} = \rho \frac{\partial f}{\partial \rho}, \tag{3.27}$$

as we have already proven. We will not make much use of the $\tilde{F}_{nm}$ derivatives in this project. They are nevertheless highly noteworthy, as they are extensively used in literature about LJ EOSs [4, 24, 25]. Such EOSs (expressed in terms of free energy) are presented in section 3.3.4.

A remark about notation

In the context of Lennard-Jones equations of state, the symbol α is often used instead of F to denote Helmholtz free energy. Here, we will use F exclusively. In addition, there is often a large difference between notation used in different publications. To make the F expressions as clear as possible in the following, we shall therefore strive to use a consistent notation in every expression, unless convenience strongly compels us to do otherwise. When explicitly discussing free energy expressions, we therefore – mainly – give *reduced* Helmholtz free energy expressions $f = F(\rho, T)$, as defined in equation 3.24. Furthermore, we will avoid rewriting the variables ρ and T to for example δ, τ or β, even though this is commonly done in literature. This is to explicitly maintain clarity and consistence between the equations. Thus, the expressions given in section 3.3.4 may differ quite significantly from the original publications – though only by notation.

Lastly, note that the reduced Helmholtz free energy *in Lennard-Jones units* is F^* (total) or f^* (per particle), defined as

$$f^* = \frac{f(\rho^*, T^*)}{\epsilon} = \frac{F}{\epsilon N k_B T}. \tag{3.28}$$

A remark about terminology

The term "equation of state" is commonly used to reference the compressibility factor, as explained above. However, in most of the publications about EOSs for the LJ fluid considered here, the same term is used (somewhat loosely) to reference the Helmholtz free energy instead. Some authors use the same term to describe both quantities, and specify if necessary. Some use EOS only for one of them, be it Z or F.

We will attempt to make it as clear as possible which quantity we discuss, and use the specific terms "compressibility factor" (or reduced pressure), "Helmholtz free energy" (or just free energy), and their respective symbols F and Z if there may be any doubt.

The "equation of state" term will be used when discussing the compressibility factor, and when it is irrelevant which of the two we mean. For example, when discussing publications about an EOS, it is not particularly relevant if the focus of said study was F of Z (most studies give both), but when actually using the formulae, it is crucial to mind the difference. We therefore use the term "Thol EOS" to describe the free energy expression of Thol [24] (see section 3.3.4), even though we in practice are more interested in F than Z. When there is room for doubt, we also use the term "EOS on Helmholtz free energy form" – or some similar formulation – to refer to the free energy. This is to maintain some consistency with the existing literature on which this work builds.

3.3.2. Theoretical, numerical and semi-numerical equations of state

In estimating the EOS (or free energy) and the virial coefficients, both theoretical and numerical approaches are possible. Before we present actual EOS examples, it is useful to briefly outline the difference. In the upcoming sections (3.3.3 and 3.3.4), we will present examples of each type.

First, theoretical methods are equations derived from theory. The ideal gas law and the Carnahan-Starling EOS (section 3.3.3) are examples of theoretical equations of state.

A numerical EOS is derived from simulation data. This can for example be done by proposing some functional form, such as equation (3.19), and curve-fitting its parameters to numerical estimates of Z. In section 3.3.4, we will see that this is very commonly done in the case of the LJ fluid.

Semi-numerical approaches to EOS approximation are also common. This can involve using some theoretical baseline, and adapting it with numerical correction factors.

3.3.3. Equations of state for HS fluids

Before studying the more complex Lennard-Jones fluid, it is useful to let the HS interaction be a starting point. In this section, we will present one widely used hard sphere equation of state, namely the Carnahan-Starling (CS) EOS.

The Carnahan-Starling EOS is reported to give a precise prediction of the HS fluid over a wide range of densities [8, 41]. The CS EOS [42] is theoretically derived, and is

$$Z^{CS} = \frac{1 + \xi + \xi^2 - \xi^3}{(1 - \xi)^3}. \tag{3.29}$$

Recall that ξ is the packing fraction, defined in equation (3.20). The CS Helmholtz free energy for hard spheres is [23]

$$f^{*\,\mathrm{CS}} = \frac{4\xi - 3\xi^2}{(1-\xi)^2} \tag{3.30}$$

3.3.4. Equations of state for Lennard-Jones fluids

As mentioned, no exact equation of state has been reported for the Lennard-Jones fluid. Most available expressions are constructed from numerical data, or with numerical corrections. They also typically contain a large number of fitted parameters [4]. Due to the large number of available EOS expressions, a quick review is necessary. This section describes five relevant LJ EOSs – all of which are expressed as Helmholtz free energy. The focus is to give a brief summary of their derivation, strengths and weaknesses. The original papers give more details about this, along with actual derivations and tables of the fitted parameters. Table 3.1 gives an overview of these EOSs, including their reported validity ranges in T and ρ. Implementations of the EOSs, including all parameters from the original publications, are available in the aforementioned GitHub repository[1].

Table 3.1.: Validity ranges of the discussed free energy (usually referred to as equations of state) expressions, as reported in the original publications. These numbers do not take extrapolation into account, even though several of these EOSs aim to handle extrapolations to high temperatures and densities. The Hess EOS contains one numerically motivated factor, and has therefore been labelled "semi-theoretical", although it is close to theoretical.

Author	Year	EOS-Type	Density range	Temperature range
Kolafa & Nezbeda	1994	semi-numerical	$0 < \rho^* < 1.25$	$0.68 < T^* < 10$
Mecke et al.	1996	semi-numerical	$0 < \rho^* < 1.0$	$0.7 < T^* < 10$
Hess	1999	semi-theoretical	$0.1 < \rho^* < 1.1$	$0.7 < T^* < 4$
Thol et al.	2016	numerical	$0 < \rho^* < 1.08$	$0.661 < T^* < 9$
Gottschalk et al.	2019	numerical	$0.002 < \rho^* < 1.41$	$0.4 < T^* < 25$

There are several approaches to deriving an expression for the equation of state for the LJ fluid. In Stephan et al. [4], 20 EOSs, derived with a variety of methods, are presented and compared. Of these 20, five are briefly presented below. Four of these, [22, 23, 24, 25], were chosen because they performed well in the meta study of Stephan et al., and one, [26], was chosen for its simplicity, due to a lack of fitted parameters. We here present the five selected EOSs. In section 6.1, our own numerical results will be compared to these equations.

The following expressions are large and complex. Therefore, we omit the asterisks on ρ^* and T^*, but maintain reduced units in every expression nevertheless. We denote the free energy f^* *with* asterisks as a reminder that the expressions do use LJ units. Conversion to real units is a matter of insertion of the definitions of equation (3.15).

[1] `https://github.com/jonasbue/MD_viscosity.git`

The Kolafa EOS

The EOS of Kolafa and Nezbeda [22] from 1994 is a widely used LJ EOS [4]. It is a modified version of the Carnahan-Starling EOS (equation (3.29)) containing one hard-sphere part, and one numerically fitted correction part. Kolafa and Nezbeda added a 20-termed power series to the CS EOS, and fitted 32 adjustable parameters to (mainly MD) simulation data. They give the EOS on the Helmholtz free energy form. The numerical quantities to which they fitted the EOS were pressure/compressibility factor, and internal energy. The resulting equation has the form

$$f^* = f^*_{HS} + e^{-\gamma\rho^2}\rho T\Delta B_2 + \sum_{j=2}^{j=6}\sum_{i=0}^{i=4} C_{ij}\frac{\rho^j}{T^{i/2}}, \tag{3.31}$$

where γ and C_{ij} are fitted parameters. $\Delta B_2 = B_{2,LJ} - B_{2,HS}$ is the difference between the second virial coefficient of the LJ and the HS fluid. These coefficients are also fitted in the paper, to the functional form

$$B_2 = \sum_i C_i \frac{1}{T^{i/2}} + C_{\ln}\ln T, \tag{3.32}$$

with different coefficients C_i for each fluid. Note that other, newer computations exist for these virial coefficients [25]. While there are 20 terms in this virial expansion, the highest order term in ρ is $j = 6$.

The Mecke EOS

Mecke [23] (1995) used a similar method to Kolafa and Nezbeda, but with a different corrective expansion series in ρ. The Mecke EOS also consists of a HS and a correction part, expressed as Helmholtz free energy, and fitted to Z and U from Monte Carlo simulations. The EOS has the form

$$f^* = f^*_{HS} + \sum_i c_i \left(\frac{T}{T_c}\right)^{m_i}\left(\frac{\rho}{\rho_c}\right)^{n_i}\exp\left[p_i\left(\frac{\rho}{\rho_c}\right)^{q_i}\right], \tag{3.33}$$

where n_i, m_i, p_i and q_i are data-fitted parameters. T_c and ρ_c are the critical temperature and density for the LJ fluid, mentioned in section 3.2.3. There are 38 numerically fitted parameters in total. The exponents n_i of ρ are not given here, so we mention that this f^*function has terms up to order $\mathcal{O}(\rho^{10})$.

The Thol EOS

Thol et al. [24] proposed an EOS in 2016 which does not build on a hard-sphere EOS, but on the ideal gas EOS instead. The approach is otherwise similar to the procedures for the above EOSs. Thol assumed that the EOS of an LJ fluid could be written as a

series expansion in density and temperature, and correlated a total of 67 parameters to MC simulation data. The resulting free energy has the form

$$\begin{aligned} f^* = f_0^* &+ \sum_{i=1}^{6} n_i \left(\frac{\rho}{\rho_c}\right)^{d_i} \left(\frac{T_c}{T}\right)^{t_i} \\ &+ \sum_{i=7}^{12} n_i \left(\frac{\rho}{\rho_c}\right)^{d_i} \left(\frac{T_c}{T}\right)^{t_i} \exp\left[-\left(\frac{\rho}{\rho_c}\right)^{l_i}\right] \\ &+ \sum_{i=13}^{23} n_i \left(\frac{\rho}{\rho_c}\right)^{d_i} \left(\frac{T_c}{T}\right)^{t_i} \exp\left[-\eta_i \left(\frac{\rho}{\rho_c} - \epsilon_i\right)^2 - \beta_i \left(\frac{T_c}{T} - \gamma_i\right)^2\right], \end{aligned} \tag{3.34}$$

where n_i, d_i, t_i, l_i, η_i, β_i, γ_i and ϵ_i are fitted parameters. f_0^* is the Helmholtz free energy of an ideal gas. The series is of order 5 in ρ. One difference between this EOS and the previous two, is that Thol fitted the EOS to many more parameters than just the compressibility factor and the internal energy. In total, nine different Helmholtz derivatives were used, namely $\tilde{F}_{00}$, $\tilde{F}_{10}$, $\tilde{F}_{20}$, $\tilde{F}_{01}$, $\tilde{F}_{11}$, $\tilde{F}_{21}$, $\tilde{F}_{02}$, $\tilde{F}_{12}$, and $\tilde{F}_{22}$.

The Gottschalk EOS

The largest EOS presented here is the Gottschalk EOS of 2019. Gottschalk postulated an EOS similar to the Thol EOS (equation (3.34)), but with a virial expansion as a starting point. The EOS therefore consists of two parts, a virial series with coefficients $B_i(T)$; and a correction series with coefficients $C_i(T)$. Both parts form power series in ρ, as in the three previous EOSs. The coefficients were fitted to MC simulation data of the same nine quantities used in the Thol EOS. The full Gottschalk free energy has the form

$$f^* = f_0^* + \sum_{i=2}^{6} \frac{\rho^{i-1}}{i-1} B_i(T) + \sum_{i=7}^{16} \frac{\rho^{i-1}}{i-1} C_i(T), \tag{3.35}$$

where

$$B_i(T) = \left(\frac{T}{4}\right)^{-\frac{i-1}{4}} \left\{ \bar{B}_i^{SS} + \sum_{k=1}^{k_i} b_{i,k} \left[\exp\left(c_i/\sqrt{T}\right) - 1\right]^{\frac{2k-1}{4}} \right\}, i \in \{3, \dots 6\}; \text{ and} \tag{3.36}$$

$$C_i(T) = \left(\frac{T}{4}\right)^{-\frac{i-1}{4}} \left\{ \bar{C}_i^{SS} + \sum_{k=1}^{k_i} c_{i,k} \left[\exp\left(d_i/\sqrt{T}\right) - 1\right]^{\frac{2k-1}{4}} \right\}, i \in \{7, \dots, 16\}. \tag{3.37}$$

The parameters $\bar{B}_i^{SS}, b_{i,k}, c_i$ as well as $\bar{C}_i^{SS}, c_{i,k},$ and d_i are all fitted to data. In total, the Gottschalk EOS has 167 such parameters, and is of order 15 in ρ. Again, f_0^* is the ideal gas free energy. For $B_2(T)$, an exact analytical expression for the LJ fluid is used, which is [25]

$$B_2^{\mathrm{LJ}} = \frac{\sqrt{2}\pi^2}{3} \frac{e^{1/2T}}{T} \left[I_{-3/4}\left(\frac{1}{2T}\right) - I_{-1/4}\left(\frac{1}{2T}\right) - I_{1/4}\left(\frac{1}{2T}\right) + I_{3/4}\left(\frac{1}{2T}\right) \right]. \tag{3.38}$$

The Hess EOS

The final EOS which we consider here, is the Hess EOS of 1999 [26]. It is noteworthy for having zero fitted parameters, making it significantly easier to implement. The Hess EOS is a modified Van der Waals EOS, derived from the *purely repulsive* Weeks, Chandler, Anderson (WCA) potential

$$u_{\mathrm{WCA}}(r) = \begin{cases} 4\epsilon\left[\left(\frac{\sigma}{r}\right)^{12} - \left(\frac{\sigma}{r}\right)^{6}\right] + \epsilon, & r < 2^{\frac{1}{6}}\sigma \\ 0, & r > 2^{\frac{1}{6}}\sigma. \end{cases} \tag{3.39}$$

The WCA potential [43] is an LJ potential which is shifted upwards by ϵ and then cut off at zero. This removes the attractive part without altering the softness of the potential. The LJ potential can then be written $u_{\mathrm{LJ}} = u_{\mathrm{WCA}} + u_{\mathrm{dis}}$, where u_{dis} is a "distortion" term. Hess then proceeds to compute the EOS for the WCA and the distortion potential separately. Hess gives the EOS explicitly in pressure as well as free energy. As with the above expressions, we will here use the free energy form

$$\begin{aligned} f^* &= f^*_{\mathrm{WCA}} + f^*_{\mathrm{dis}} \\ &= T\left\{\frac{\rho B_2^{\mathrm{WCA}}(T)}{1-\rho v_{\mathrm{eff}}} + 2\left[\frac{\rho v_{\mathrm{eff}}}{1-\rho v_{\mathrm{eff}}}\right]^2\right\} + \rho T\left(B_2^{\mathrm{LJ}} - B_2^{\mathrm{WCA}}\right), \end{aligned} \tag{3.40}$$

where B_2^{LJ} and B_2^{WCA} are the second virial coefficients of the LJ and WCA fluid, respectively. The first term of equation (3.40), f^{WCA}, is a modified CS free energy, in which the volume of the particles is replaced by an effective volume

$$v_{\mathrm{eff}}(T^*) = \frac{\pi\sigma^3}{48}\left(\frac{2}{1+\sqrt{T^*}}\right)^{1/2}. \tag{3.41}$$

This is just the volume of particles with diameter σ_{eff} instead of σ, as defined in section 3.2.4. We have given v_{eff} with asterisks on T^* to emphasise that we are still operating in reduced units. The virial coefficient B_2^{LJ} is given by equation (3.38), and B_2^{WCA} is [44]

$$B_2^{\mathrm{WCA}} \approx \frac{4\pi\sqrt{2}}{6}\left(0.19667T^2 + 10.56T + 1\right)^{-3/24}. \tag{3.42}$$

3.4. The radial distribution function

The radial distribution function is a useful tool in the study of many-particle systems. It describes the density of the system, as a function of distance from some reference particle within the system.

The RDF $g(r)$ is the local density of the system at a distance r from the reference particle, divided by the average density ρ. Assuming there are $N \to \infty$ particles in a system, at positions $r_0, r_1, ...$, we can mathematically define the RDF around a reference particle r_0 as

$$g(r) = \frac{1}{\rho}\left\langle \sum_{i\neq 0}^{N} \delta(\vec{r} - \vec{r_i}) \right\rangle. \tag{3.43}$$

This equals the average amount of particles within a spherical shell of radius r and thickness $\mathrm{d}r$. $\delta(r)$ is the Dirac delta function.

Assuming that the system is at thermal equilibrium, when $r \to \infty$, $g(r)$ approaches 1. This means that far away from the reference particle, the fluid simply has an average density of ρ. Furthermore, assuming a repulsive potential, $g(r)$ approaches zero for $r < \sigma$. This is because overlapping particles have excess potential energy, which is unlikely at equilibrium.

Of particular interest is the RDF at contact, $g(\sigma)$. This is the radial distribution function evaluated at the diameter of the particle, σ. It contains information about the density of particles around one reference particle. This is linked to for example the collision frequency, which affects the viscosity.

3.4.1. Radial distribution function of the Lennard-Jones fluid

In order to compute the viscosity, we need a value for the RDF at contact for the LJ fluid, as explained in section 3.1.3. In this section, we will explain how to obtain this value. The calculations in this section are original to this work and has not, to our knowledge, been used for the LJ fluid before. The procedure has however been used for other systems. In particular, Pousaneh and de Wijn [17] used this approach to get an RDF at contact and an Enskog viscosity for a dipolar hard-sphere fluid. This is a major motivation for this attempt to follow the same approach for the LJ fluid.

As for EOSs, no exact expression for the RDF of the Lennard-Jones fluid has been published. Morsali et al. [45] has published a numerically correlated expression for $g(r)$, with 11 adjustable parameters. This RDF was derived in a similar fashion as the free energies of section 3.3.4. The Morsali RDF is a functional

$$g(r^*, T^*, \rho^*) = \begin{cases} 1 + (r^*)^{-2}\, e^{-(ar^*+b)} \sin(cr^* + d) & \\ \quad + (r^*)^{-2}\, e^{-(gr^*+h)} \cos(kr^* + l), & r > 1 \\ s\, e^{-(mr^*+n)^4}, & r \leq 1, \end{cases} \tag{3.44}$$

where $\{a, b, c, d, g, h, k, l, m, n\}$ are all functions of density and temperature. Their expressions contain 65 adjustable parameters in total, which Morsali et al. fitted to simulation data. For the full expression, we refer to the original source [45].

Another path to an RDF for the LJ fluid, is to derive it from the Helmholtz free energy. This will not give the full $g(r)$, but the RDF at contact, $g(\sigma)$. As we saw in section 3.1.3, $g(\sigma)$ – and not $g(r)$ – is part of the Enskog expression for viscosity, and is therefore just as useful in this context.

The RDF at contact is related to the compressibility factor through the relation [12, 17, 46]

$$Z = 1 + \frac{\langle U_{\text{int}} \rangle}{N \mathrm{k_B} T} + \frac{2\pi\rho}{3} \sigma^3 g(\sigma), \tag{3.45}$$

where U_{int} is the total internal energy of the system, as used in equation (3.21). Both Z and U_{int} can be expressed in terms of Helmholtz free energy, meaning that, given an F, we know the RDF at contact.

The internal energy is given by the Helmholtz free energy derivative [17, 24]

$$\langle U_{\text{int}} \rangle = \frac{-1}{\beta} \frac{\partial F}{\partial \beta}. = -T^2 \frac{\partial F/T}{\partial T}. \tag{3.46}$$

We will prove this relation. To do this, we need to introduce the partition function

$$Q \coloneqq \sum_i e^{-E_i/\mathrm{k_B}T}, \tag{3.47}$$

where E_i is the energy of a *state* j. The partition function is a standard tool in statistical physics, so we refer to (for example) [35, 40] for details about it.

Now, we can express the probability p_j of our system being in state j [40],

$$p_j = \frac{e^{-E_j/\mathrm{k_B}T}}{Q}. \tag{3.48}$$

Knowing p_j, the expected energy of the system is

$$\begin{aligned} \langle E \rangle = \langle U_{\text{int}} \rangle &= \sum_{j=1}^{N} p_j E_j \\ &= \frac{1}{Q} \sum_{j=1}^{N} E_j e^{-E_j/\mathrm{k_B}T} \\ &= \frac{1}{Q} \sum_{j=1}^{N} E_j e^{-\beta E_j}, \end{aligned} \tag{3.49}$$

where we use $\beta = 1/\mathrm{k_B}T$ to simplify notation. Now, we use that $\mathrm{d}\ln(x)/\mathrm{d}x = 1/x$, and reformulate to

$$\langle U_{\text{int}} \rangle = -\frac{1}{Q} \left(\frac{\partial Q}{\partial \beta} \right) = -\frac{\partial \ln Q}{\partial \beta}. \tag{3.50}$$

We now use the Helmholtz free energy, which can be expressed as [40]

$$F = U - TS = -\mathrm{k_B}T \ln Q = -\frac{\ln Q}{\beta}. \tag{3.51}$$

Inserting $\ln Q = -\beta F$ in equation 3.50 gives the internal energy as a function of free energy

$$\langle U_{\text{int}} \rangle = \frac{\partial \beta F}{\partial \beta} = -T^2 \frac{\partial F/T}{\partial T}. \tag{3.52}$$

which is precisely what we need. Moving on, we insert the definition of the reduced Helmholtz free energy f, and get that

$$\langle U_{\text{int}} \rangle = -N\mathrm{k_B}T^2 \frac{\partial f}{\partial T}. \tag{3.53}$$

Rearranging equation (3.45) now gives an expression for the RDF at contact,

$$\begin{aligned} g(\sigma) &= \frac{3}{2\pi\rho\sigma^3}\left[Z - 1 - \frac{\langle U_{\text{int}}\rangle}{N\text{k}_\text{B}T}\right] \\ &= \frac{3}{2\pi\rho\sigma^3}\left[\rho\frac{\partial f}{\partial \rho} - 1 + T\frac{\partial f}{\partial T}\right]. \end{aligned} \tag{3.54}$$

If the Helmholtz free energy is known, we can obtain an expression for the RDF at contact for the system.

3.5. Viscosity of the Lennard-Jones fluid

Armed with the free energies of section 3.3.4, as well as equation (3.54), we can obtain an expression for the Lennard-Jones RDF. Thus, we know all entries of Enskog's equation for viscosity (3.3) for the LJ fluid.

Enskog theory requires short-ranged interactions (see section 3.1.1). As figure 3.2 shows, this is not the case for the LJ fluid. However, the LJ potential is very small compared to ϵ at long ranges. Within certain limits, it is very plausible for Enskog theory to give reasonable predictions also for the LJ fluid.

The Helmholtz free energies of section 3.3.4 all have one thing in common. They consist of two parts, one much simpler than the other. The Thol and Gottschalk equations use an ideal gas term F^0 plus a residual term F^r. Kolafa and Mecke use a hard sphere term F^HS plus a residual term F^r. Lastly, the Hess EOS has a purely repulsive (but soft) WCA term, and a residual "distortion" term. In every case, the residual term is a perturbation supposed to capture the behaviour that separates the LJ potential from simpler potentials. When using these EOSs (or rather, free energies) in the Enskog equation, we are treating the LJ potential as a perturbation of a simpler potential (HS, ideal gas, or WCA).

In the preceding sections, we have achieved an equation for the viscosity of the LJ fluid – which is an out-of-equilibrium property – from the Helmholtz free energy, which is an equilibrium property.

4. Molecular dynamics

Molecular dynamics (MD) is a type of computer simulation in which a many-particle system is modelled through a large number of individual particles – usually referred to as atoms or molecules – that obey the Newtonian equations of motion. This gives deterministic simulations, as opposed to stochastic Monte Carlo (MC) simulations.

Monte Carlo simulation is very useful to study systems at equilibrium, but the common Metropolis MC methods are not designed to reproduce out-of-equilibrium mechanics. We will not consider MC simulation any further in this project.

4.1. A simple description of an MD simulation

To explain the principles of molecular dynamics, we describe how a very simple MD simulation works. Every element in this simple simulation will be present in all MD simulations, though more advanced features are usually necessary for practical purposes.

To create an MD simulation, we must keep a list of coordinates, and a list of velocity vectors. These lists give the positions and velocities of the particles that we simulate, and are updated when the particles move. To start the simulation, we initialize the system by giving every particle a unique position, so that they do not overlap[1]. These positions are typically limited by the borders of some region, typically a box. The particles are also given initial velocities. The velocities can be assigned corresponding to some distribution around the desired temperature $T \propto \langle v^2 \rangle / \mathrm{k_B}$. Then, the main part of the simulation can begin. This is done in three steps:

1. The force acting on every particle is computed;
2. the particle positions are updated; and
3. the particle velocities are updated.

Every update in particle positions/velocities corresponds to an increase in time, by a small finite time step $\mathrm{d}t$. This is done by integrating the Newtonian equations of motion. The integral is most commonly – and often most efficiently – solved with the velocity Verlet algorithm [19].

The MD simulation runs by repeating the steps above any number of times, until a final time t_f is reached. The positions and velocities of the particles are updated according to Newton's classical equations of motion. With some optimization, this relatively simple algorithm allows computational modelling of many-particle systems with millions of particles.

[1] There are several ways to create initial positions, but the exact method is not important in this context.

4.2. Details about molecular dynamics

While the algorithm presented in section 4.1 produces a simple simulation of a physical system, some details should be mentioned. This section describes measures and functions which will make an MD simulation more efficient and more faithful to the laws of physics.

Powerful and versatile MD software exists and is readily available for use. Some such programmes are LAMMPS [5], GROMACS [47], DL_POLY [48] and NAMD [49]. These have a diverse set of functionalities, and are parallelised to be highly efficient at runtime. These programmes can take care of many for the following details.

4.2.1. Periodic boundary conditions

An MD simulation can only handle a finite number of particles. While this number can be large (more than $\mathcal{O}(10^6)$ [50]), the system will be nowhere close to macroscopic orders of magnitude ($\mathcal{O}(10^{23})$). However, we can improve this with *periodic boundary conditions*. When a particle crosses a boundary of the simulation cell (the box), it reappears on the other side of the cell. In these boundary conditions, two opposite edges of the box represent the same place. In this way, we can approximate a system of infinite size with a finite amount of particles [19].

While the system can behave as if spatially infinite, there is nevertheless a finite number of particles. If there are only a few particles spread out in a relatively large box, then the particles are likely to reach the edge of the box instead of colliding with each other. If this is the case, particles are not uncorrelated at far sides of the simulation cell. Such systems will show certain nonphysical behaviours, and might fail to reproduce expected results. We can avoid this by making sure that the *correlation length* – the distance at which particles are likely to be uncorrelated – is much shorter than the sides of the box.

The fewer particles there are in a system, the longer the correlation length will be, because particles are less likely to cross paths. Therefore, this type of *finite size effect* is relevant at low densities. The issue can be avoided by increasing the particle number at low densities. This, however, comes at a price of longer computation times.

4.2.2. Thermostat

The temperature is usually not constant in a simple MD simulation. Even when trying to simulate a system at constant temperatures, the temperature will not remain perfectly constant. One reason for this is that if two particles overlap, they will bounce back due to the high potential energy they share. If we model such a situation with finite time steps, the particles may end up slightly closer to each other than they would on a continuous timeline. This gives them a slight increase in potential energy, compared to the kinetic energy they had going into the collision. The particles will then leave the collision with more energy than they had to begin with. This causes a small increase in temperature. If many collisions happen, the temperature "crawl" will be noticeable.

To counter the temperature increase, we can include a thermostat in the simulation.

The thermostat is an algorithm that controls the average kinetic energy of the particles. We can do this in simpler and more advanced ways, where the more advanced methods have a stronger theoretical foundation. We will not discuss the details of how the thermostats work here, but we give an overview of the most common methods. More details about thermostats in MD are given in [19].

The simplest way to thermostat an MD simulation, is to compute the total kinetic energy (temperature) of the system, and reduce or increase it by some factor to get the desired temperature. This means (nonphysically) speeding up or slowing down the particles, to mimic the effect of a heat bath in full contact with the system. This should typically be done over multiple steps, rather than abruptly. We can then apply the thermostat at periodic intervals, to maintain a constant temperature.

A more subtle example of implementing a thermostat is the method of Andersen [51] and the Berentsen thermostat [52]. In these algorithms, the system is connected to an external heat bath of a desired temperature, and particles can "collide" with this heat bath. Collisions happen at random, and the particle will gain a speed according to some probability distribution around the desired temperature. These thermostats introduce a stochastic process – a Markov process – to the simulation. The simulation is then no longer deterministic, although they will give the same results if pseudo-random number generators are used with the same seeds.

Another group of thermostats are derived from the Lagrangian of the system itself. This group includes the Nosé-Hoover thermostat [19, 53, 54, 55], and the CSVR thermostat [56], and the Hamiltonian-derived CSLR thermostat [57]. These thermostats are theoretically more complex, but are deterministic due to the fact that they are derived from Lagrangian dynamics.

4.2.3. Handling infinite potentials

For large collections of particles, an infinite-ranged interaction potential takes a very long time to compute. With periodic boundary conditions (i.e. an infinite system size), a naïve computation of the inter-particle interaction takes infinitely long time. There are methods to solve this, see [19, chapter 12]. In the case of the Lennard-Jones potential, however, it is appropriate to simply cut off the potential at some finite distance r_c. Then,

$$u_{\text{cut}}(r) = \begin{cases} u(r), & r \leq r_c \\ 0, & r > r_c. \end{cases} \tag{4.1}$$

where $u(r)$ is our original interaction potential. This requires that the potential value is negligible at r_c, and that a *tail correction* is added, to correct for the missing potential energy. Furthermore, MD simulations of the type discussed in 4.1 do not handle discontinuous potentials. Therefore, we shift the cut-off potential u_{cut} to make it zero at r_c. Correcting equation (4.1), the cut and shifted interaction potential is now

$$u_{\text{cut-shifted}}(r) = \begin{cases} u(r) + u(r_c), & r \leq r_c \\ 0, & r > r_c. \end{cases} \tag{4.2}$$

In terms of potential values, the cut-and-shift modification is small. Yet, it makes the MD simulation much more manageable.

4.2.4. Error estimates

To obtain any quantity from an MD simulation, we can take (or compute) the instantaneous value of that quantity from one time step of the simulation. Most quantities in MD are fluctuating, however. To gain a good estimate of their value, we find the average value from multiple time steps. Now, we also require an estimate of the uncertainty of this average. We obtain such an error estimate by *block averaging*. This section briefly explains block averaging. More details are given in [19].

Imagine that we have an MD simulation, and wish to compute the pressure p from it. As mentioned, we compute and average pressure over n time steps,

$$\bar{p} = \frac{1}{n} \sum_{i=1}^{n} p_i, \tag{4.3}$$

where p_i is the pressure at time step i. If the time steps i are adjacent, all pressures p_i will be of (almost) exactly the same value, because the system is in (almost) the exact same state. These time steps are *correlated*. If we use only correlated steps in our average, the value $\bar{p}$ will certainly gain a value close to the pressures p_i that were included, but not necessarily to the true pressure. Furthermore, since the p_i are so similar, the variance

$$\sigma_p^2 = \frac{1}{n_B} \sum_{i=0}^{n} (p_i - \bar{p})^2 \tag{4.4}$$

will be small. This means we have a poor estimate of the pressure p. To improve this estimate, we compute several average values called block averages. Consider an average pressure over a finite time t_B

$$\bar{p}_B = \frac{1}{t_B} \int_0^{t_B} A(t)\ \mathrm{d}t = \frac{1}{n_B} \sum_{i=1}^{n_B} p_i, \tag{4.5}$$

where n_B is the number of time steps in t_B. The variance of the block is

$$\sigma_B^2 = \frac{1}{n_B} \sum_{i=0}^{n_B} (p_i - \bar{p}_B)^2. \tag{4.6}$$

To remove the correlation between different time steps, we must now find a good value of t_B. With increasing values of t_B, the variance increases, until t_B is much larger than the *correlation time* t_c. When $t_B >> t_c$, the variance becomes a constant. Hence, if we know the correlation time of our simulated system, we can simply pick a block length t_B. Omitting some details, we can estimate the correlation time by finding out at what block length the expression

$$t_c \simeq P(t_B) \coloneqq t_B \, \frac{\sigma_B^2}{\langle p^2 \rangle - \langle p \rangle^2} \tag{4.7}$$

becomes constant [19].

4.3. Viscosity in MD simulations: The Müller-Plathe algorithm

Müller-Plathe [6] has described an algorithm to estimate the viscosity of a fluid in an MD simulation. The basic idea is to create a velocity gradient in the simulated system, so a momentum current associated with viscosity arises. Then the viscosity can be computed from the momentum current. This section describes the Müller-Plathe algorithm, and how the viscosity is extracted from the simulation data.

Assume we have an MD simulation of a box containing N particles. The box has edges of length L_x, L_y, and L_z, where $L_z > L_x = L_y$. The box also has periodic boundary conditions, so a particle that reaches the edge of the box will continue its trajectory on the other edge. Now, we divide the box into two regions – we call them slabs. The slabs lie on top of each other, separated by a plane at height $z = L_z/2$.

There are now *two* borders between the two slabs. One at $z = L_z/2$, and one at $z = L_z$, which is the same height as $z = 0$, due to the periodic boundary conditions. We wish to control the velocity of the particles in these two borders. To do this, we divide the box further into m chunks. Two of these chunks lie at the slab borders, $z = 0$ and $z = L_z/2$. In the $z = 0$-chunk, we wish to make the average velocity of the particles as small as possible in the x-direction. In the $z = L_z/2$-chunk, we wish to make the velocity as large as possible in the x-direction. To do this, we will perform a repeated *momentum swap*, as follows.

In the $z = 0$-chunk, find the particle with the *largest* (most positive) velocity component v_x in x-direction. In the $z = L_z/2$-chunk, find the particle with the *smallest* (most negative) v_x-component. Once a particle in every chunk is selected, swap their momenta p_x in the x-direction. Now, the particle in the $z = 0$-chunk is moving along the $-x$-direction, and vice versa for the particle in the $z = L_z/2$-chunk. Next, repeat this process at regular intervals through the MD simulation. With time, this will cause a steady velocity profile in the box, positive around $L_z/2$, and negative around $z = 0$ and $z = L_z$. The velocity profile is illustrated in figure 4.1.

The momentum swap process is entirely unphysical. However, its consequences are not. As stated in 3.1.3, viscosity is associated with a transport of momentum, as a consequence of a velocity gradient in a system. The velocity gradient in x-direction, imposed on the system by the Müller-Plathe algorithm, causes a momentum current J_z in the z-direction. This current is a physical response to the swapping, and its magnitude is proportional to the viscosity of the system

$$J_z = -\eta \frac{\partial u_x}{\partial z}, \tag{4.8}$$

where $\partial u_x/\partial z$ is the slope of the velocity profile that we created.

4.3.1. Computing the viscosity

From the MD simulation, we get position and velocity data of every single particle. This allows us to compute the value of J_z and $\partial u_x/\partial z$, and hence the viscosity.

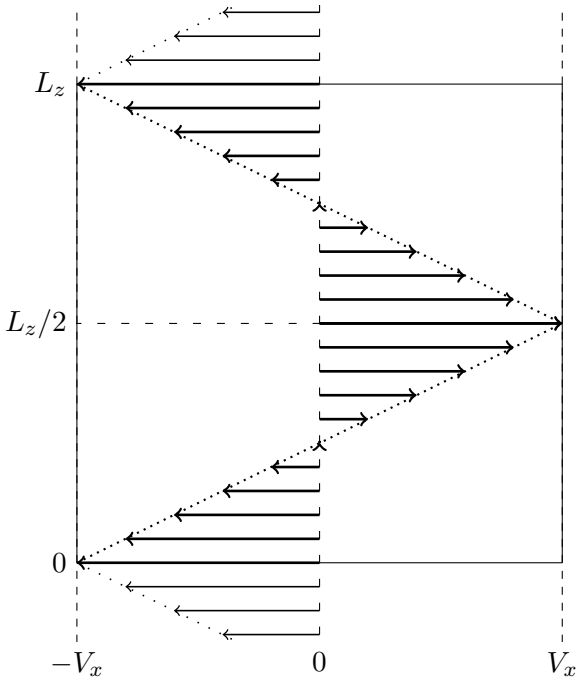

Figure 4.1.: The simulation cell, and velocity profile, of the Müller-Plathe experiment. The figure shows how the velocity increases linearly as z approaches $L_z/2$, and decreases as z approaches $z = 0$, $z = L_z$. Around the edges of the cell ($z = 0, L_z$) and in the middle ($z = L_z/2$), we perform momentum swaps at regular intervals to create the velocity profile. One simulation cell is shown, as well as the periodicity of the box. The region above the box is the same region as seen below the box. The figure is a modified version of a corresponding figure in [8].

The momentum flux J_z is the z-momentum P_z that crosses through a plane perpendicular to the z-axis, divided by the area of that plane, per time unit

$$J_z = \frac{\Delta P_z}{2A\Delta t}. \tag{4.9}$$

The factor 2 comes from the fact that the momentum flows in two directions, due to the periodic boundary conditions. The area of the box is known; $A = L_x L_y$.

Since the velocity gradient is linear, the momentum current J_z has the same magnitude across the entire box. Now, we assume that the system is in steady state – meaning that the velocity profile is constant in time. Then, the momentum transferred in z-direction due to viscosity, is the same as the momentum transferred between the chunks in the Müller-Plathe algorithm. The value of P_z is therefore just the total momentum transferred through the swapping process. Furthermore, in steady state, P_z grows steadily with time

$$\frac{\Delta P_z}{\Delta t} \to \frac{P_z}{t} \implies J_z = \frac{P_z}{2At}. \tag{4.10}$$

To obtain the value of J_z, all we need is the *final* value of the total transferred momentum P_z, and the final time t_f.

The slope of the velocity profile $\partial u_x/\partial z$ can be computed by a linear regression. Hence, the viscosity of the simulated fluid is

$$\eta = -\frac{P_z}{2At}\left(\frac{\partial u_x}{\partial z}\right)^{-1}. \tag{4.11}$$

4.3.2. Error estimate

The only source of error in the Müller-Plathe method comes from the regression of the velocity gradient. The slope $\partial u_x/\partial z$ is found by linear regression, and the error estimate associated with it is given by the regression. With a standard error estimate, we can use Gauss' law of error propagation to get an uncertainty for the full viscosity expression.

The standard deviation Δf of a function f with variables $x_1, \dots x_n$ is

$$\Delta f(x_1, \dots, x_n) = \sqrt{\left(\frac{\partial f}{\partial x_1}\Delta x_1\right)^2 + \dots + \left(\frac{\partial f}{\partial x_n}\Delta x_n\right)^2}, \tag{4.12}$$

where Δx_i is the standard deviations of the variables x_i. To simplify the notation, we now use $\partial_z \coloneqq \partial/\partial z$ to denote differentiation in the coordinate z. Given equation (4.12), the error of the viscosity, as obtained by the Müller-Plathe method, is

$$\Delta\eta = \frac{\partial\eta}{\partial(\partial_z u_x)}\Delta(\partial_z u_x) = \frac{P_x}{2tA}\left(\frac{\partial u_x}{\partial z}\right)^{-1}\Delta(\partial_z u_x) = \eta\Delta(\partial_z u_x). \tag{4.13}$$

Here, $\Delta\partial_z u_x$ is the standard error of the linear regression of the velocity slope. With the error estimate included, our expression for the numerical viscosity becomes

$$\eta = -\frac{P_z}{2At}\left(\frac{\partial u_x}{\partial z}\right)^{-1}\left[1 \pm \Delta\left(\frac{\partial u_x}{\partial z}\right)\right]. \tag{4.14}$$

To reduce the error in the viscosity estimates, we can increase the number of particles and the simulation time t_f. The former measure will provide better velocity statistics, and the latter will reduce the impact of statistical fluctuations in the estimated quantities.

We now have a way to estimate viscosity in an MD simulation of a fluid. In chapter 5, we will describe how we set up the simulations.

5. Method

A large number of MD simulations have been performed, in order to estimate the viscosity of an LJ fluid. Next, the results of the simulations were compared to the viscosity expressions which were explained in section 3.5. The resulting viscosity estimates are presented in section 6. This section describes choices made in the simulation setup, and tests to ensure that the simulations were working as expected.

5.1. Simulation setup

In the simulations, we used the Müller-Plathe algorithm of section 4.3 to create a velocity profile, and thereby compute the viscosity. The simulations were performed for densities $0.025 \leq \rho^* \leq 0.5$ and temperatures $1.3 \leq T^* \leq 4.0$. All other parameters ($\epsilon,\ \sigma,\ \ldots$) remain constant. Figure 5.1 shows all the points in (ρ^*, T^*)-space at which a computation was performed. The simulated systems contain $N = 3000$ particles, mass $m = 1$ and diameter $\sigma = 1$. For low-density systems with $\rho < 0.1$, the particle number was increased to $N = 6000$. This was done to reduce the finite-size effects which were mentioned in section 4.3.

The MD simulations have some fluctuations in temperature, which is not unusual even with a thermostat. By inspection of the LAMMPS output, a simulation with temperature set to $T = 2$ will have fluctuations in temperature between $T = 1.95$ and $T = 2.05$. This is why T was incremented in steps of $\Delta T = 0.1$. The density was incremented in steps of $\Delta\rho = 0.05$, except for when $\rho < 0.1$, where $\Delta\rho = 0.025$. The reduced step length was intended to increase precision in the region where simulations are more vulnerable to finite size effects.

The LJ potential was cut off at $r_c = 4.5\sigma$. The cut-off distance was selected by running a small number of simulations with different values of r_c. These test runs were then assessed by their ability to reproduce the expected EOSs of section 3.3.4. Around 4.5σ, we found that an increase in the cut-off distance did not contribute to more precise simulation results. At the same time, increasing the cut-off to 5σ and beyond massively slowed down the simulations.

The fluids are first initialized in a random state and equilibrated over $t_{\text{eq}} = 1000$ reduced time units. Then, the Müller-Plathe algorithm is applied to the fluid system, imposing a velocity profile and a shear stress on the fluid. This is done over $t_{\text{visc}} = 4000$ reduced time units. The time step length was $\mathrm{d}t = 0.001$, so the simulations lasted for $5 \cdot 10^6$ time steps.

The simulations were all done using the CSVR thermostat (see section 4.2.2) [56]. In the equilibration period, $t \leq t_{\text{eq}}$, a relatively low damping constant of 100 was used, to

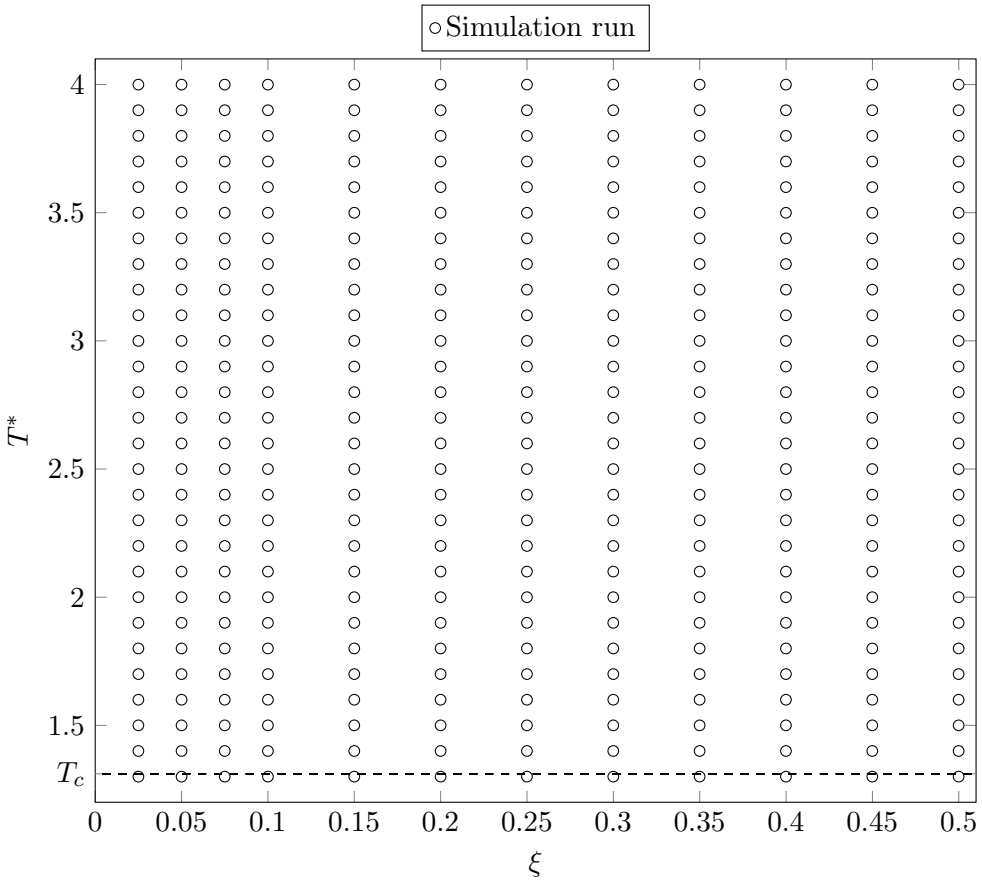

Figure 5.1.: The values of packing fraction ξ and temperature T^* used in the simulations were distributed in a grid, as shown in the figure. Every circle represents a point in (ξ, T)-space. The critical temperature $T_c \approx 1.311$ is shown as a dashed line. Reduced units are used.

reduce the equilibration time. While the Müller-Plathe algorithm was running, when $t > t_{\text{eq}}$, a high damping constant of 10 000 was used. This was done to reduce the impact of the thermostat on the simulations, while still avoiding a temperature increase due to the finite time steps.

5.1.1. Simulation tests

Before viscosity computations are performed, we need to ensure that the simulations work correctly. Several tests were done to ensure that the simulations behave as expected, and that they reproduce the behaviour of a physical system. This gives an assurance that the simulations are reliable. This section describes the tests.

First, we study the simulated systems at equilibrium, to check that they agree with existing theory. The simulations were compared to the EOSs from section 3.3. The

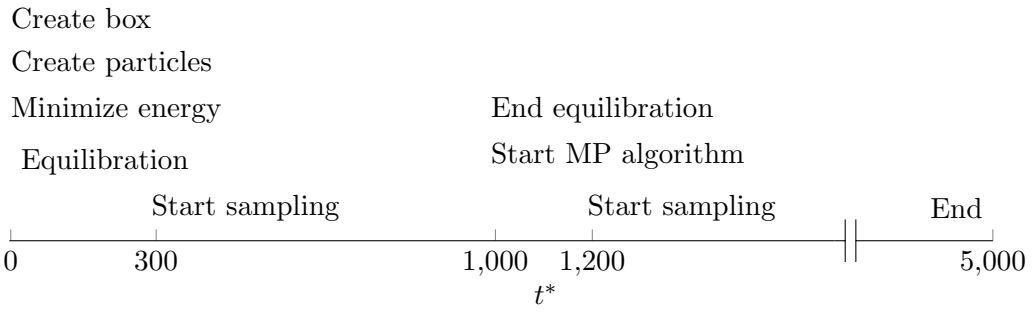

Figure 5.2.: A simple timeline showing the different steps of the simulation. The system is created and initialized with randomly placed particles. The potential energy is then minimized, so that particles do not overlap. Then, the system is equilibrated for $t_{\text{eq}} = 1000$ time units. After equilibration, the Müller-Plathe algorithm runs for $t_{\text{visc}} = 4000$ time units. This induces a velocity profile in the system, as shown in figure 4.1.

RDFs at equilibrium were also plotted to assert that their shapes were as expected. The RDF at contact was compared to the RDF of Morsali et al. [45].

It is useful to compare the equilibrium state of our simulations to equations from literature, but simulation data of previous work provides an even better test. Thol et al. [24] provides some simulation results for the compressibility factor of the LJ fluid. Our simulations were tested against these data.

Once the simulations ability to produce physical equilibrium states has been verified, we can proceed to evaluate the viscosity computations. As mentioned in section 4.3, there are a few criteria that must be met for the Müller-Plathe algorithm to work. Most importantly, the velocity profile in the box must be linear. This was tested simply by plotting the velocity data, and then visually inspecting the curves.

5.2. Data analysis

Analysis of the simulation output follows the procedures described in chapter 4, but some choices were made in the process. We briefly explain them here.

The simulation output contains data for a large number of time steps. In the equilibration phase, the earliest of these time steps correspond to non-equilibrated states. In the Müller-Plathe phase, early time steps correspond to states without a steady state velocity profile. To avoid systematic error, the first 30 % of time steps were therefore discarded.

Next, measures were taken to avoid sampling correlated time steps. In computing equilibrium quantities, block averaging was implemented as described in section 4.2.4. In the Müller-Plathe phase, error estimate comes from the linear regression, and block averaging is not necessary. However, care was taken to avoid including correlated time steps in the simulation. Therefore, sampling was only done every 3 time units (or every 3000th time step).

Velocity profiles are computed by linear regression, from the z coordinates and v_x components of every single particle, at the sampled time steps. Since non-physical momentum swaps take place in the $z = 0$ and $z = L_z/2$ chunks, these are discarded from the regression analysis, to avoid systematic error due high velocities in these chunks. The regression analysis therefore samples only the regions where particle momenta are not swapped by the Müller-Plathe algorithm.

5.3. Viscosity

In section 3.5, we discussed how to obtain viscosity expressions from the Helmholtz free energy. For each of the five Helmholtz free energies in section 3.3.4, as well as the Carnahan-Starling F, we compute the compressibility factor and the internal energy. From these, we compute an RDF, and use this in Enskog's equation for the viscosity. This gives us six different viscosity expressions.

We assess each of these expressions, not only by the viscosity precision but also the ability of the free energy functions to predict the compressibility factor. After assessing the viscosity expressions, we attempt to expand our model by introducing a new parameter, which is numerically fitted to the data. We detail this process, and its motivation, in section 6.4.1.

6. Results

This chapter presents the results of the LJ simulations, and compare them to the expressions from chapter 3. First, we show that the simulations reproduce the known equilibrium properties of LJ fluids. Next, we assert that the simulations behave as required in chapter 5. We then proceed to compare the viscosity results for the simulated fluids to the viscosity expression presented in chapter 3. We also attempt to improve the viscosity expressions by introducing an empirical, physically motivated fitting parameter.

This chapter contains several large figures. A small summary of how to read them can therefore be helpful. Most figures come in a two-column format, used throughout the chapter. In these figures, the left column shows the "true" value of the plotted data, and the right column shows the same data, normalized by one of the theory functions. Often, we normalize by hard-sphere functions, to illustrate the difference between LJ and HS. In these figures, point markers show simulation results, and curves show predictions from theory.

6.1. Compressibility factor

First of all, we present plots of the compressibility factor for the simulated systems. The simulation compressibility factors are compared to the predictions for the Lennard-Jones fluid, which are derived from the Helmholtz free energies of section 3.3.4. Both numerical and theoretical Z-values are shown in figure 6.1 and 6.2. The former of which shows $Z(\xi)$, and the latter shows $Z(T^*)$. In the left column of these figures, we see the value of the compressibility factor. In the right column, the same values are divided by the hard-sphere Carnahan-Starling compressibility factor, equation (3.29). This normalization is intended to make the curves more distinguishable, and simultaneously to clearly illustrate the difference between the HS and LJ theory. This should give a relatively clear indication of how well both the HS and the LJ equations do at explaining the behaviour of the LJ fluid.

In figure 6.3, we see the internal energy of the simulated systems. As with the Z plots, the figure includes the internal energy as obtained from the free energies of section 3.3 as well. We have omitted the internal energy corresponding to the CS EOS here, since hard spheres (by definition) have no internal energy – they cannot overlap. Hence, we have normalized the content in the right column of plots with the Thol free energy in the absence of a hard sphere curve. This has consequences for the uncertainty, which appears very large for low values of U_{Thol}. Also, because U is negative for all values of ξ, the right column contains *negative* values as well. This is done so that the largest U is at the top in both columns.

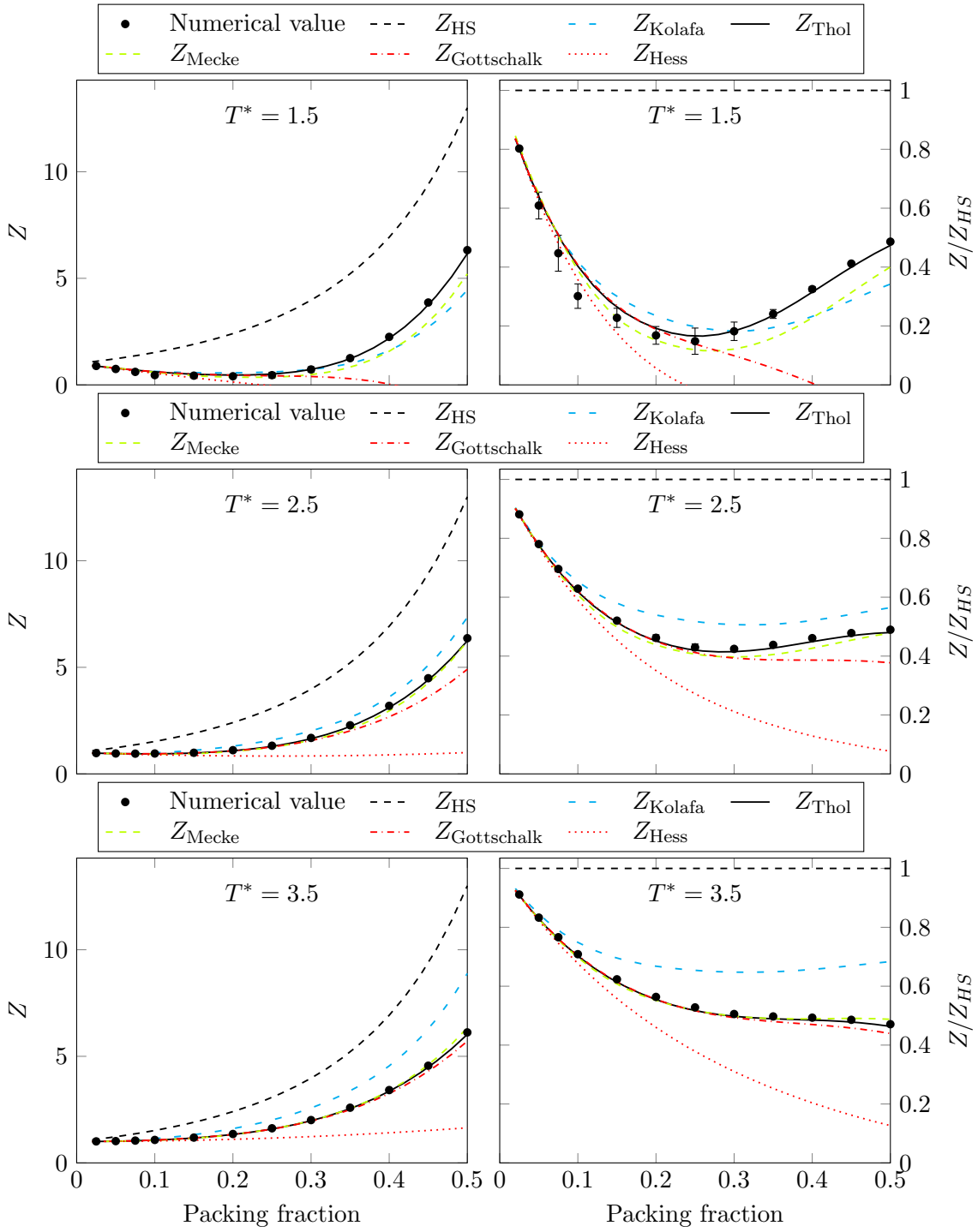

Figure 6.1.: Compressibility factor of the simulated systems (dots), compared to the equations of state from section 3.3 (curves). In the left column, the compressibility factor Z is show. In the right column, all values are divided by the hard sphere Carnahan and Starling compressibility, labelled Z_{HS}. The values are plotted as functions of the packing fraction.

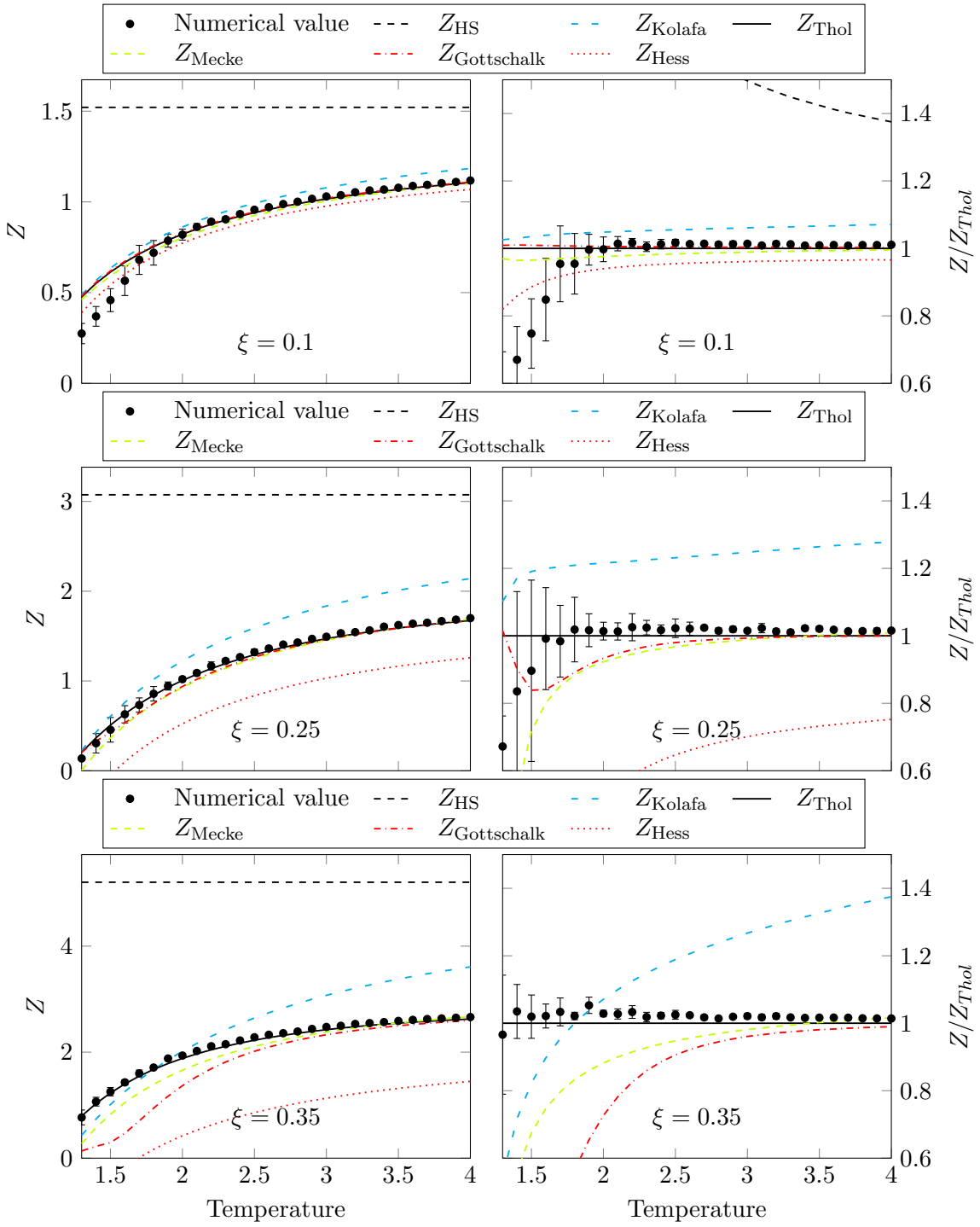

Figure 6.2.: Compressibility factor for the simulated systems (dots), compared to the equations of state from section 3.3 (curves). The values are plotted as functions of temperature. In the left column, the compressibility factor Z is shown. In the right column, all values are divided by the Z derived from the Thol Helmholtz free energy. This expression is used instead of Carnahan-Starling, because hard spheres are temperature independent, and because visual inspection indicates that Thol is performing best.

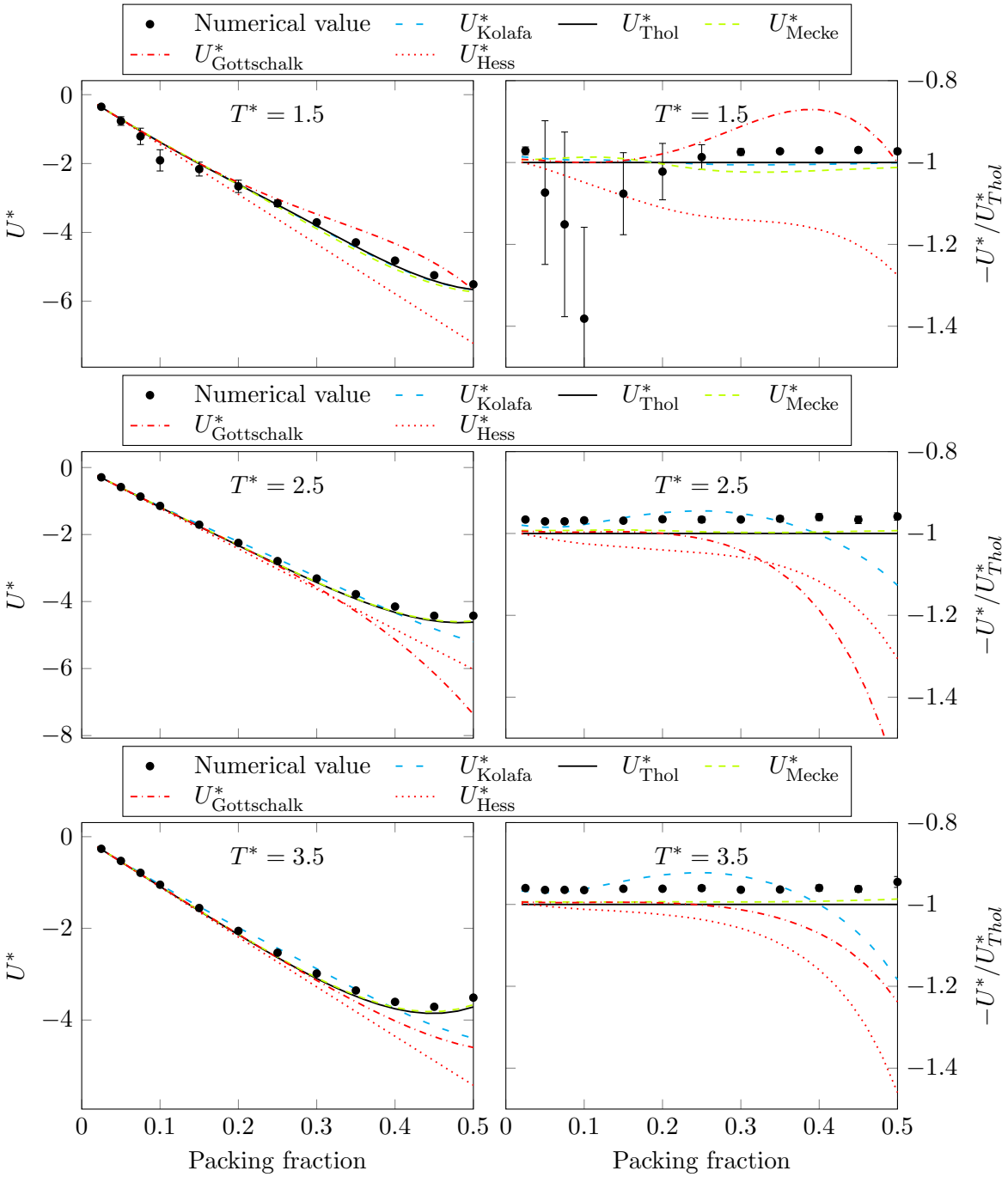

Figure 6.3.: The internal (potential) energy U^* from simulations (dots), compared to the internal energy from the Lennard-Jones Helmholtz free energy. Hard spheres have no internal energy (by definition), so the CS expression is not included. The values are shown in the right column. In the left column, all values are normalized by the internal energy from the Thol F, multiplied by -1. The sign is flipped in the right column, so that the largest values are largest in both columns, to increase readability. Reduced units are used.

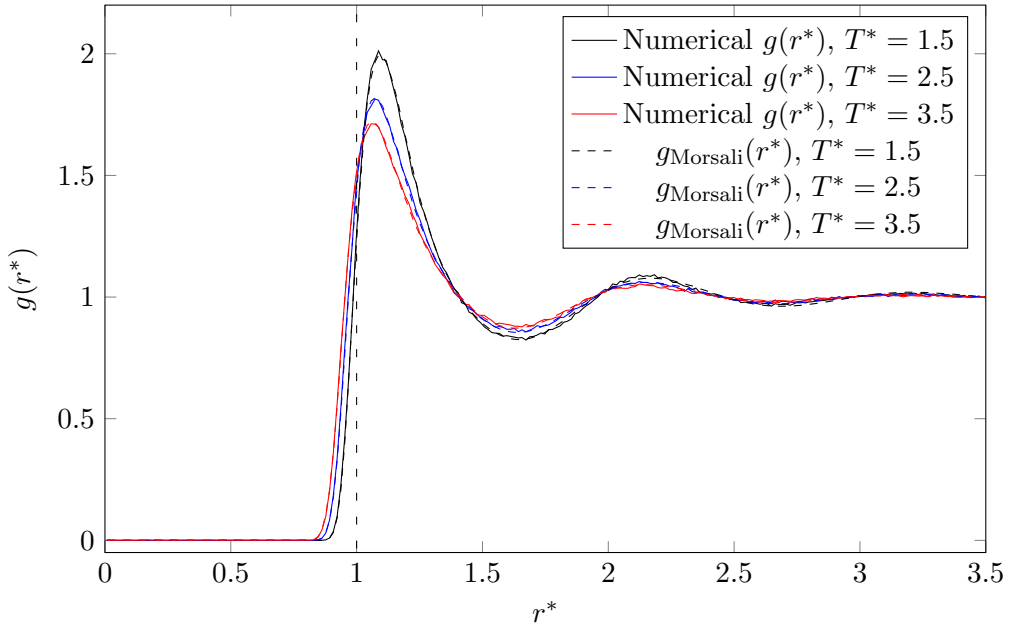

Figure 6.4.: The radial distribution function of three simulated systems, for $\xi = 0.3$ at $T^* = \{1.5,\ 2.5,\ 3.5\}$ (coloured in black, blue and red, respectively), shown in solid lines. For each curve, the corresponding RDF curve from the Morsali RDF, is given as a dashed line. The numerical RDF is computed at discrete intervals of 0.015σ. A vertical line to mark $r^* = \sigma = 1$ is included, as a reference to the steep slope of the RDFs.

6.2. Radial distribution function

Next, we take a look at the RDF of the simulated systems. There are two relevant approaches to this: We can study the RDF at contact (as a function of for example density), or the full RDF of r^*. The RDF at contact affects the Enskog viscosity more directly, but the RDF of r^* is a useful check that the system behaves as expected.

As a physicality check, we start with $g(r^*)$, shown in figure 6.4. This figure shows the RDF of three simulated systems as curves. For comparison, the Morsali RDF is plotted alongside the numerical RDFs in dashed lines.

Next, figure 6.5 shows the RDF at contact, as a function of ξ, for three different temperatures. The format of this figure is the same as the compressibility factor figures that we presented earlier. Some things are important to note here. The numerical $g(\sigma)$ in this figure is defined as *the maximum* value of $g(r^*)$, and not the value at $r^* = \sigma$. This is the same definition as used in [8, 17].

6.2.1. Definition of the numerical RDF at contact

With soft particles, the meaning of "contact" is not immediately clear. Hard spheres are in contact when separated by a distance $r^* = \sigma = 1$, but this is not necessarily where soft particles actually "feel" the effect of a collision. Energetic particles may get

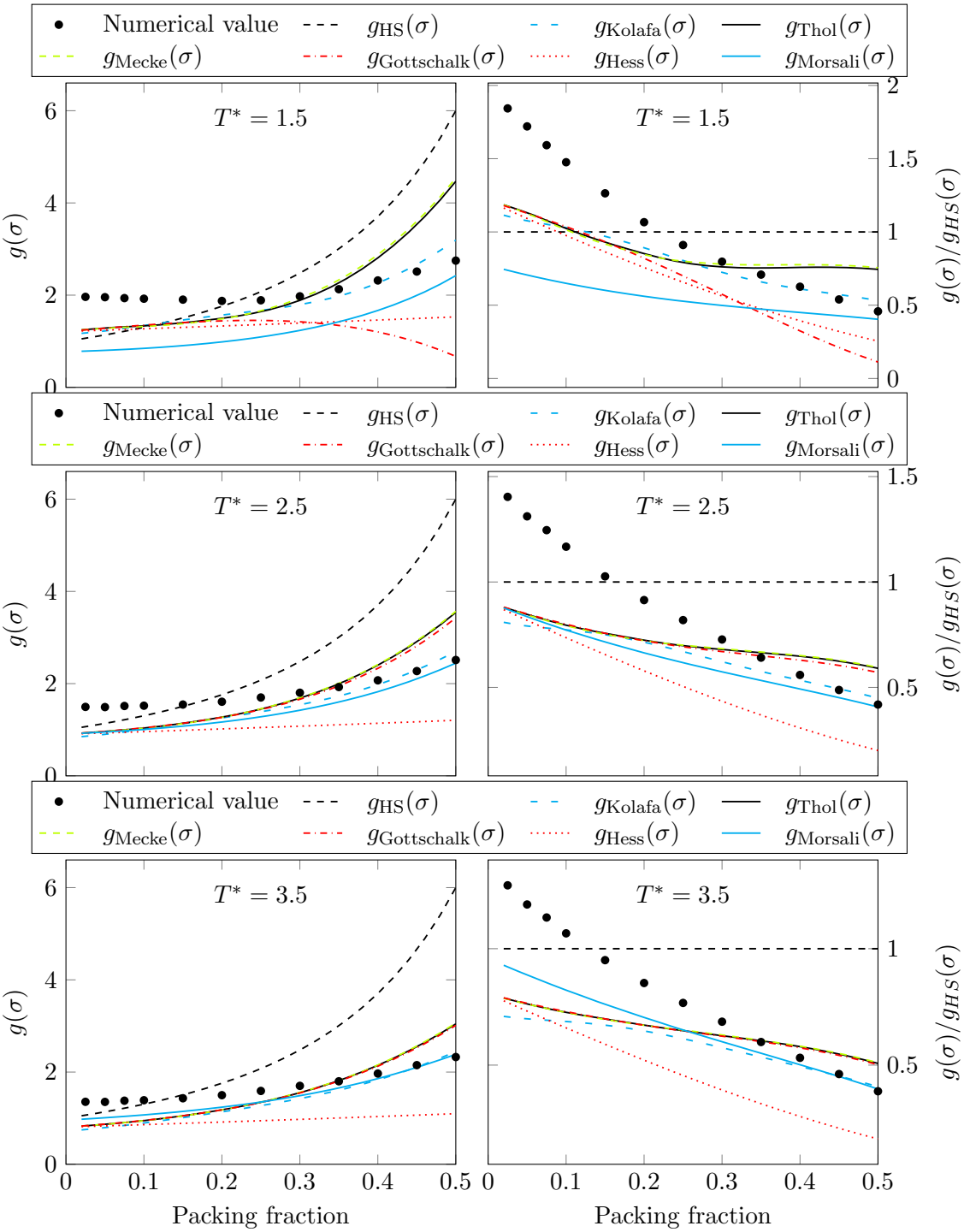

Figure 6.5.: The RDF at contact as a function of density, for temperatures $T^* = \{1.5,\ 2.5,\ 3.5\}$. The dots represent values from simulations, and the lines represent values from the free energy functions, as well as the numerically correlated RDF of Morsali et al. [45]. The numerical values in this figure are the peak values of $g(r^*)$. The left column of figures shows the RDF values, and the right column shows the same values normalized by the HS prediction. Reduced units are used.

much closer than σ, and particles that have close to no energy may stick together at $r^* = 2^{1/6}\sigma$.

In figure 6.5, we used the peak value of the full RDF as our RDF at contact. However, defining the RDF at contact as $\max[g(r^*)]$ is not the only option. Considering that hard-spheres have an effective diameter of one, it is relevant to define the numerical RDF at contact as $g(r^* = \sigma = 1)$, as a comparison. We name this definition $g(1)$, to separate it from the previous one. We can mention that for soft LJ spheres, there is no physical reason that distinguishes $r^* = 1$ from other radii, but it is nevertheless a convenient benchmark value.

More definitions are possible still. For non-zero temperatures, soft particles tend to overlap. To describe this, the effective diameter σ_{eff} was introduced in section 3.2.4. The effective diameter represents a natural point at which to define "contact". This leads to another definition of the RDF at contact, which we name $g(\sigma_{\text{eff}})$. In section 3.2.4, we introduced both an upper and a lower bound for the effective diameter. Even at low temperatures, the difference between the definitions was smaller than the resolution of our numerical RDF. In other words, no significant difference was bound between the two definitions. We therefore use only the *lower* bound – which in practice is equivalent to the upper in the present cases.

The last definition of the RDF at contact was already explored in section 3.4.1. This is the RDF at contact obtained from the Helmholtz free energy (or directly, Z and U) with equation (3.54). Due to the lack of a point at which this RDF definition is evaluated at, we denote it as the functional $g(F)$ – g as a function of the Helmholtz free energy. This to distinguish it from the remaining expressions.

We explore these four definitions of $g(\sigma)$ in figure 6.6. Here, the point markers represent different definitions of $g(\sigma)$. Some of the curves (RDFs derived from the free energies of Gottschalk, Hess and Kolafa) are also omitted in this figure, to make it more readable. Note that $g(F)$ does not give us any new information about the systems here, since the numerical Z and U match the Thol-based functions so well in figure 6.1–6.3, it is no surprise that $g(F)$ does as well. We include it to make the four definitions explicitly visible.

We will discuss the definition of the RDF at contact further in chapter 7.

6.3. Velocity profiles

One last verification of the simulations is necessary before we move on to the viscosity. The Müller-Plathe algorithm strictly requires that the velocity profile in the system be linear. Figure 6.7 shows the time averaged velocity for 18 chunks of the simulation cell. The bottom and middle chunk $z = 0$ and $z = L_z/2$ are where momentum swaps are happening. These chunks are excluded from the regression analysis, and hence from the plots as well. Additionally, regression lines for the velocities are also shown in the figure. Recall form section 4.3 that the slope of these lines are used to compute the viscosity. A steeper velocity profile is directly implying a higher viscosity. Three simulations, each at temperature $T^* = 1.5$ with varying densities are included in the figure. Note that the y-

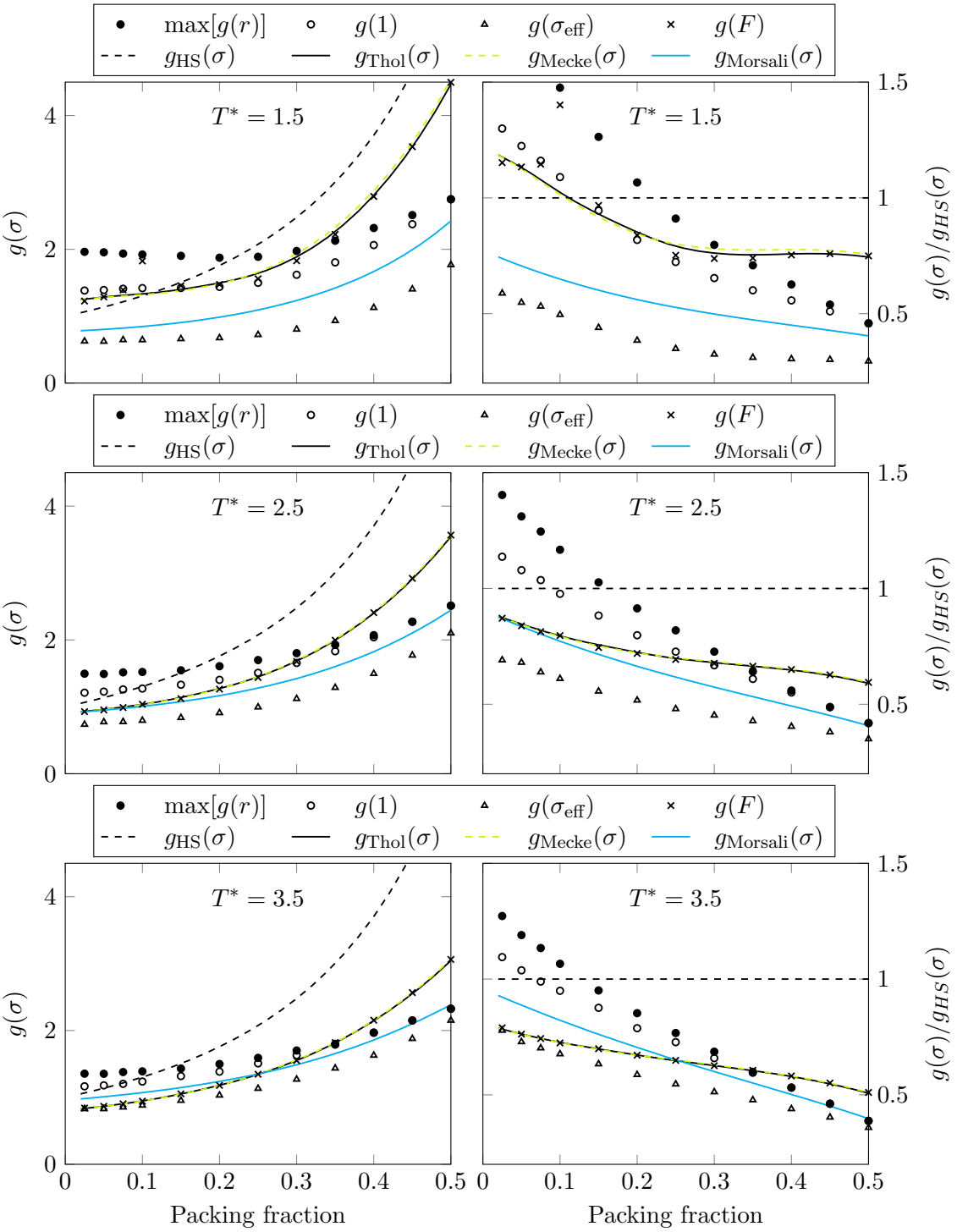

Figure 6.6.: The RDF at contact, for simulated systems (point markers) as well as from several free energy functions, as defined in equation (3.54) (curves). Here, several definitions of the numerical RDF at contact is included. The black filled circles are the maximum value of $g(r^*)$, as used in figure 6.5. The empty circles represent the RDF at $r^* = \sigma = 1$. The triangles represent the RDF evaluated at σ_{eff}, which is where $u_{\text{LJ}}(\sigma_{\text{eff}}) = \frac{1}{2}\text{k}_\text{B}T$. The crosses denote the RDF obtained from Z and U from the simulations, computed with equation 3.54. Reduced units are used.

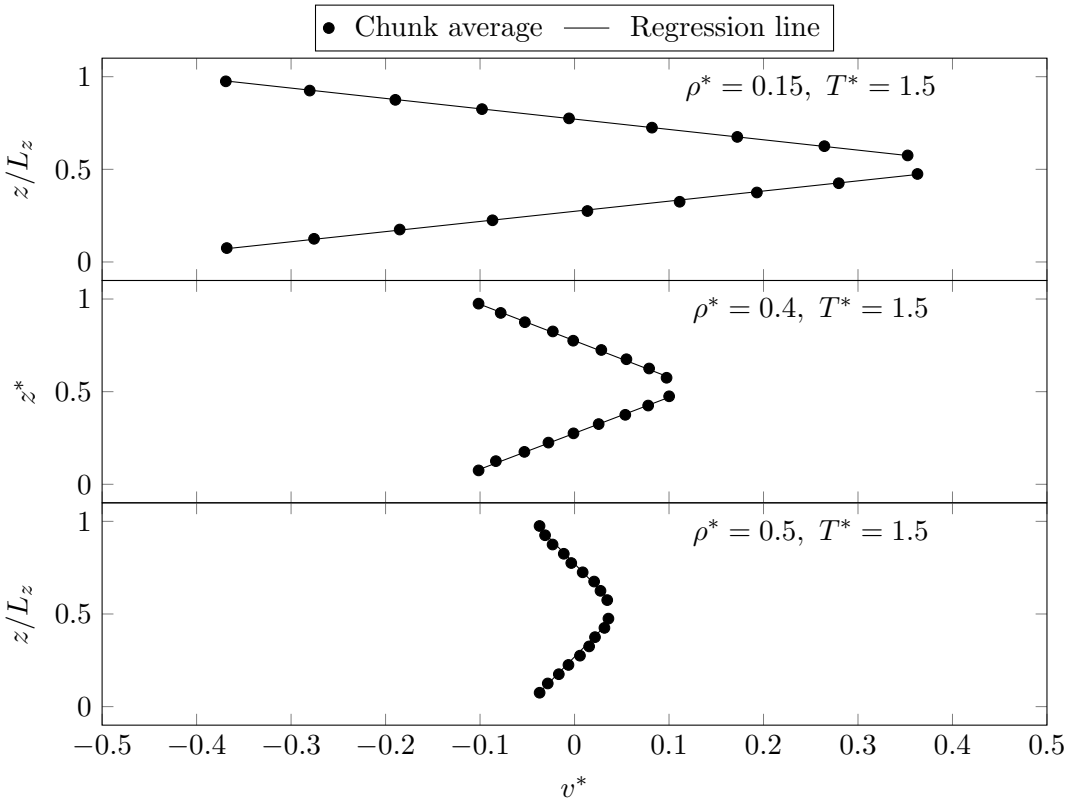

Figure 6.7.: Velocity profile in the simulation cell, extracted from three simulations, where $T^* = 1.5$ and $\xi = \{0.15,\ 0.4,\ 0.5\}$. The dots show the time average of the velocities in every chunk. The lines come from linear regression of the velocity points. Along the y-axis is the z-coordinate, the height of the particles within the box, divided by the total box height L_z. A larger version of the bottom subplot ($\xi = 0.5$) is included in appendix A, figure A.2.

axis shows the z-coordinate, and the x-axis shows the velocity component in x-direction. All three subfigures share a common x-axis, making the profiles easier to compare. Some additional figures are included in appendix A. Figure A.2 shows a larger version of the $\xi = 0.5$ figure. Figure A.3 shows the velocity profile for three different temperatures, $T^* = \{1.5,\ 2.5,\ 2.5\}$, at the same density $\xi = 0.4$. These last figures show the same qualitative behaviour as figure 6.7.

6.4. Viscosity

We can now move on to present the viscosity of the simulations, and compare them to the Enskog expression for the viscosity, obtained from the free energy functions of section 3.3.

Figure 6.8 and 6.9 show the numerical viscosity of the simulated LJ fluids, as functions

of temperature and packing fraction respectively. The structure of the figures is the same as earlier, with the left column normalized by the hard-sphere Enskog viscosity expression.

Lastly, we present another way to visualize the viscosity estimates. Figure 6.10 shows grids of all simulation runs, similar to the grid from figure 5.1. Here, every cell of the grid is coloured according to the discrepancy between the Enskog viscosity and simulation, defined as

$$\Delta(\eta, \eta_{\text{Enskog}}) = \frac{|\eta - \eta_{\text{Enskog}}|}{\eta}. \tag{6.1}$$

Larger discrepancies are marked with green/yellow, and smaller discrepancies are blue. This means that, if the Enskog viscosity η_{Enskog} at some (ξ, T^*) with some RDF differs largely from the numerical viscosity, then the corresponding area in figure 6.10 will be brighter and greener. If the theory agrees with simulation, the corresponding areas will be bluer and darker. Only four versions of the Enskog equation are included in figure 6.10, namely those following from the Thol F, the Mecke F, the Morsali RDF and the hard-sphere (Carnahan-Starling) F. The remaining three equations are omitted for brevity, but they can be found in Appendix A, figure A.5.

6.4.1. The collision integral

Consider again figure 6.8 and 6.9. While the numerical viscosity differs in value, it shows similar *trends* as the different Enskog viscosity expressions. Particularly, the viscosity expressions based on the Thol and Mecke equations look similar in shape.

We now reintroduce the collision integral Ω, which we set to unity in section 3.1.3. Recall that for hard spheres, $\Omega \equiv 1$. For *soft* particles however, it is unequal to one. In this section, we will attempt to find a value (presumably different than unity) for the collision integral of the simulated LJ fluid. We will use this value to fit Enskog's viscosity expression for the LJ fluid, to see if we can improve the viscosity predictions from figure 6.8–6.10.

We now let the collision integral Ω be an undetermined parameter, and curve-fit the Enskog expressions to the simulation results, using a standard non-linear least squares method[1]. This gives some empirical/numerical value for Ω, which can be used to adjust the viscosity equations. From figure 6.8, we can expect that $\Omega \approx 1.2$, but also that the value should increase slightly with temperature. We therefore compute one value for Ω for each T^*. We also fit the viscosity *only* at low densities, $\xi \leq 0.2$, since Enskog's expression for the viscosity is expected to break down at high densities.

Firstly, we perform a curve-fitting only of Enskog with an RDF from the Thol F. This gives us one set of numerical Ω values, shown in figure 6.11. It is immediately clear that the newly adjusted equations (curves) fit the simulation data (points) better, even though all curves are adjusted with the same collision integral. Note also that the shapes of $\eta(\xi)$ is unchanged, we have only affected the values. The Ω values used in this figure, are shown in figure 6.11. We then divide the initial viscosity expressions by this

[1] `https://docs.scipy.org/doc/scipy/reference/generated/scipy.optimize.curve_fit.html`

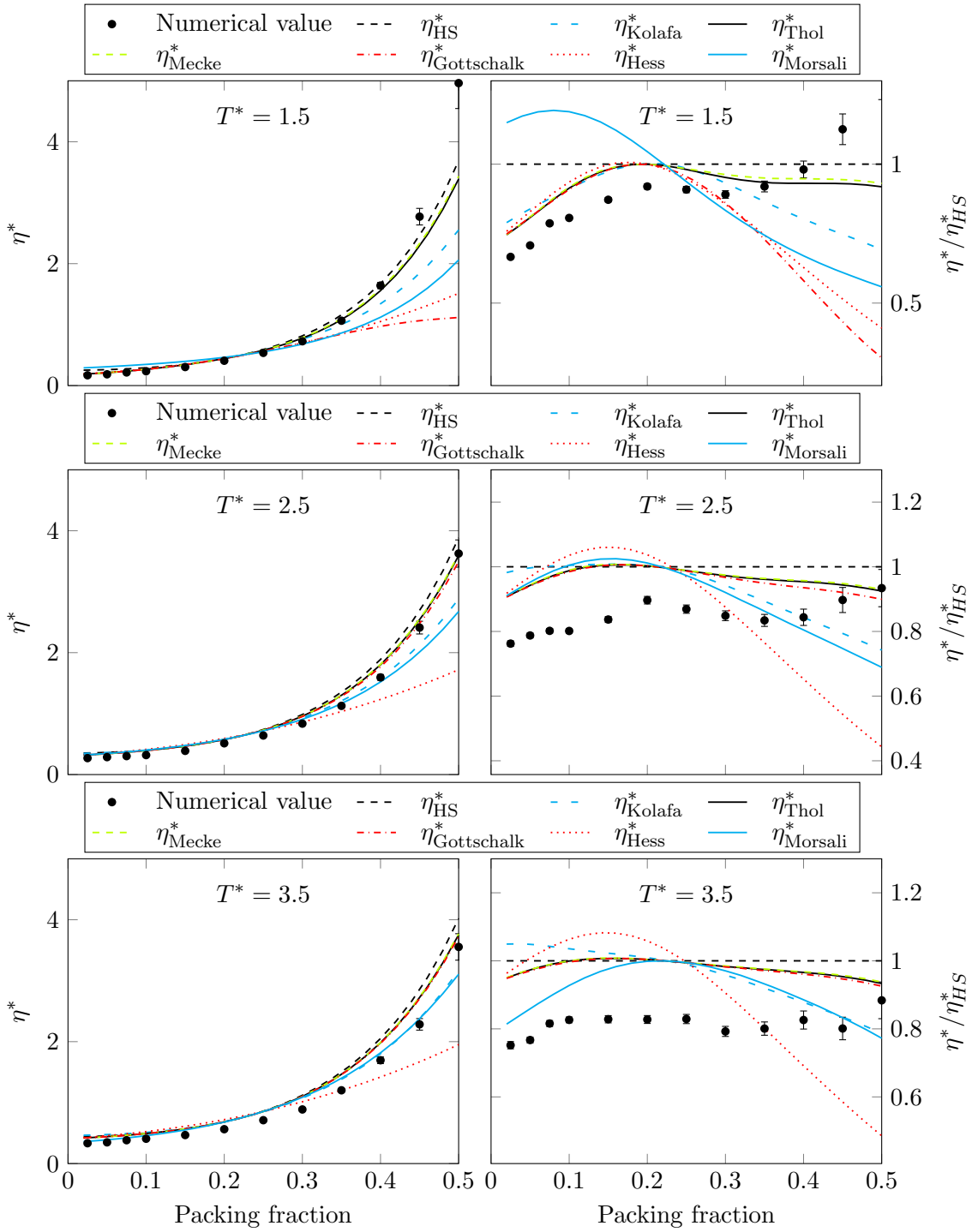

Figure 6.8.: Viscosity of the simulated systems (dots), as well as the Enskog expression for the viscosity (curves), plotted as a function of packing fraction. The Enskog expressions use RDFs from the free energies of section 3.3, and the Morsali RDF, as noted in the legend. The left column shows the viscosity value, and the right column shows the same values normalized by the hard-sphere viscosity – Enskog's viscosity expression with the CS RDF. Reduced units are used.

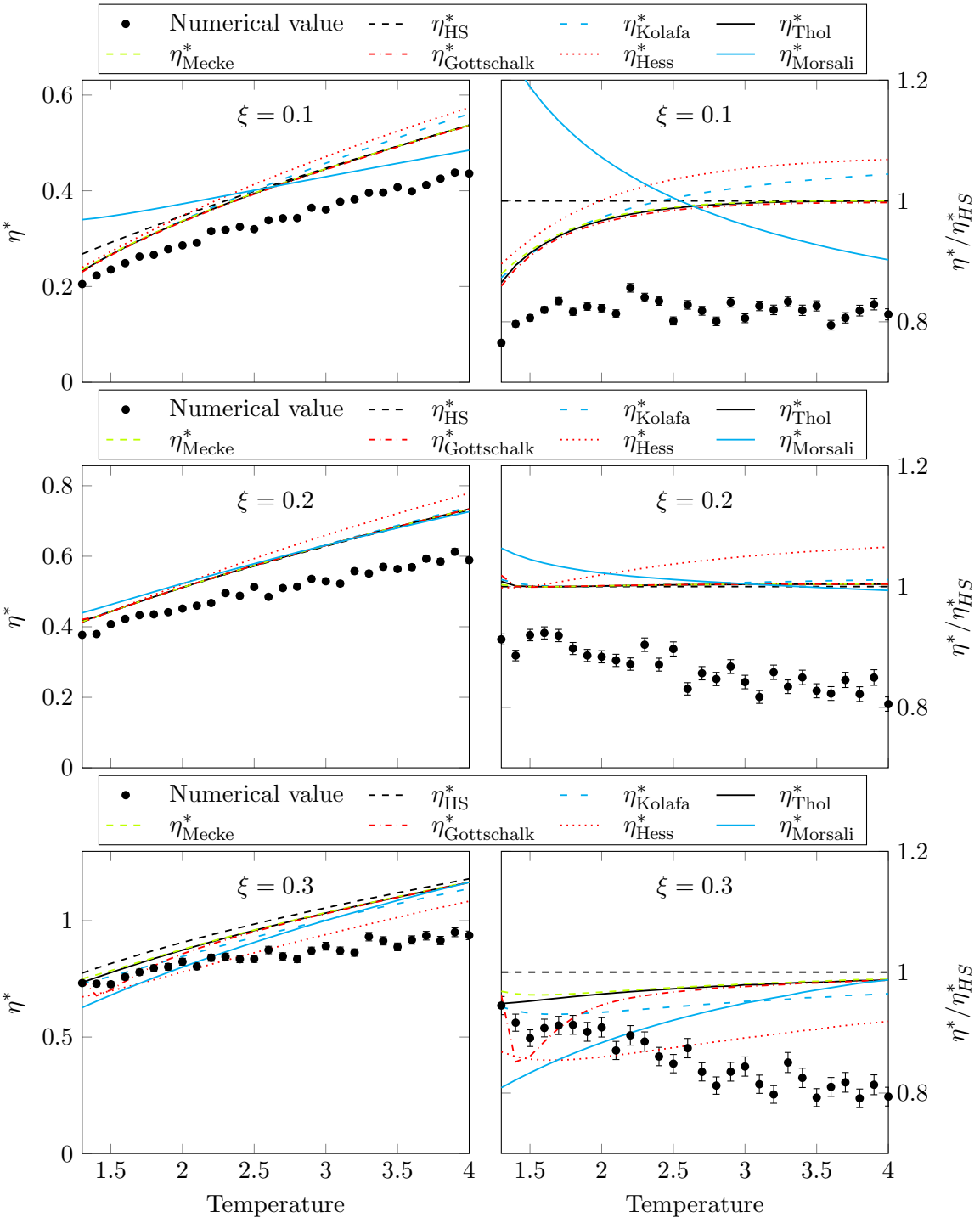

Figure 6.9.: Viscosity of the simulated systems (dots), as well as the Enskog expression for the viscosity (curves), plotted as a function of reduced temperature. The Enskog expression uses RDFs from the free energies of section 3.3, and the Morsali RDF, as noted in the legend. The left column shows the viscosity value, and the right column shows the same values normalized by the hard-sphere viscosity – Enskog's expression with the CS RDF. Reduced units are used.

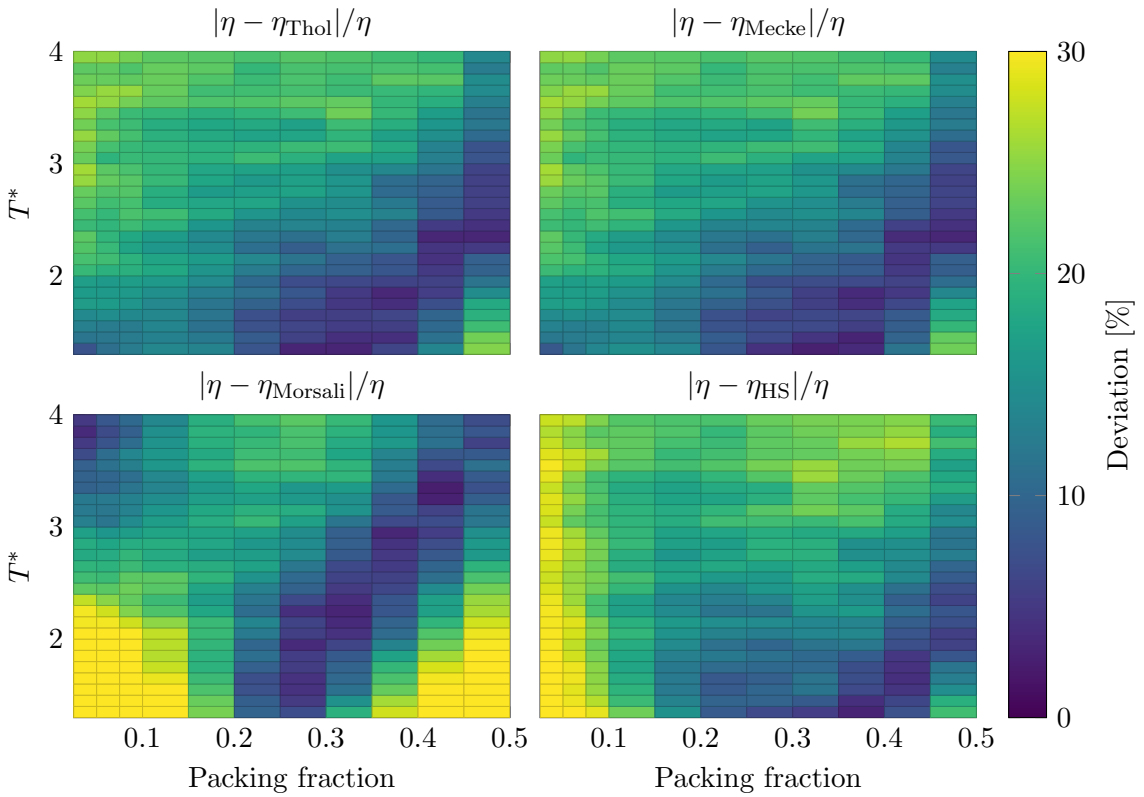

Figure 6.10.: The difference between the numerical viscosity and the predicted Enskog viscosity, shown as a colour map. The figures illustrate the difference for *all* simulations that were run. The x-axis shows packing fraction, and the y-axis shows (reduced) temperature. The colours illustrate the difference between numerical viscosity and predicted viscosity for four RDFs, (Thol F, Mecke F, Morsali RDF and CS F). A brighter (green) colour suggests a larger deviation from theory, and a darker (blue) colour implies a smaller deviance.

new curve-fitted collision integral. This results in new viscosity plots, shown in figure 6.12. As a remark, we mention that curve-fitting to obtain an estimate of σ_{eff} was also attempted. This did not cause any noteworthy difference to just fitting Ω, and was not investigated further.

Treating Ω as a numerical fitting parameter yields a semi-empirical way to obtain the viscosity of the LJ fluid. We will explore the performance of this method further in section 7.3.

6.4.2. Viscosity with numerically fitted collision integrals

To assess the results of the numerically adapted viscosity functions, a proper comparison of the viscosity predictions from the different free energies is due. This requires a comparison of the viscosity expressions, curve-fitted individually for every single RDF,

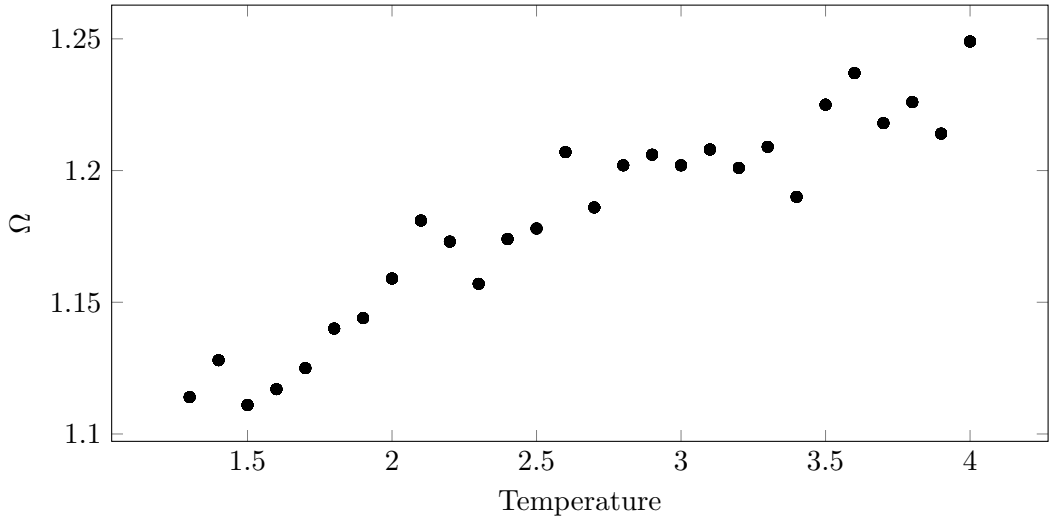

Figure 6.11.: Value of the collision integral Ω, as obtained by curve-fitting Enskog's expression for the viscosity for $\eta(\xi)$ to the numerical viscosity, for each temperature. The are fitted to the numerical viscosity Hence, we have one value for every temperature.

and not just the one from the Thol F. However, such plots turned out relatively difficult to read, and do not contribute much to this discussion. Therefore, we refer to figure A.4 in appendix A for a version of figure 6.12 where all curves have their own fitted Ω parameter.

Here, we instead visualize the performance of the adjusted viscosity functions as a colour plot, in the same way as in figure 6.10. Figure 6.13 shows such a colour plot, now with collision integrals individually obtained for each RDF function. Comparing to figure 6.10, we see that the discrepancies are now much smaller. For η_{Thol} and η_{Mecke}, the discrepancies are steadily around 5 % or less for almost all configurations, except in the high-density low-temperature region. Enskog's expression for hard-sphere viscosity (still using the CS RDF), is also fitted. A version of this figure with the remaining free energies is included in appendix A, figure A.6.

Building on the results of this chapter, we proceed to discuss the results and the behaviour of our equations and simulations in chapter 7.

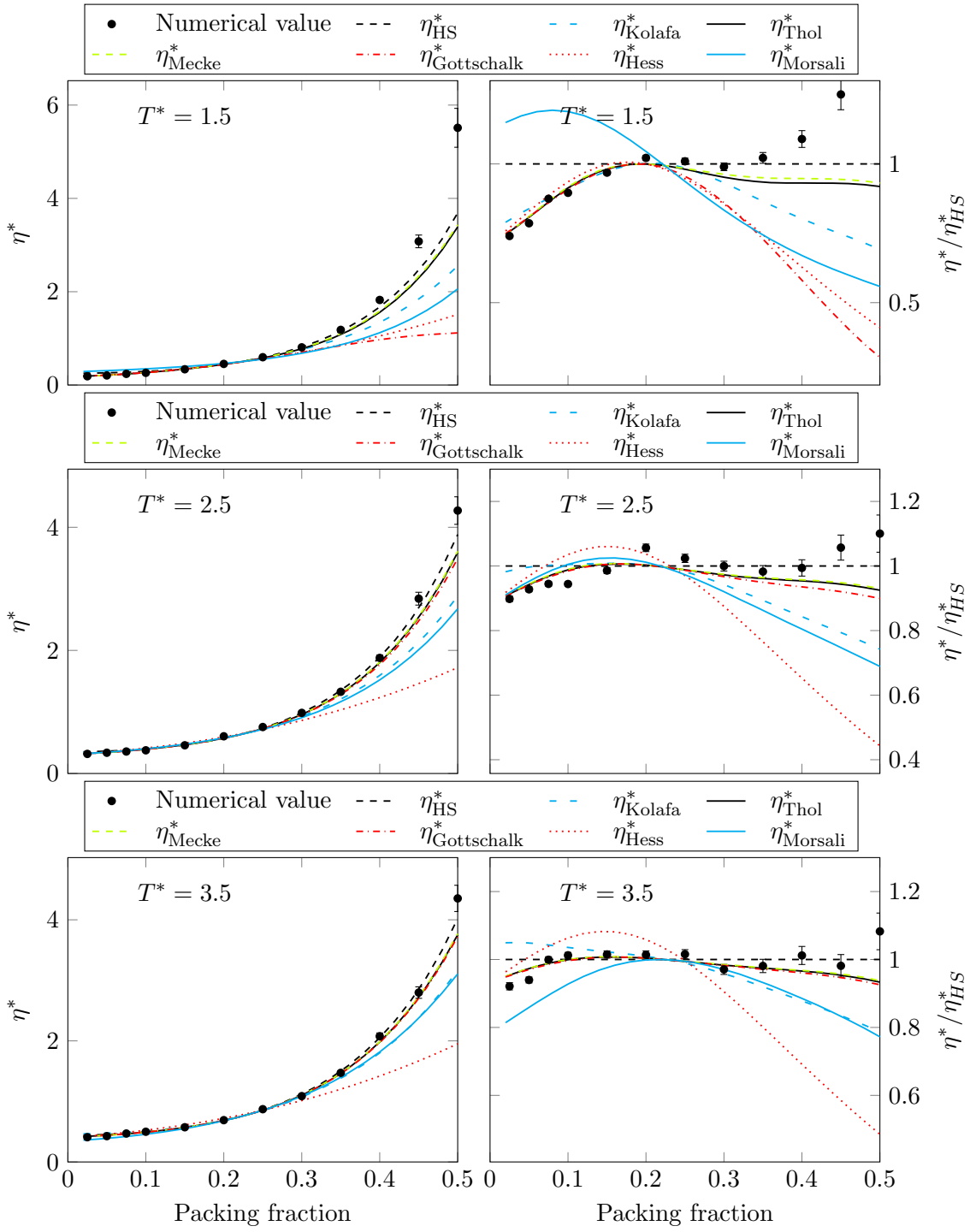

Figure 6.12.: Viscosity of the simulated systems (dots), compared to the Enskog expression for the viscosity (curves) with RDFs from the free energies of section 3.3 – plus the Morsali RDF. Here, all the equations (the curves) are divided by a collision integral $\Omega \neq 1$. The values of Ω are obtained from curve-fitting η^*_{Thol} to the numerical viscosity data. The curve-fitting is done individually for each temperature, explained in the text. The values are shown in figure 6.11.

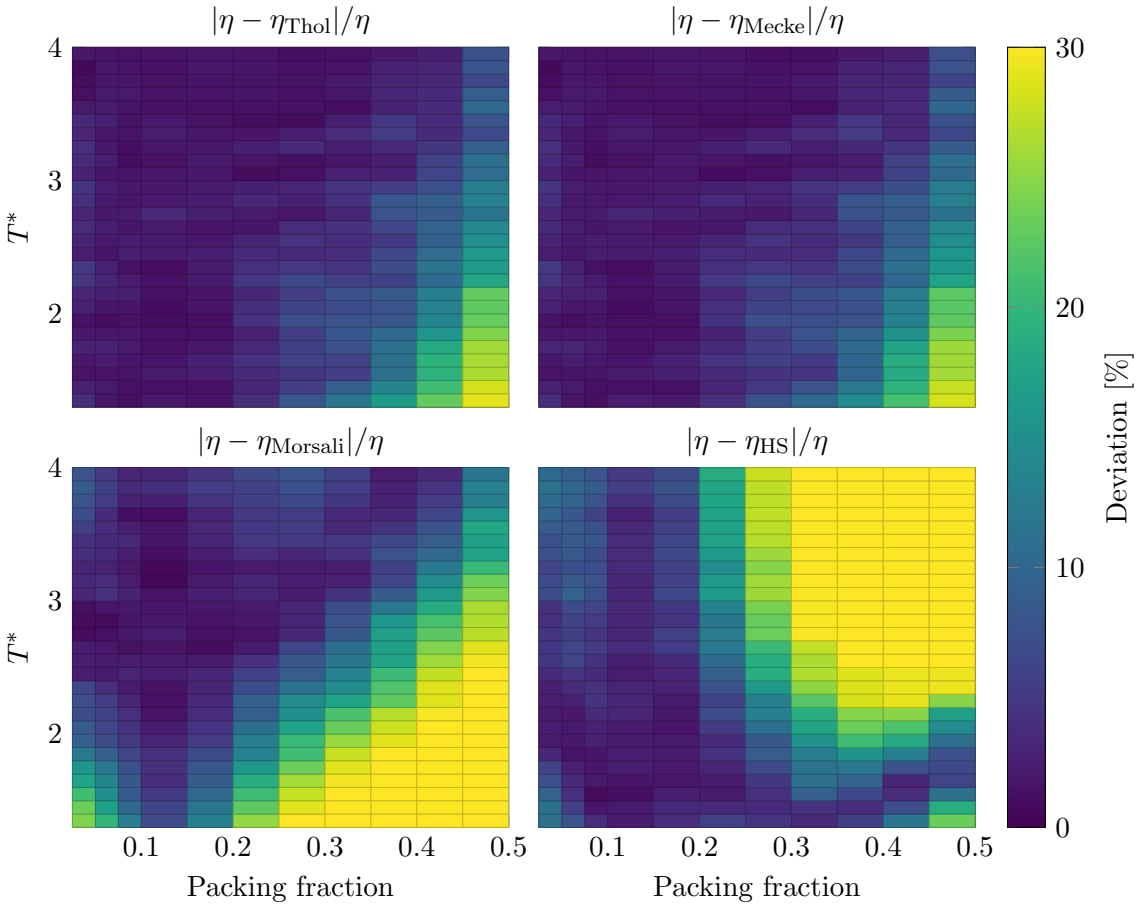

Figure 6.13.: The difference between the numerical viscosity and the Enskog viscosity *with* curve-fitted values for Ω The difference is shown as a colour map, in the same way as in figure 6.10. The collision integral has been fitted individually for all four RDFs, making them comparable. The figures illustrate the difference for all simulations. The x-axis shows packing fraction, and the y-axis shows (reduced) temperature. The colours illustrate the difference between numerical viscosity and predicted viscosity for four RDFs, (Thol F, Mecke F, Morsali RDF and CS F). A brighter (green/yellow) colour suggests a larger deviation from theory, and a darker (blue) colour implies a smaller deviance. Note that the colour bar is *capped* at 30 %, to maintain some resolution in the top two figures. In other words, the HS RDF shows larger deviations than 30 %.

7. Discussion

In this chapter, we discuss the results of chapter 6. In particular, we evaluate the performance of the viscosity model employed in this work. We discuss the definition of the RDF and its role in the Enskog equation, and we discuss the numerical fitting of the collision integral. These concepts were introduced in chapter 6. We use this to explain the viscosity results. Lastly, we mention some possible directions of related research in the future.

7.1. Assessing the validity of the simulations

As mentioned, we need to test the simulations to ensure that they behave as expected. This involves checking the reduced pressure, the RDF, and the velocity profiles of the simulations.

The simulations closely reproduce the EOS (compressibility factor) of Thol for nearly all (ξ, T^*)-configurations. Figure 6.1 and 6.2 demonstrate this. It is worth noting the differences between the different Z curves. For EOSs that are created with different methods (and with many years separating them), difference is expected. Precisely, we expect recent EOSs to outperform old ones, even though all simulations are within the validity range of the EOSs (table 3.1). It is also reasonable to expect that the numerical EOSs are more accurate than the theoretical Hess EOS. The most recent EOSs are Thol and Gottschalk. Not surprisingly, they perform better than Kolafa, Mecke and Hess for most configurations.

For the purposes of this work, it strengthens the reliability of Thol's EOS that the internal energy U it predicts also matches the simulations. In addition, the shape of the simulation RDFs (figure A.1) is in line with the Morsali RDF. When it comes to the RDF at contact, there are more subtleties involved. This is discussed in detail in section 7.2.

We also note that the velocity profiles, shown in figure 6.7 are linear. For high densities ($\xi \approx 0.5$) and low temperatures ($T^* \leq 1.5$), the velocity profiles start to show signs of slight non-linearity, as well as more noise. However, we do not expect Enskog theory to perform well in these regions, so, while noteworthy, this is not considered a major issue. Nevertheless, some caution regarding the high-ξ–low-T^*-simulations is well placed.

7.2. The RDF at contact

In section 6.2, figure we presented four definitions of the RDF at contact, and compared them to the RDFs from chapter 3. Obviously, the $g(F)$ definition in figure 6.6 fits

the Thol prediction best, since both $g(F)$ and the Helmholtz derived RDFs use this very definition. What is more interesting, is that $g(F)$ does not resemble any of the other definitions particularly well. At the same time, using $g(F)$ seems to reproduce the viscous behaviour of the LJ fluid, at least with a numerically fitted Ω.

Studying figure 6.6, we see that $g(\sigma_{\text{eff}})$ is the smallest, and $\max[g(r)]$ the largest. No reasonable estimate of the RDF at contact should be larger than the peak value of the RDF, and we do not expect particles to be located at distances shorter than σ_{eff}, except for in rare cases. We can therefore interpret $\max[g(r)]$ and $g(\sigma_{\text{eff}})$ as an upper and a lower bound for the "true" RDF at contact. The Helmholtz-derived RDF at contact, $g(F)$ falls between these two definitions for all low to intermediate densities, which is where we expect Enskog theory to work. When discussing the lower bound for the RDF at contact, it is relevant to mention that the lower bound for σ_{eff} itself was used as well (see section 3.2.4). We repeat that no significant difference between the two σ_{eff} definitions was observed in the numerical RDFs.

In figure 6.6, we see that $g(F)$ has a different high-density limit than the other definitions. At the same time, note that the viscosity at high densities is proportional to $g(\sigma)$ (see equation (3.3)). This implies that, because $g(F)$ is larger than the other definitions, it will perform better at predicting the high-density viscosity than the other definitions. Note that this does not necessarily represent any physical behaviour. Enskog's equation for the viscosity is expected to break down at higher densities, regardless of which RDF we use.

Without numerical fitting, the Morsali RDF performs poorly at predicting the viscosity, in large parts of the explored temperature and density ranges. This is illustrated in figure 6.8–6.10. Interestingly, this RDF also performs significantly worse than most F-based RDFs, even with curve-fitted values for Ω. This last point is seen in figure 6.13 and in figure A.6 in appendix A. With an RDF that was numerically fitted specifically to the LJ fluid, this may be surprising. However, we can explain this behaviour from the discussion of what "contact" means. The Morsali RDF does predict the RDF of r for the LJ system (figure 6.4), but without a proper definition of the particle radius, we are not able to use the function well. Attempts were made at evaluating the Morsali RDF at $r^* = \sigma_{\text{eff}}$ without any more success. This illustrates why deriving $g(\sigma)$ from a Helmholtz free energy is useful – it spares us the ambiguity of selecting an actual value for σ.

Since we can clearly see that $g(F)$ in the Enskog equation succeeds at predicting the viscosity, we should try to explain why. In section 3.4 we interpreted $g(\sigma)$ as a description of the collision rate. This is reasonable, since the RDF at contact does describe how many particles are in contact with each other. To describe a viscosity however, what we need is not only to know the collision rate, but also the amount of momentum transferred. These quantities are of course tightly linked. Yet, given the success of our F-derived RDF at contact, we can claim that $g(F)$ possibly explains the momentum transfer better than the geometrically motivated RDF definitions.

7.3. Viscosity

The first viscosity predictions (figure 6.8–6.10) differed from simulations by up to 25 % (and even more for some of the EOSs). Still, by introducing the curve-fitted collision integral, the results reproduce the numerical viscosity with more accuracy (less than 5 % difference for most configurations). This is shown in figure 6.12 and 6.13. This means that we can predict the viscous behaviour of the LJ fluid with accuracy, by only using its equilibrium properties. The method is precise with only one theoretically motivated fitting parameter.

In the high-density region, the viscosity predictions are less precise, even with fitted values for Ω. As explained in section 3.1.1, this is to be expected. Notice also that the difference is larger at low temperatures. At high temperatures, particles move more vigorously, making them a bit more faithful to the assumptions of Enskog theory even at slightly higher densities. In other words, high density breaks our model a bit later at high temperatures than at low temperatures.

One relevant comparison to this work is the Enskog 2σ-model of Umla and Vesovic [13, 16]. This model also showed an error in the range of 0–5 %, which is similar to this model (but overall slightly smaller). The main difference between the 2σ-model and our Helmholtz-based model, is that only one parameter – the collision integral – is needed in our model, as opposed the 2σ-model's two effective diameters. As mentioned, an attempt was also made to introduce a second fitted parameter (σ), but this did not cause noteworthy improvements to the results. We therefore do not discuss this second parameter any further, and consider only the one-parameter model.

This work demonstrates that equilibrium properties of our specific fluid system are sufficient to obtain an an RDF for use with the Enskog expression for viscosity. In other words, the only fluid-specific parameters we use stem from the equilibrium properties of the system. This is an interesting result, because it means that equilibrium properties contain information about non-equilibrium properties – or at least, that equilibrium properties are able to give approximate predictions of non-equilibrium properties. The viscous behaviour of fluids in this model comes from theoretical work that is well studied. Our contribution is that the theory can be applied to the LJ fluid, as long as we have a good description of its Helmholtz free energy. While the free energy expressions used here are mainly numerical, if an accurate theoretical expression were known, we would expect it to give similar results. Furthermore, there is no reason to expect that this procedure should fail to describe other model fluids that are similar to the Lennard-Jones fluid. That would mean we are closer to a description of more realistic fluids, although real-world fluids are often vastly more complex than the LJ fluid. Given a solid theoretical description of other transport coefficients, it is even possible that similar approaches can hold for other non-equilibrium properties than the shear viscosity. This certainly requires further research, but if we are able to approach a number of transport coefficients from the equilibrium properties of fluids, it would be a significant step forward in the field of non-equilibrium statistical physics.

7.3.1. The collision integral

With the numerical Ω estimate, it is relevant to ask what the collision integral for LJ particles actually is. Tables [58] give that $\Omega \approx 1.198$ for $T^* = 1.5$, which does not match our estimate. Furthermore, Ω should *decrease* with T^* [59], and not increase, as the estimate in figure 6.11 does. This is because the collision integral is related to the scattering cross-section of the particles, and the scattering area decreases with σ_{off} and hence temperature. We offer no explanation for the unexpected behaviour of the collision integral correlation here, and have to report it as a phenomenon. The impact of the collision integral on the viscosity of soft-potential fluids therefore needs some more investigation. Nevertheless, using it as a fitting parameter yields a successful semi-empirical viscosity model, which is able to compete with existing ones.

We also point out that the fitting has been performed for each temperature, leaving density-dependent viscosity expressions. A corresponding curve-fitting could be performed in each separate density – or in both variables at once. This is a straightforward question of implementation, and has not been done here due to time limitations.

For almost half of the simulated (ξ, T^*)-space, the HS viscosity performs worse with a curve-fitted collision integral than it did originally (figure 6.10 and 6.13). The other functions perform significantly better in most parts of configuration space. This is because the HS model shows a slightly different low-density behaviour than the other functions, and curve-fitting to the low-density values enlarges the error at higher densities. Since the collision integrals are intentionally fitted only at low densities, this should be regarded as somewhat deliberate. The theoretical motivation for curve-fitting in Ω was that the collision integral is not unity for soft spheres. In this spirit, the curve-fitting procedure is not intended for the HS model. Also note that without any curve-fitting, the HS model outperforms many of the tested LJ-models. However, when comparing the HS model with for example the Thol model, the LJ-EOSs perform considerably better than the HS versions both with and without numerical fitting.

7.3.2. Answering the research question

In section 1.3, we defined the research question

> "Can we predict the viscosity of the Lennard-Jones fluid by combining Enskog theory for hard spheres with equilibrium expressions for the radial distribution function, derived from the Helmholtz free energy?"

Even with a numerical fitting parameter, our model is able to quantitatively predict the viscosity of the Lennard-Jones fluid over the low to intermediate density range. At higher densities, it is less precise, particularly at low temperatures – which, as we have already explained (section 3.1.1), is expected for Enskog theory. We therefore indeed have an approach to the shear viscosity of the LJ fluid, based on the Helmholtz free energy and Enskog theory. This is what we set out to find. Under our procedure, however, the expression is dependent on fitting to the low-density viscosity of the fluid. This makes the method semi-empirical. Currently, the best available Helmholtz free

energy expressions for the LJ fluid are semi-empirical or empirical as well. Yet, we stress once more that the behaviour of the viscosity is reproduced by our expressions even in the regions where no fitting was performed. This is why we can claim that the procedure is successful.

7.4. Future work

This thesis leaves some questions unanswered, and several research topics are natural to investigate following this.

As mentioned, the motivation for exploring this procedure was that Pousaneh and de Wijn [17] used it to describe the shear viscosity of dipolar hard spheres. Dipolar particles interact via the Coulomb potential, which is significantly stronger at long ranges than the LJ potential. Seeing as Enskog's viscosity expression combined with free energy-derived equilibrium properties is able to predict the viscosity of fluids, it is natural to study more interaction potentials using the same methods. In principle, we can expect this method to work with a very large collection of interaction potentials. Being able to describe both soft (Lennard-Jones-like) potentials and long-ranged (Coulomb-like) potentials on their own – can they be combined? Extending this procedure to more complex fluids would be a large step forward in the field of complex fluid viscosity.

We have seen that the RDF at contact is not defined without issue. The RDF at contact which best predicts the viscosity behaviour disagrees with three different definitions that are all physically motivated and based on the shape of $g(r)$. This suggests that the RDF at contact is not perfectly understood, and that examining its definition is necessary to obtain good estimates of transport coefficients. Nevertheless, we note that the current work does not require a function (numerical of otherwise) for $g(r)$, only a value for $g(\sigma)$. As this value is derived from the Helmholtz free energy, we do not – in this context – need to know the shape of the full RDF at all.

This work intends to lay a foundation for further work on more complex interaction potentials, or more complex particle structures. Viscosity is a complex phenomenon, and much exploration is still needed in the progress towards a proper understanding of how it behaves.

8. Conclusion

This work combines Enskog's expression for the viscosity from kinetic theory with equilibrium properties of the Lennard-Jones fluid. Using these properties, which were derived from Helmholtz free energy expressions from literature, we obtain an equation for the shear viscosity of the LJ fluid. This means that we have found a non-equilibrium transport property from equilibrium descriptions of a fluid. One numerically fitted parameter had to be introduced to obtain accurate viscosity results. This parameter, the collision integral Ω, corrects for the fact that our spheres do not interact as hard spheres. The curve-fitting was only done at low densities – where the viscosity is closer to an analytically known limit – and we have demonstrated that this was sufficient in many cases to describe the viscosity, even at high densities.

Comparing to a similar model, the Enskog 2σ-model, this work has demonstrated similar error between prediction and simulation, with one less parameter. This model does however require an expression for the Helmholtz free energy of the modelled system, which is not required by the 2σ-model.

During the study, we have observed that the radial distribution function at contact, which is a key quantity in Enskog's viscosity expression, does not match the natural interpretations from the full RDF of r. Deriving the RDF at contact from Helmholtz free energy provides good viscosity predictions, but we have not clearly linked this quantity to a specific value of r. This notion implies that we may not have a full understanding of the true role the RDF at contact plays in Enskog's viscosity equation, and propose this as a future topic of research.

Even with relatively strict assumptions, Enskog's viscosity expression continues to prove itself a strong foundation for building sophisticated viscosity models. Moreover, the Helmholtz free energy is already crucial to describing systems in statistical physics. The model presented in this work can serve as a strong tool in studies of complex fluid transport theory in the future. We suggest that this method should be tested for other interaction potentials in the future, with hope that it may prove itself versatile.

Bibliography

[1] S.C. Colbeck. "A review of the friction of snow skis". In: *Journal of Sports Sciences* 12.3 (1994). PMID: 8064975, pp. 285–295. DOI: 10.1080/02640419408732174. eprint: https://doi.org/10.1080/02640419408732174.

[2] James Clerk Maxwell. "IV. On the dynamical theory of gases". In: *Philosophical Transactions of the Royal Society of London* 157 (1867), pp. 49–88. DOI: 10.1098/rstl.1867.0004. eprint: https://royalsocietypublishing.org/doi/pdf/10.1098/rstl.1867.0004. URL: https://royalsocietypublishing.org/doi/abs/10.1098/rstl.1867.0004.

[3] J. E. Jones and Sydney Chapman. "On the determination of molecular fields.—I. From the variation of the viscosity of a gas with temperature". In: *Proceedings of the Royal Society of London. Series A, Containing Papers of a Mathematical and Physical Character* 106.738 (1924), pp. 441–462. DOI: 10.1098/rspa.1924.0081. eprint: https://royalsocietypublishing.org/doi/pdf/10.1098/rspa.1924.0081.

[4] Simon Stephan, Jens Staubach, and Hans Hasse. "Review and comparison of equations of state for the Lennard-Jones fluid". In: *Fluid Phase Equilibria* 523 (2020), p. 112772. ISSN: 0378-3812. DOI: https://doi.org/10.1016/j.fluid.2020.112772.

[5] Aidan P. Thompson et al. "LAMMPS - a flexible simulation tool for particle-based materials modeling at the atomic, meso, and continuum scales". In: *Computer Physics Communications* 271 (2022), p. 108171. ISSN: 0010-4655. DOI: https://doi.org/10.1016/j.cpc.2021.108171.

[6] Florian Müller-Plathe. "Reversing the perturbation in nonequilibrium molecular dynamics: An easy way to calculate the shear viscosity of fluids". In: *Phys. Rev. E* 59 (5 May 1999), pp. 4894–4898. DOI: 10.1103/PhysRevE.59.4894.

[7] "Chapter 4 - Hydrodynamic Lubrication". In: *Engineering Tribology (Fourth Edition)*. Ed. by Gwidon W. Stachowiak and Andrew W. Batchelor. Fourth Edition. Boston: Butterworth-Heinemann, 2014, pp. 105–210. ISBN: 978-0-12-397047-3. DOI: https://doi.org/10.1016/B978-0-12-397047-3.00004-7.

[8] Jonas Bueie et al. *Shear viscosity of pseudo-hard sphere mixtures*. 2021.

[9] Leonhard Euler. "Principes généraux du mouvement des fluides". In: *Mémoires de l'académie des sciences de Berlin* 12 (1757), pp. 274–315.

[10] S. Chapman and T. G. Cowling. *The Mathematical Theory of Non-Uniform Gases*. 2nd ed. Cambridge University Press, 1953.

[11] Lawrence Korson, Walter Drost-Hansen, and Frank J Millero. "Viscosity of water at various temperatures". In: *The Journal of Physical Chemistry* 73.1 (1969), pp. 34–39.

[12] R. Di Pippo et al. "Composition dependence of the viscosity of dense gas mixtures". In: *Physica A: Statistical Mechanics and its Applications* 86.2 (1977), pp. 205–223. ISSN: 0378-4371. DOI: https://doi.org/10.1016/0378-4371(77)90029-2.

[13] Rudolf Umla. "The Enskog-2σ model, a new viscosity model for simple fluids and alkanes". PhD thesis. Imperial College London, 2013.

[14] Faezeh Pousaneh and Astrid S. de Wijn. "Shear viscosity of pseudo hard-spheres". In: *Molecular Physics* 118.4 (2020), p. 1622050. DOI: 10.1080/00268976.2019.1622050. eprint: https://doi.org/10.1080/00268976.2019.1622050.

[15] M. K. Tham and K. E. Gubbins. "Kinetic Theory of Multicomponent Dense Fluid Mixtures of Rigid Spheres". In: *The Journal of Chemical Physics* 55.1 (1971), pp. 268–279. DOI: 10.1063/1.1675518. eprint: https://doi.org/10.1063/1.1675518.

[16] Rudolf Umla, Nicolas Riesco, and Velisa Vesovic. "Viscosity of pure fluids—Enskog-2σ model". In: *Fluid Phase Equilibria* 334 (2012), pp. 89–96. ISSN: 0378-3812. DOI: https://doi.org/10.1016/j.fluid.2012.08.006.

[17] Faezeh Pousaneh and Astrid S. de Wijn. "Kinetic Theory and Shear Viscosity of Dense Dipolar Hard Sphere Liquids". In: *Phys. Rev. Lett.* 124 (21 May 2020), p. 218004. DOI: 10.1103/PhysRevLett.124.218004.

[18] Astrid S. de Wijn et al. "Viscosity of liquid mixtures: The Vesovic-Wakeham method for chain molecules". In: *The Journal of Chemical Physics* 136.7 (2012), p. 074514. DOI: 10.1063/1.3685605. eprint: https://doi.org/10.1063/1.3685605.

[19] Daan Frenkel and Berend Smit. *Understanding molecular simulation : from algorithms to applications. 2nd ed.* Vol. 50. Jan. 1996. DOI: 10.1063/1.881812.

[20] Robert Hellmann, Nicolas Riesco, and Velisa Vesovic. "Calculation of the transport properties of a dilute gas consisting of Lennard-Jones chains". In: *The Journal of Chemical Physics* 138.8 (2013), p. 084309. DOI: 10.1063/1.4793221. eprint: https://doi.org/10.1063/1.4793221.

[21] Martin P. Lautenschlaeger and Hans Hasse. "Transport properties of the Lennard-Jones truncated and shifted fluid from non-equilibrium molecular dynamics simulations". In: *Fluid Phase Equilibria* 482 (2019), pp. 38–47. ISSN: 0378-3812. DOI: https://doi.org/10.1016/j.fluid.2018.10.019.

[22] Jiří Kolafa and Ivo Nezbeda. "The Lennard-Jones fluid: an accurate analytic and theoretically-based equation of state". In: *Fluid Phase Equilibria* 100 (1994), pp. 1–34. ISSN: 0378-3812. DOI: https://doi.org/10.1016/0378-3812(94)80001-4.

[23] M. Mecke et al. “An Accurate Van der Waals-Type Equation of State for the Lennard-Jones Fluid”. In: *International Journal of Thermophysics* 17 (Jan. 1996), pp. 391–404. DOI: 10.1007/BF01443399.

[24] Monika Thol et al. “Equation of State for the Lennard-Jones Fluid”. In: *Journal of Physical and Chemical Reference Data* 45.2 (2016), p. 023101. DOI: 10.1063/1.4945000. eprint: https://doi.org/10.1063/1.4945000.

[25] Matthias Gottschalk. “An EOS for the Lennard-Jones fluid: A virial expansion approach”. In: *AIP Advances* 9.12 (2019), p. 125206. DOI: 10.1063/1.5119761. eprint: https://doi.org/10.1063/1.5119761.

[26] Siegfried Hess. “Augmented van der Waals equation of state for the Lennard-Jones fluid”. In: *Physica A: Statistical Mechanics and its Applications* 267.1 (1999), pp. 58–70. ISSN: 0378-4371. DOI: https://doi.org/10.1016/S0378-4371(98)00670-0.

[27] David M. Heyes. “Transport coefficients of Lennard-Jones fluids: A molecular-dynamics and effective-hard-sphere treatment”. In: *Phys. Rev. B* 37 (10 Apr. 1988), pp. 5677–5696. DOI: 10.1103/PhysRevB.37.5677.

[28] Karsten Meier, Arno Laesecke, and Stephan Kabelac. “Transport coefficients of the Lennard-Jones model fluid. II Self-diffusion”. In: *The Journal of Chemical Physics* 121.19 (2004), pp. 9526–9535. DOI: 10.1063/1.1786579. eprint: https://doi.org/10.1063/1.1786579.

[29] Karsten Meier, Arno Laesecke, and Stephan Kabelac. “Transport coefficients of the Lennard-Jones model fluid. I. Viscosity”. In: *The Journal of Chemical Physics* 121.8 (2004), pp. 3671–3687. DOI: 10.1063/1.1770695. eprint: https://doi.org/10.1063/1.1770695.

[30] Kippi M. Dyer, B. M. Pettitt, and George Stell. “Systematic investigation of theories of transport in the Lennard-Jones fluid”. In: *The Journal of Chemical Physics* 126.3 (2007), p. 034502. DOI: 10.1063/1.2424714.

[31] Monika Thol et al. “Equation of State for the Lennard-Jones Truncated and Shifted Model Fluid”. In: *International Journal of Thermophysics* 36 (Nov. 2015), pp. 25–43. DOI: 10.1007/s10765-014-1764-4.

[32] Gábor Rutkai et al. “How well does the Lennard-Jones potential represent the thermodynamic properties of noble gases?” In: *Molecular Physics* 115.9-12 (2017), pp. 1104–1121. DOI: 10.1080/00268976.2016.1246760. eprint: https://doi.org/10.1080/00268976.2016.1246760.

[33] N. Tchouar, M. Benyettou, and F. Ould Kadour. “Thermodynamic, Structural and Transport Properties of Lennard-Jones Liquid Systems. A Molecular Dynamics Simulations of Liquid Helium, Neon, Methane and Nitrogen”. In: *International Journal of Molecular Sciences* 4.12 (2003), pp. 595–606. ISSN: 1422-0067. DOI: 10.3390/i4120595.

[34] Hai Wang and Michael Frenklach. "Transport properties of polycyclic aromatic hydrocarbons for flame modeling". In: *Combustion and flame* 96.1-2 (1994), pp. 163–170.

[35] Mikkelsen Arne Elgsæter Arnljot. *Klassisk tranportteori*. 2000.

[36] D.S. Viswanath et al. *Viscosity of Liquids: Theory, Estimation, Experiment, and Data*. Springer Netherlands, 2007. ISBN: 9781402054822. URL: https://books.google.no/books?id=TD3TeErQD-oC.

[37] Simon Stephan et al. "Thermophysical Properties of the Lennard-Jones Fluid: Database and Data Assessment". In: *Journal of Chemical Information and Modeling* 59.10 (2019). PMID: 31609113, pp. 4248–4265. DOI: 10.1021/acs.jcim.9b00620. eprint: https://doi.org/10.1021/acs.jcim.9b00620.

[38] F. London. "The general theory of molecular forces". In: *Trans. Faraday Soc.* 33 (0 1937), 8b–26. DOI: 10.1039/TF937330008B.

[39] P. C Hemmer. *Termisk fysikk*. Norwegian. OCLC: 488673135. Trondheim: Tapir, 2002. ISBN: 9788251917391.

[40] K.A. Dill and S. Bromberg. *Molecular Driving Forces: Statistical Thermodynamics in Biology, Chemistry, Physics, and Nanoscience*. Garland Science, 2011. ISBN: 9780815344308. URL: https://books.google.no/books?id=%5C_DKAQgAACAAJ.

[41] Ángel Mulero. *Theory and Simulation of Hard-Sphere Fluids and Related Systems*. 2008.

[42] Norman F. Carnahan and Kenneth E. Starling. "Equation of State for Nonattracting Rigid Spheres". In: *The Journal of Chemical Physics* 51.2 (1969), pp. 635–636. DOI: 10.1063/1.1672048. eprint: https://doi.org/10.1063/1.1672048.

[43] John D. Weeks, David Chandler, and Hans C. Andersen. "Role of Repulsive Forces in Determining the Equilibrium Structure of Simple Liquids". In: *The Journal of Chemical Physics* 54.12 (1971), pp. 5237–5247. DOI: 10.1063/1.1674820. eprint: https://doi.org/10.1063/1.1674820. URL: https://doi.org/10.1063/1.1674820.

[44] J. Richard Elliott, Andrew J. Schultz, and David A. Kofke. "Combined temperature and density series for fluid-phase properties. II. Lennard-Jones spheres". In: *The Journal of Chemical Physics* 151.20 (2019), p. 204501. DOI: 10.1063/1.5126281. eprint: https://doi.org/10.1063/1.5126281.

[45] Ali Morsali et al. "An accurate expression for radial distribution function of the Lennard-Jones fluid". In: *Chemical Physics* 310.1 (2005), pp. 11–15. ISSN: 0301-0104. DOI: https://doi.org/10.1016/j.chemphys.2004.09.027.

[46] Pil H. Lee and Branka M. Ladanyi. "Structural and dielectric properties of dipolar hard sphere mixtures: Reference hypernetted chain and pertubation theory results". In: *The Journal of Chemical Physics* 91.11 (1989), pp. 7063–7074. DOI: 10.1063/1.457324. eprint: https://doi.org/10.1063/1.457324.

[47] Lindahl et al. *GROMACS 2021.4 Manual*. Version 2021.4. Nov. 2021. DOI: 10.5281/zenodo.5636522.

[48] Ilian T. Todorov et al. "DL_POLY_3: new dimensions in molecular dynamics simulations via massive parallelism". In: *J. Mater. Chem.* 16 (20 2006), pp. 1911–1918. DOI: 10.1039/B517931A.

[49] James C. Phillips et al. "Scalable molecular dynamics on CPU and GPU architectures with NAMD". In: *The Journal of Chemical Physics* 153.4 (2020), p. 044130. DOI: 10.1063/5.0014475. eprint: https://doi.org/10.1063/5.0014475.

[50] Steve Plimpton. "Computational limits of classical molecular dynamics simulations". In: *Computational Materials Science* 4.4 (1995). Proceedings of the Workshop on Glasses and The Glass Transition:1 Challenges in Materials Theory and Simulation, pp. 361–364. ISSN: 0927-0256. DOI: https://doi.org/10.1016/0927-0256(95)00037-1. URL: https://www.sciencedirect.com/science/article/pii/0927025695000371.

[51] Hans C. Andersen. "Molecular dynamics simulations at constant pressure and/or temperature". In: *The Journal of Chemical Physics* 72.4 (1980), pp. 2384–2393. DOI: 10.1063/1.439486. eprint: https://doi.org/10.1063/1.439486.

[52] H. J. C. Berendsen et al. "Molecular dynamics with coupling to an external bath". In: *The Journal of Chemical Physics* 81.8 (1984), pp. 3684–3690. DOI: 10.1063/1.448118.

[53] Shūichi Nosé. "A molecular dynamics method for simulations in the canonical ensemble". In: *Molecular Physics* 52.2 (1984), pp. 255–268. DOI: https://doi.org/10.1080/00268978400101201.

[54] William G. Hoover. "Canonical dynamics: Equilibrium phase-space distributions". In: *Phys. Rev. A* 31 (3 Mar. 1985), pp. 1695–1697. DOI: 10.1103/PhysRevA.31.1695.

[55] William G. Hoover. "Constant-pressure equations of motion". In: *Phys. Rev. A* 34 (3 Sept. 1986), pp. 2499–2500. DOI: 10.1103/PhysRevA.34.2499.

[56] Giovanni Bussi, Davide Donadio, and Michele Parrinello. "Canonical sampling through velocity rescaling". In: *The Journal of Chemical Physics* 126.1 (2007), p. 014101. DOI: 10.1063/1.2408420. eprint: https://doi.org/10.1063/1.2408420.

[57] Giovanni Bussi and Michele Parrinello. "Accurate sampling using Langevin dynamics". In: *Phys. Rev. E* 75 (5 May 2007), p. 056707. DOI: 10.1103/PhysRevE.75.056707.

[58] L.D. Smoot and P.J. Smith. *Coal Combustion and Gasification*. The Plenum Chemical Engineering Series. Springer US, 1979. ISBN: 9781475797213. URL: https://books.google.no/books?id=TDLvBwAAQBAJ.

[59] A. Laricchiuta et al. "Classical transport collision integrals for a Lennard-Jones like phenomenological model potential". In: *Chemical Physics Letters* 445.4 (2007), pp. 133–139. ISSN: 0009-2614. DOI: https://doi.org/10.1016/j.cplett.2007.07.097.

A. Additional figures

This appendix includes some figures that were omitted in the main text. These figures are placed here because they do not show any qualitatively unique behaviour compared to 6, but are nevertheless useful to reference as additional examples.

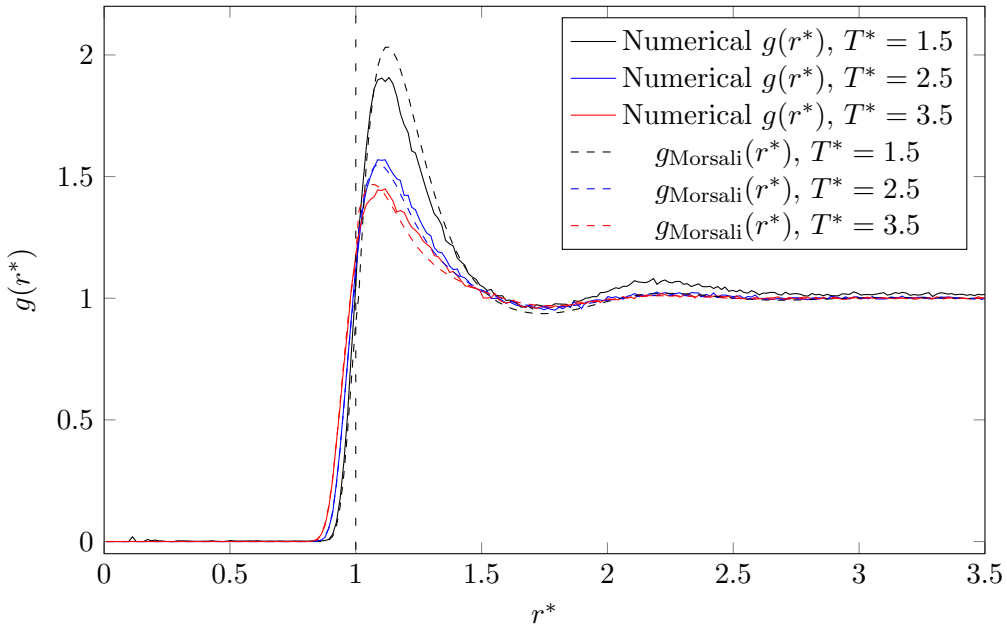

Figure A.1.: The radial distribution function of three simulated systems, for $\xi = 0.15$ at $T^* = \{1.5,\ 2.5,\ 3.5\}$. For each curve, the corresponding Morsali RDF curve is also shown as a dashed line of the same colour. The numerical RDF is computed at discrete intervals of 0.015σ. A vertical line to mark $r^* = \sigma = 1$ is included, as a reference to the steep slope of the RDFs.

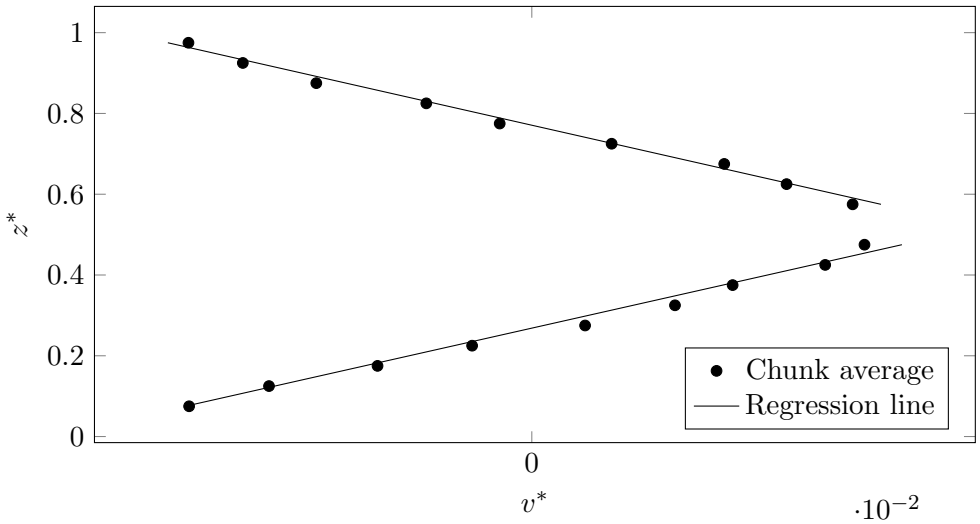

Figure A.2.: Velocity profile, extracted from one simulation with $(\rho^*, T^*) = (0.5, 1.5)$. This is a larger version of the bottom plot in figure 6.7. The lines are regression lines of the velocity gradient in the simulation cells. The points are time averaged velocity values, for each chunk. Here, we see that the linearity is starting to break down.

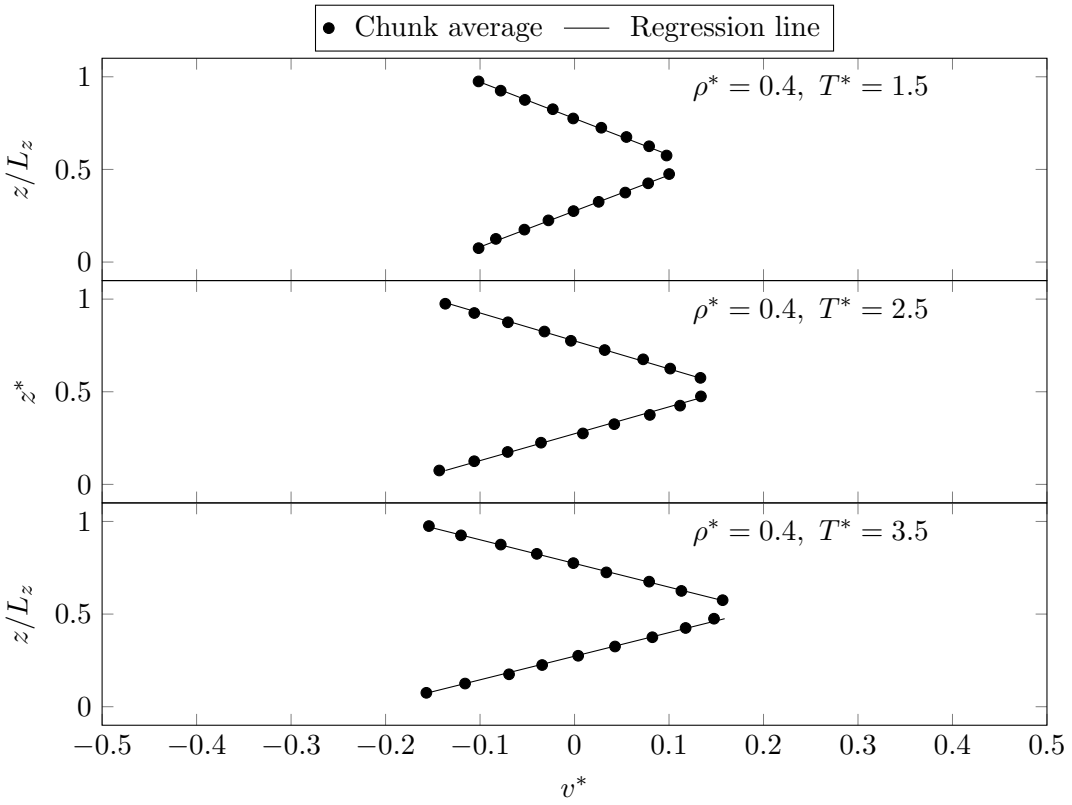

Figure A.3.: Velocity profile in the simulation cell, extracted from three simulations, where $\xi^* = 0.4$ and $T^* = \{1.5,\ 2.5,\ 2.5\}$. The dots show the time average of the velocities in every chunk. The lines come from linear regression of the velocity points. Along the y-axis is the z-coordinate, the height of the particles within the box, divided by the total box height L_z.

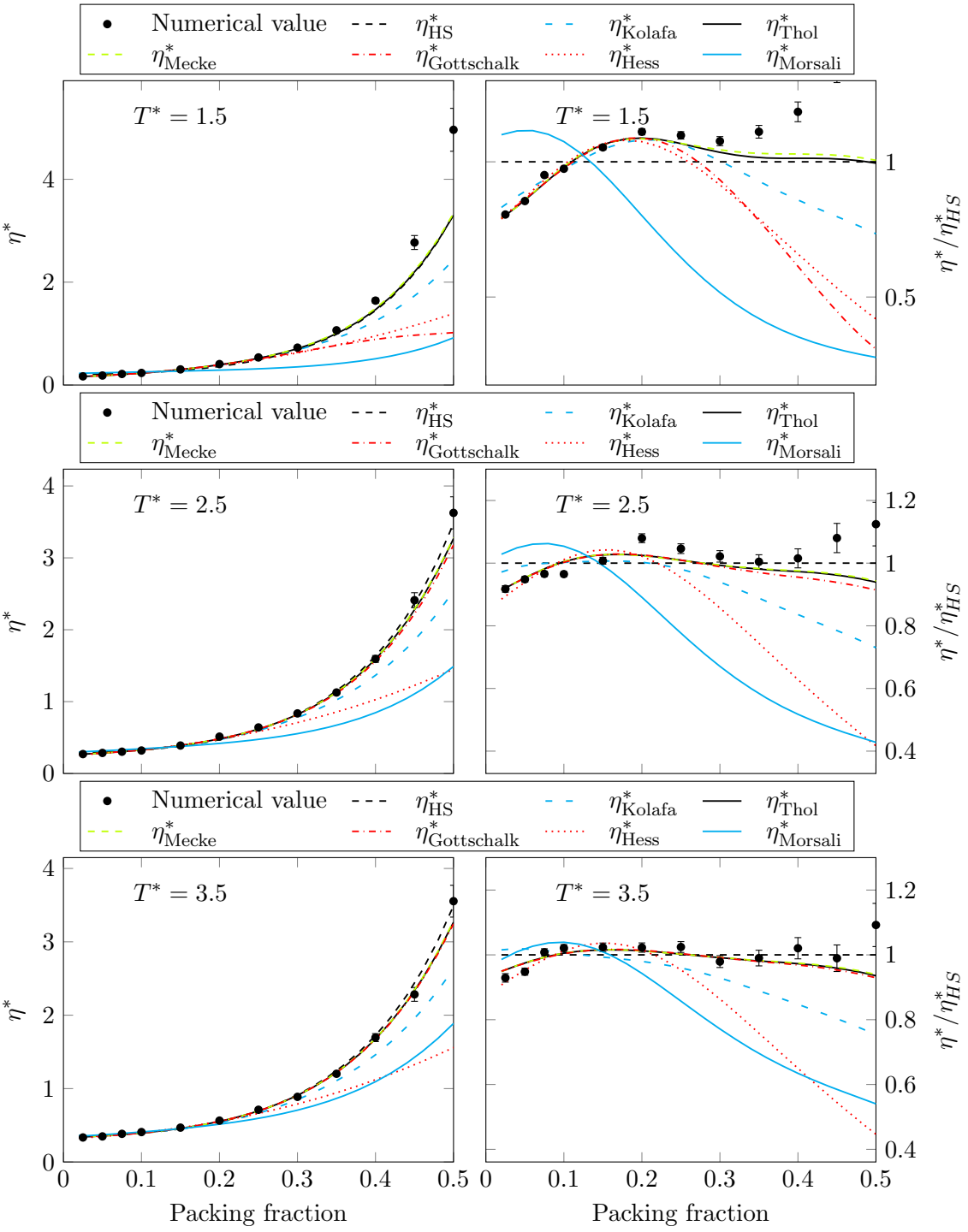

Figure A.4.: Viscosity of the simulated systems (dots), compared to Enskog's expression for the viscosity (curves) with RDFs from the free energies of section 3.3 – plus the Morsali RDF. Here, all the equations (the curves) are divided by a collision integral $\Omega \neq 1$. The values of Ω are obtained individually for each temperature, from curve-fitting, as explained in the text. The values are shown in figure 6.11.

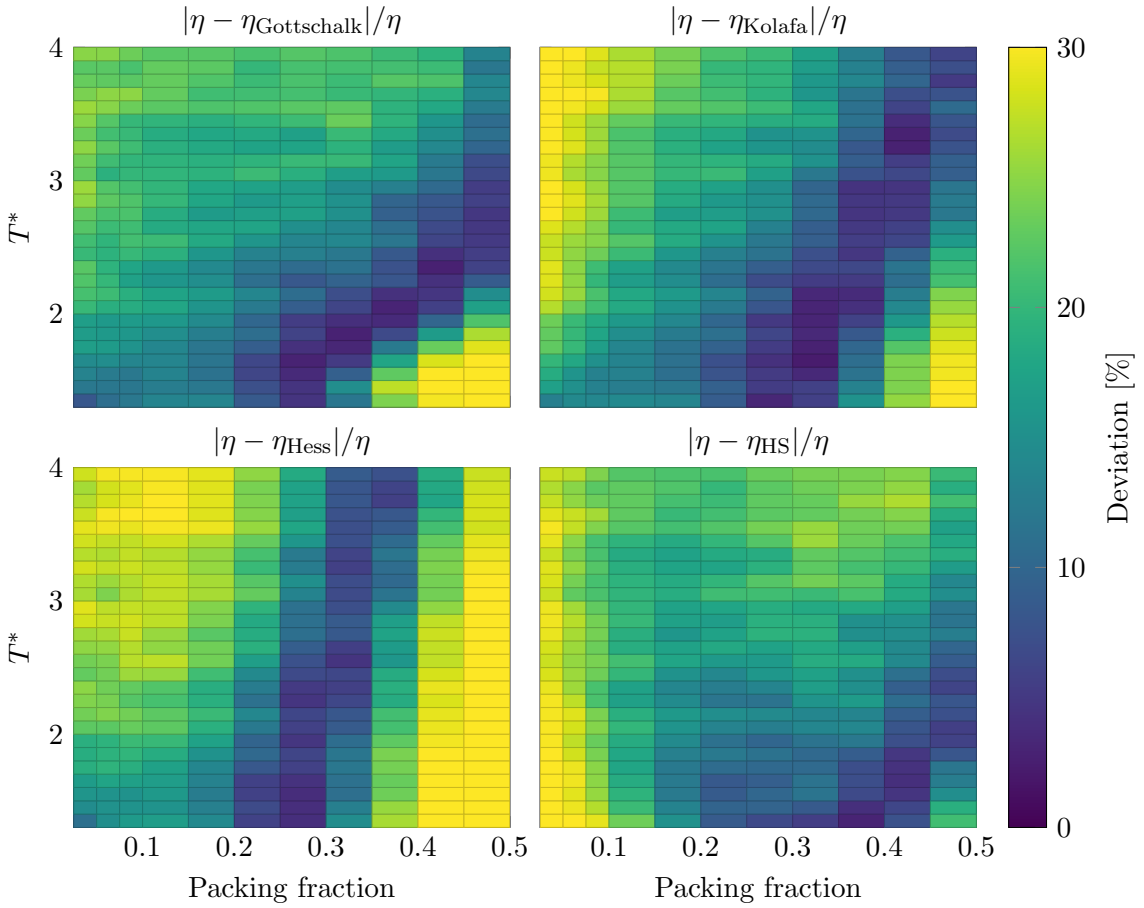

Figure A.5.: The difference between the numerical viscosity and the predicted Enskog viscosity, shown as a colour map. The figures illustrate the difference for *all* simulations that were run. The x-axis shows packing fraction, and the y-axis shows (reduced) temperature. The colors illustrate the difference between numerical viscosity and predicted viscosity for four RDFs, (Gottschalk EOS, Kolafa EOS, Hess EOS and CS RDF). A brighter (green/yellow) colour suggests a larger deviation from theory, and a darker (blue) colour implies a smaller deviance. The colour bar is capped at 40 %, meaning that the true deviation in the yellow areas can be – and is – larger than indicated. This is done to retain resolution at lower discrepancies.

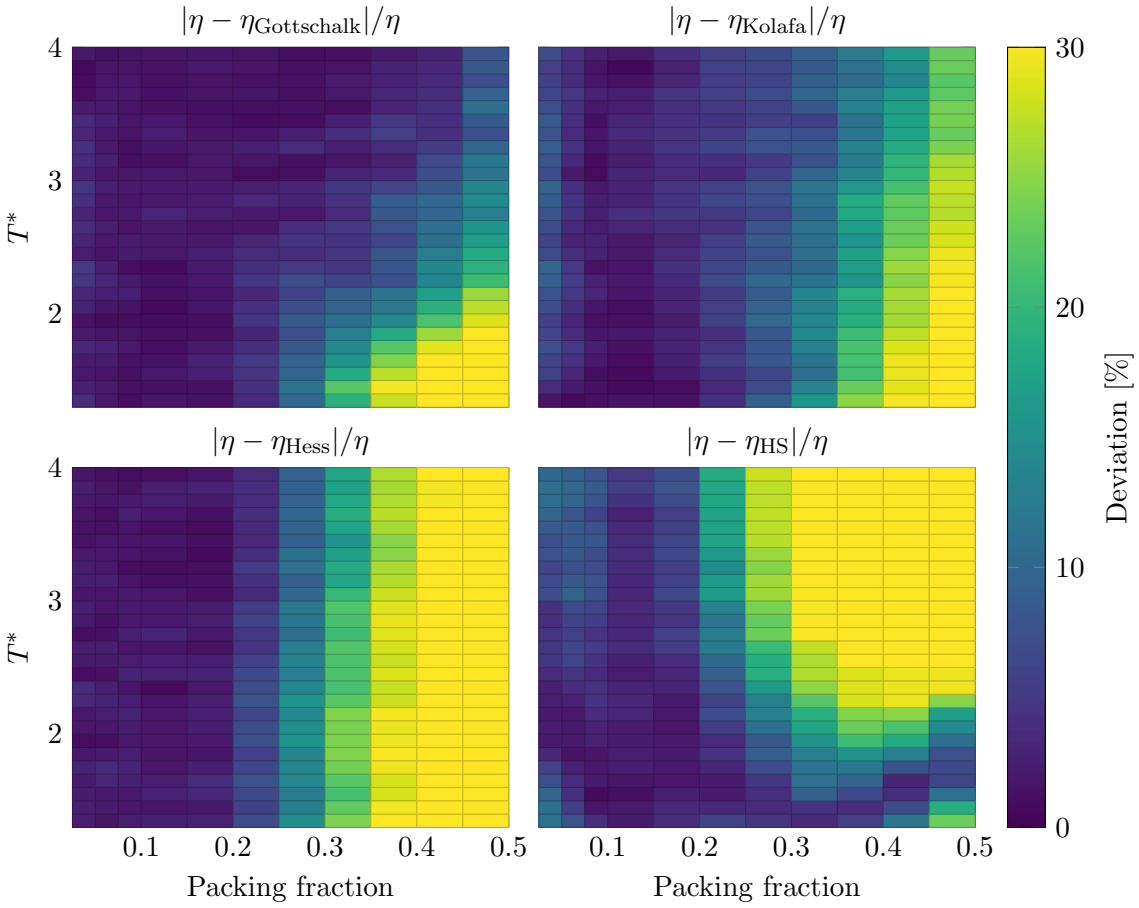

Figure A.6.: The difference between the numerical viscosity and the Enskog viscosity *with* curve-fitted values for Ω The difference is shown as a colour map, in the same way as in figure 6.10. The collision integral has been fitted individually for all four RDFs, making them comparable. The figures illustrate the difference for all simulations. The x-axis shows packing fraction, and the y-axis shows (reduced) temperature. The colours illustrate the difference between numerical viscosity and predicted viscosity for four RDFs, (Gottschalk EOS, Kolafa EOS, Hess EOS and CS RDF). A brighter (green/yellow) colour suggests a larger deviation from theory, and a darker (blue) colour implies a smaller deviance. Note that the colour bar is *capped* at 30 %, to maintain some resolution in the top two figures. In other words, the HS RDF shows larger deviations than 30 %.

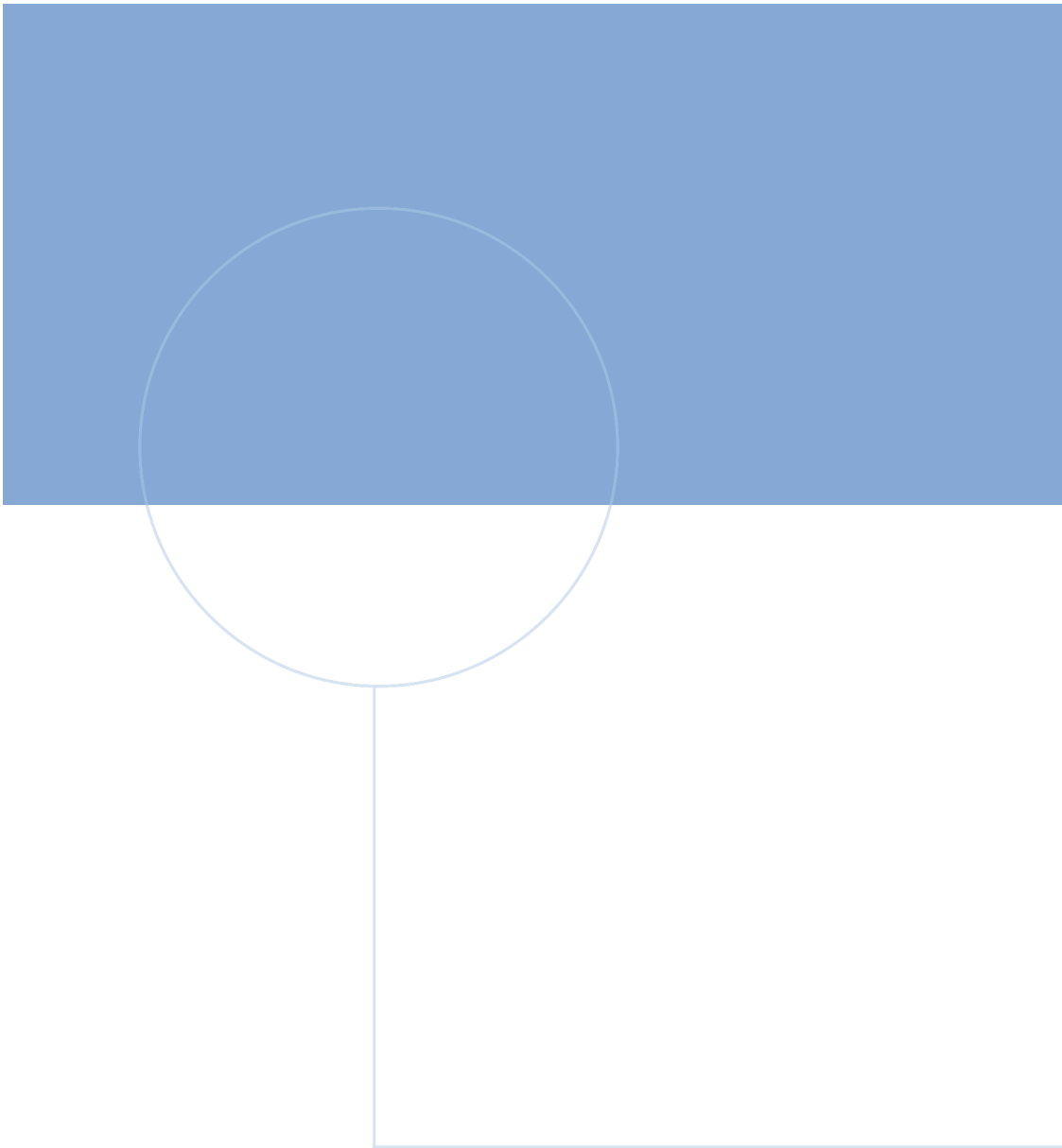

NTNU

Norwegian University of
Science and Technology